Experimental Investigation of Dynamical Properties and Ergodicity in Plasma Crystals

Diploma Thesis
by
Christina Knapek

30. Januar 2004

Technische Universität München
Fakultät für Physik

Max-Planck-Institut für Extraterrestrische Physik

Themensteller: Prof. Dr. Volker Schönfelder
Betreuer: Prof. Dr. Gregor Morfill

Erklärung

Mit der Abgabe der Diplomarbeit versichere ich, dass ich die Arbeit selbständig verfaßt und keine anderen als die angegebenen Quellen und Hilfsmittel benutzt habe.

.....	.....
(Ort, Datum)	(Unterschrift von Christina Knapek)

Acknowledgements

I want to thank just everyone who supported me to finish this thesis in time and whom I do not mention here because the time is too short.

Namely I thank Uwe Konopka for his supervision and motivation during the last weeks, Wolfram Bunk for the helpfull discussions and Rick Quinn for his advice and help at the beginning of my thesis.

Especially I thank Daniel Mohr for his help during the last night when I finished this thesis and for his help in programming during the last year.

Contents

Physical Constants **III**

1 Introduction **1**

2 Plasma Crystals **3**
2.1 Definition of Plasmas . . . 3
2.2 Strong Coupling . . . 4
2.3 Particles in Plasmas . . . 7
2.3.1 Charging . . . 7
2.3.2 Forces Acting on Particles . . . 7
2.3.3 Thermodynamical Phases . . . 8
2.3.4 Waves in Plasma Crystals . . . 10
2.3.5 Equation of Motion of a Single Particle . . . 11

3 Ergodic Theory **13**
3.1 Description of a Dynamical System . . . 13
3.1.1 Hamilton Formalism . . . 13
3.1.2 Probability Functions . . . 14
3.1.3 Macroscopic Averages . . . 14
3.2 The Ergodic Theorem . . . 15
3.3 Application of the Ergodic Theorem . . . 17
3.3.1 Phase Space of Particles in Plasma Crystals . . . 17
3.3.2 Conditions of Ergodic Behaviour . . . 18

4 Experiment and Data Preparation **21**
4.1 Basic Setup . . . 21
4.2 Particle Tracking . . . 26
4.3 Experimental Errors . . . 27
4.3.1 Gaussian Error Distribution . . . 28
4.3.2 Analysis Methods . . . 29
4.3.2.1 Histograms . . . 29
4.3.2.2 Fit Procedure . . . 30
4.3.3 Measured Error Distribution . . . 31
4.4 Estimation of Experimental Parameters . . . 33

4.4.1 Basic Quantities . . . 34
4.4.2 Dependence of Thermal Motion . . . 35
4.4.3 Dependence of the Maximum Displacement . . . 37

5 Analysis **43**
5.1 Performed Experiments . . . 44
5.1.1 Specifications . . . 44
5.1.2 Expected Scales . . . 46
5.1.2.1 Length Scales . . . 46
5.1.2.2 Time Scales . . . 49
5.1.3 Comparison of Different Magnifications . . . 50
5.1.4 Summary . . . 51
5.2 Stationarity of the Plasma Crystal . . . 52
5.2.1 Detection of Common Trends . . . 53
5.2.1.1 Running Mean and Standard Deviation . . . 53
5.2.1.2 Power Spectra . . . 59
5.2.1.3 Summary . . . 64
5.2.2 Removing of Common Trends . . . 64
5.2.2.1 Rotation . . . 65
5.2.2.2 Oscillation in the Confinement Potential . . . 69
5.2.2.3 Flows . . . 71
5.2.2.4 Radial Contractions of the Crystal . . . 71
5.2.3 Result of Detrending . . . 72
5.3 Stationarity of the Single Particle Time Series . . . 83
5.4 Dynamical Behaviour of Single Particles . . . 89
5.4.1 Maxwell Distribution of Velocities . . . 89
5.4.2 Velocity Distributions in the Plasma Crystal . . . 90
5.4.3 Distribution of the Displacement . . . 98
5.5 Test for Ergodic Behaviour . . . 106
5.5.1 Conditions for Ergodicity . . . 107
5.5.2 Hypothesis Testing . . . 107
5.5.3 Kolmogorov-Smirnov and Kuiper Tests . . . 109
5.5.3.1 Results of Statistical Tests for Particle Displacements . . . 112
5.5.3.2 Results of Statistical Tests for Velocities . . . 115
5.5.3.3 Spatial Dependence of the Test Results . . . 117
5.5.4 Conclusion of the Test . . . 118

6 Summary and Conclusion **121**

References **125**

List of Figures **129**

List of Tables **135**

Physical Constants

k_B	$1.38 \cdot 10^{-23}$ J/K	Boltzmann constant
q_e	$1.602 \cdot 10^{-19}$ C	elementary charge
ϵ_0	$8.854 \cdot 10^{-12}$ As/Vm	vacuum dielectric constant

Chapter 1

Introduction

Plasma crystals were theoretically predicted by [1] and shortly after that discovered experimentally [2]. They are formed by small spherical dust particles which get highly charged in a plasma due to collection of electrons and ions on their surfaces, and thus can form crystalline structures due to their strong mutual interactions.

A subject of interest in the study of plasma crystals is the dynamical behaviour of its constituents. By visual observation of the μm-sized particles, properties such as particle oscillation around the mean lattice site and thermal motion can be investigated directly, giving a direct determination of the phase space of the particles motions. From this, informations can be extracted on macroscopic quantities such as the particle temperature.

Ergodic behaviour in a plasma crystal is understood as the equivalence of the dynamic behaviour of a single particle in time and the ensemble of particles as components of the crystal at one particular time, as it is expressed in general in terms of ergodic theory. Ergodicity is often presupposed in the interpretation of particle dynamics of a plasma crystal. A lot of quantities such as particle temperature, the motion under the influence of the interparticle potential or the charge are derived from series of images taken of the whole crystal by averaging quantities over the ensemble of particles in each image and over time [17], although it is not deductively clear whether this approach is valid.

As will be illustrated in this thesis, ergodic behaviour of a physical system is subject to certain conditions. Measurement times long compared with the intrinsic dynamics of the system and a closed system, or at least a system in thermal equilibrium with its surroundings, are necessary. Following from the last is the exclusion of non-stationary systems for application of the ergodic theorem. Further, the ensemble is defined as numbers of independent equal realisations of one basic dynamic process. Plasma crystals are strongly coupled systems, and though each particle within the crystal is a realisation of a basic system, the strong coupling as a nature of plasma crystals contradicts with the condition of independent systems in an ensemble.

In conclusion, an a priori assumption of ergodic behaviour of particles in plasma crystals

is not a valid assumption.

The aim of this thesis is to investigate fundamental dynamical properties of particles in a monolayer of particles, i.e. a 2-dimensional plasma crystal, with respect to the question whether the equivalence of time and ensemble phase functions is given though the condition of independent systems is violated. What will not be performed is a proof of ergodicity itself.

The requirement for the experiment is to generate a stable single layer of particles arranged in a plasma crystal. External influences should be excluded as far as possible, or at least the effects should be well defined, to meet the conditions of energetic equilibrium and stationarity. Long-time measurements exceeding the usual time span chosen for observations have to be performed, on the one hand to confirm the stability of the system with respect to stationarity and on the other hand to improve the statistics by a large number of data points.

The presented work is organized as follows:

Chapter 2 describes basic properties of plasma crystals and the usual description of the particle dynamics. After that some theoretical background to the ergodic theory is given in chapter 3 and the conditions for ergodic behaviour are described in more detail, connected to the question of their fulfillment in the plasma crystal.

The experimental setup is treated in chapter 4. Here importance is put on the estimation of expected measurement errors and on expected time and length scales of the intrinsic dynamics of the particles. This gives the possibility to control the dynamical state of the particles in a plasma crystal according to external experimental parameters from the outset.

The last part of the thesis, chapter 5, concerns with the analysis of data obtained from the series of measurements described in section 5.1. Here the important features are at first the examination of stationarity in the system. Nonstationarities are detected and identified as trends in section 5.2. These will be removed from the data by decomposition of the time series of measurements into parts caused by different physical effects. Distribution functions will be obtained and investigated which express the dynamical properties of the single particles in section 5.4. Finally, a direct test on ergodic behaviour is carried out in section 5.5. This test is based on statistical methods and compares the ensemble of particles in a plasma crystal with the trajectory of one single particle in time, with respect to absolute values of variables such as spatial coordinates and velocities in the system.

Chapter 2

Plasma Crystals

A plasma crystal as generated in a laboratory consists of charged spherical, μm-sized particles, which are levitated in the plasma sheath region of a plasma that is generated by a radio-frequency (RF) discharge between two electrodes. The particles can arrange themselves in a two or three dimensional lattice structure due to their charge and their interaction with plasma components. In this chapter, after a short definition of the plasma state in section 2.1, a thermodynamical description of dust particles in plasmas in terms of a new plasma component is given in section 2.2. Section 2.3 is concerned with basic properties of dust particles injected into a plasma and their interactions with other particles or plasma components.

2.1 Definition of Plasmas

Plasmas can be found nearly everywhere, starting from stars and interstellar space to neon tubes and candles. It is often called the fourth state of matter among solid, liquid and gaseous. While a gas consists of free neutral atoms or molecules with a kinetic energy high enough to prevent any bonds, a plasma is made up of ionized atoms and free electrons. To generate it, energies of more than 1 eV ($\approx$ 11600 K) are needed. Ions and electrons have strong interaction forces due to their opposite charge, which leads to a behaviour unlike a gas. But not every ionized gas can be called plasma.

The main characteristic of a plasma is its quasineutrality. That requires on the one hand the same charge densities of ions and electrons, $q_+ n_+ = q_- n_-$ where $n_{+/-}$ are the densities of ions and electrons, respectively, and $q_{+/-}$ the corresponding charges. On the other hand, ions and electrons are free to move, if their mean kinetic energy $E_{kin} = k_B T$ is higher than their potential energy $E_{pot} = q_{+/-}\Phi$ and they will then arrange themselves due to Coulomb forces acting between them. The lighter electrons will accumulate around the ions, thus screening the positive charge as seen from the outside. The distance from the screened charge, where the Coulomb potential has dropped to $1/e$ of its size at the center

is called Debye length λ_D:

$$\lambda_D = \sqrt{\frac{\epsilon_0}{\mathrm{q}_e^2}\frac{k_B T}{n_-}} \tag{2.1}$$

The screened Coulomb potential $\Phi(\tilde{r})$ at the distance $\tilde{r}$ from a particle with any charge Q is

$$\Phi(\tilde{r}) = \frac{Q}{4\pi\epsilon_0} \cdot \frac{1}{\tilde{r}} \cdot e^{-\frac{\tilde{r}}{\lambda_D}} \tag{2.2}$$

with the vacuum dielectric constant ϵ_0, the Boltzmann constant k_B and the elementary charge q_e.
Only at length scales L larger than λ_D the plasma can be called quasineutral and plasma parameter can be defined. This leads to a restriction of the total number N_{tot} of particles in the plasma: It has to be much larger than the number of particles N_D in the Debye volume (the spherical volume with radius λ_D around the center ion). Else the system size would be just of the magnitude of the Debye length. To summarize, following conditions hold for an ideal plasma[4]:

- $n_+ = n_-$
  The electron density has to be equal to the ion density.
- $L \gg \lambda_D \Rightarrow N_{total} \gg N_D$
  The extension of the system has to be much larger than the Debye length $\lambda_D \Rightarrow$ the total amount of particles in the system has to be much larger than the number of particles in the Debye volume

A shift of electrons and ions leads to a restoring force caused by electrostatic forces. In consequence, oscillations of the plasma constituents occur at the so called plasma frequency ω_p which is proportional to $\sqrt{n_-}$. It is a characteristic quantity which sets a lower limit to the frequencies of propagating electromagnetic waves.

In the next section plasma will be classified regarding to the particle dynamics and energy.

2.2 Strong Coupling

The behaviour of the plasma constituents is determined by the ratio of their potential and kinetic energies. This ratio is characterised by the Coulomb coupling parameter Γ:

$$\Gamma = \frac{\langle E_{pot} \rangle}{\langle E_{kin} \rangle} \tag{2.3}$$

with the mean potential energy $\langle E_{pot} \rangle$ and the mean kinetic energy $\langle E_{kin} \rangle$. For a system in thermodynamic equilibrium, the mean kinetic energy per degree of freedom is $1/2 k_B T$.

The mean potential energy depends on the kind of interaction potential between plasma particles. In the case of Coulomb forces this is

$$\langle E_{pot} \rangle = \frac{Q^2}{4\pi\epsilon_0\Delta} \qquad \text{Coulomb potential} \tag{2.4}$$

$$\langle E_{pot} \rangle = \frac{Q^2}{4\pi\epsilon_0\Delta} \cdot e^{-\Delta/\lambda_D} \qquad \text{screened Coulomb potential} \tag{2.5}$$

with the mean interparticle spacing Δ. The value of Γ now gives a separation of plasmas into weakly coupled systems for $\Gamma < 1$, and strongly coupled for $\Gamma \geq 1$. Usual plasmas have $\Gamma < 1$, as can be seen in figure 2.1.
As an example: To get $\Gamma = 1$ for an Argon plasma with a mean kinetic energy of $E_{kin} = 0.026$ eV ($\hat{=}$ room temperature), and assuming a Coulomb potential with a charge $Q = +1$ q_e and three degrees of freedom, for the ions a mean interparticle distance Δ of:

$$\Delta = \frac{Q^2}{6\pi\epsilon_0 E_{kin}} \approx 4 \cdot 10^{-8} \text{ m} \tag{2.6}$$

would follow. This would mean an ion density of 10^{22} m^{-3}, whereas the usual density of an fully ionized Argon plasma is 10^{20} m^{-3} at a pressure of 2 Pa. An decrease of the ion density from 10^{22} to 10^{20} m^{-3} for $\Gamma = 1$ would demand $\langle E_{kin} \rangle = 0.007$ eV, which corresponds to a temperature of ≈ 80 K. A screened Coulomb potential would even reduce the required kinetic energy due to the lower mean potential energy. In conclusion, strong coupling seems to be not easy to achieve in a plasma consisting of electrons and ions with charges in the range of a few q_e.

Dusty or colloidal plasmas have a third component besides electrons and ions – micrometer-sized dust particles. These collect ions and electrons on their surface. The electrons have a much higher mobility than the ions, thus leading to negative net charges of -1000 and more elementary charges per μm particle diameter on the particle surface [10]. Therefore the interaction potential between the particles can become much higher than their kinetic energy. Due to the high mass of the dust particles compared with ions or electrons, they may remain relatively fixed, while ions and electrons move around and form a flexible neutralizing background for the particles. The coupling parameter for the dust particle component of the plasma can reach values of more than 1000 (see figure 2.1), and highly ordered systems, called plasma crystals, can form [1]. These kind of systems will be described in more detail in the next section.

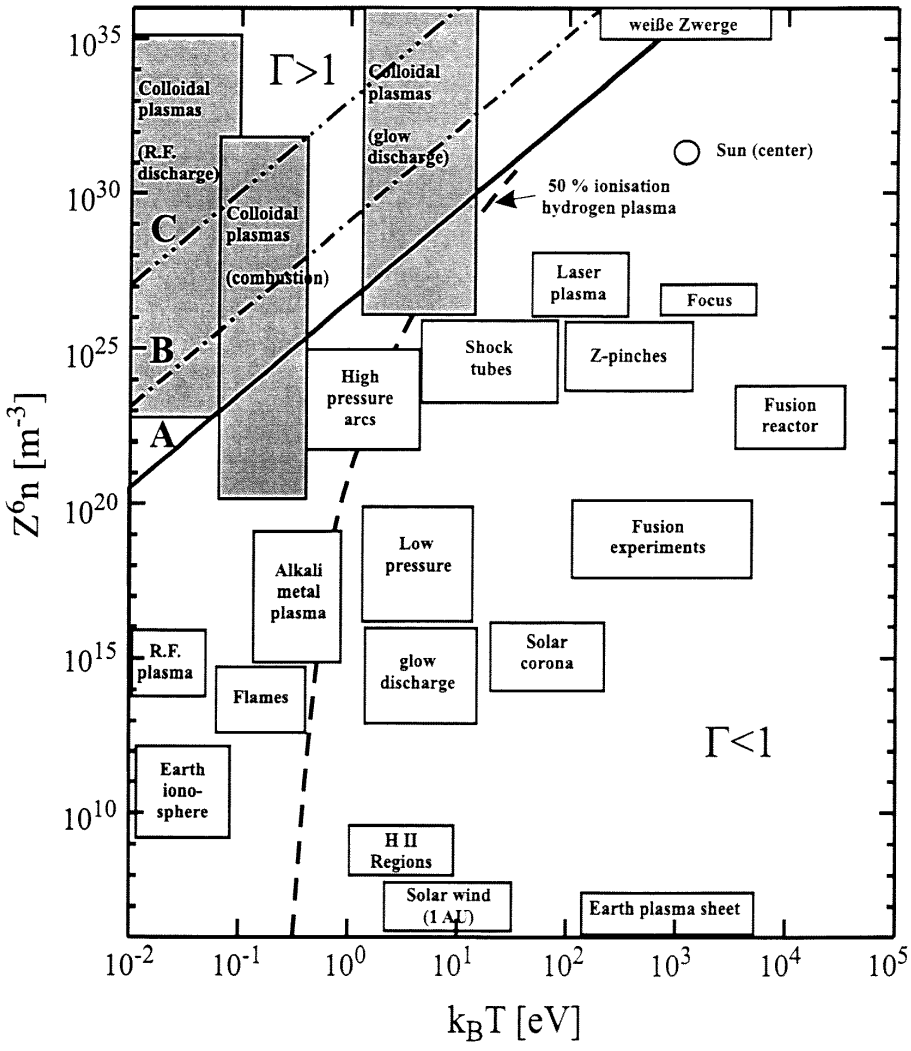

Figure 2.1: Overview of plasmas and the corresponding coupling parameter Γ. Dusty plamas are located in the upper left corner (also called colloidal plasmas) with $\Gamma > 1$.

2.3 Particles in Plasmas

Processes determining the behaviour of dust particles contain charging processes (section 2.3.1), external forces such as gravity an electrostatic forces (section 2.3.2) and the mutual interaction of particles leading to a definition of phases and coherent motions such as waves (sections 2.3.3, 2.3.4). Finally a dynamical description of the motion of a single dust particle is adressed in section 2.3.5.

2.3.1 Charging

Spherical particles suspended into a plasma get charged under the influence of electron and ion fluxes towards their surface. The particles behave like capacitors with a capacitance

$$C_P = 4\pi\epsilon_0 R_P \tag{2.7}$$

where R_P is the particle radius. The charge Q_P of a particle is equals to C_P times a floating potential Φ_S, which depends on the fluxes I_e and I_i of electrons and ions onto its surface. A negative net charge is reached due to the higher mobility of the electrons [2],[5]. This causes positive ions to accumulate around the dust particles and screen their charge. The interaction potential Φ_{IP} between the particles at a distance $\tilde{r}$ is therefore a screened Coulomb potential [6]

$$\Phi_{IP}(\tilde{r}) = \frac{Q_P}{4\pi\epsilon_0\tilde{r}} e^{-\frac{r}{\lambda_D}} \tag{2.8}$$

Usual values of the charge are of the order of some -1000 q_e per μm particle diameter.

2.3.2 Forces Acting on Particles

Due to gravity, the particles would just drop to the ground. To prevent this, the particles are injected between two horizontal, parallel electrodes, at which a RF voltage (usually 13.56 MHz) is applied to ignite the plasma. After ignition fast electrons hit the electrode surfaces and get lost. Due to that the electron density is decreased in that region and a thin sheath with a positive charge density, $q_+n_+ > q-n-$, builds up. This creates a potential increasing monotonic from the electrode to the quasineutral plasma bulk. The net potential in the bulk is zero, so the potential is negative at the electrode surfaces. The resulting electric field E_v points towards the electrode causing an opposite electric force F_v towards the bulk for negative charges in the sheath, while positive ions are attracted by the negative potential of the surfaces. If dust particles are inserted between the electrodes gravity pulls them down, as do the ions streaming downward towards the electrodes (ion drag force). In the plasma sheath region the electric force $F_v = Q_P E_v$ acts on the particles

with a negative charge Q_P and levitates them againts the downward pointing forces. The particles are now trapped vertically between the lower electrode and the quasineutral plasma bulk in the plasma sheath region [7]. In the horizontal direction an electric force $F_h = Q_P E_h$ pointing inwards to the center of the electrode confines the particles. This force is produced by a shaped electrode which creates a parabolic potential well with a higher potential in a circle around the center of the electrode. An horizontally outward force $F_{IP} = Q_P E_{IP}$ is given by the electrostatic interparticle repulsion.

In summary, gravity and ion drag is balanced by the electric force in the plasma sheath, while the confining force acts against the interparticle repulsion as it is schematically shown in figure 2.3.2.

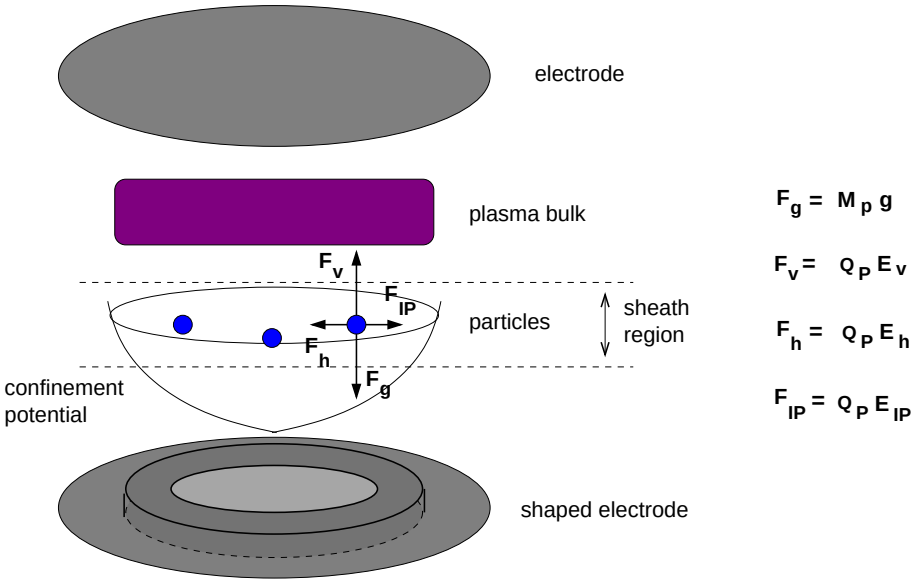

Figure 2.2: External forces acting on a dust particle in a RF discharge. The ion drag force mentioned in the text is not included.

2.3.3 Thermodynamical Phases

In the thermodynamical description, phase is defined by the ratio of kinetic and potential energy. For a wide range of parameters such as particle size, particle density and plasma conditions crystalline states of dust particles in plasmas can be achieved. They have $\Gamma \gg 1$ and are therefore called strongly coupled systems. The structure can be a two or three-dimensional lattice, usual hexagonal close-packed (hcp) or face-centered cubic (fcc) [8], as shown schematically in figure 2.3. As an example, figure 2.4 shows a real image taken from a 2-dimensional plasma crystal in the right panel. In the left panel a triangulation of the particle positions is made, and one can clearly see the hexagonal structure. In the case of a 3-dimensional crystal, it has been found, that the particles of different layers

are often aligned vertically. The reason are ions moving downward towards the negative electrode. The ions stream around a negative charged dust particles, partly captured right beneath the particle thus producing a positive wake field which attracts a particle in the lower layer. The attractive force is asymmetric, it works only on the lower particles (since only beneath a particle a region of higher ion density appears). That way vertical strings of particles are generated which even move together if the upper particle is pushed as it was investigated by [9].

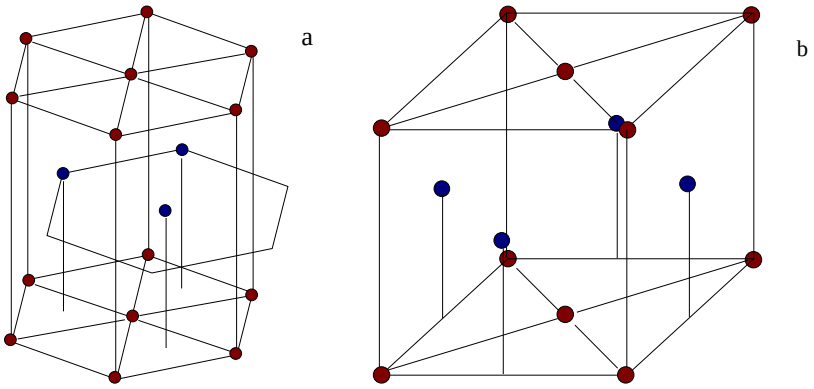

Figure 2.3: 3-dimensional crystal structure: a) hexagonal close-packed and b) face-centered cubic.

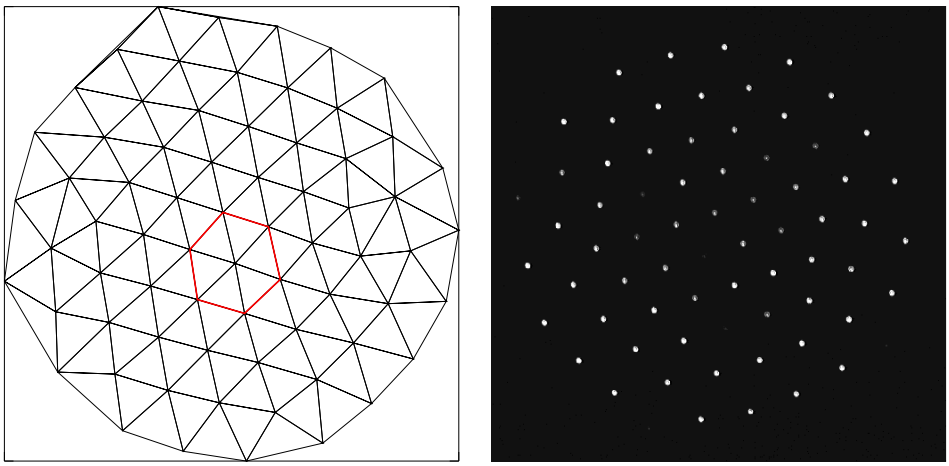

Figure 2.4: Real image of a 2D plasma crystal (right) and corresponding triangulation of the particle positions (left). Marked in red is the hexagonal structure.

Phase transitions to a liquid occur for $\Gamma < \Gamma_c \approx 172$ [2]. This requires an increase of the ratio of kinetic to potential energy. The kinetic energy is determined basically by the particle temperature. Since weakly ionized plasmas are used for the experiments (only $\approx 10^{-7}$ % of the gas atoms are ionized), collisions of dust particles and neutral gas atoms outweigh interactions with charged plasma components. Thus the particle motion

is damped and the dust grains are cooled to the temperature of the neutral gas, which is usually at room temperature [10]. By decreasing the gas pressure and thus reducing the number of neutral atoms, the relation of collisions with neutral gas to charged plasma components gets smaller. The inelastic collisions with the latter heats the dust grains and increases the mean kinetic energy [11]. Other heating processes are the fluctuating electric force of the RF discharge, charge fluctuations and instabilities due to coupling modes [12].

Contributing to the potential energy are the external confining potential and the interparticle potential. This is valid at least if only motion in a horizontal plane is of interest. A decrease of the RF voltage at the lower electrode diminishes the strength and the gradient of the vertical electric field and thus also the radial confining field. The crystal expands in the horizontal plane and the mean interparticle spacing becomes larger. Therefore the mean potential energy of a particle is decreased. The interparticle potential is influenced by the particle size, since the charge is proportional to R_P and thus $\Phi_{IP} \propto R_P^2$.

In summary, by choosing the appropriate plasma conditions and discharge parameters, one can decrease Γ until the crystal melts as observed in [13] or [14]. The first melting transition is not a solid-liquid transition, but to a phase called hexatic. This phase is distinguished by the loss of long-range translational order, while still keeping long range orientational order [3]. As Γ continues to decrease a liquid phase emerges, where only short range ordering appears. In the gaseous phase Γ becomes < 1 at very low plasma densities and high RF voltages no transitional or orientational order is left.

Instead of describing the phase by Γ, which is not very accurate, information based on spatial distribution of particles can be used. This is done by calculating the pair- and bond-orientational correlation functions, $g(r)$ and $g_6(r)$. $g(r)$ is the numbers of particles around a choosen center particle depending on the distance; $g_6(r)$ gives an estimate on the degree of changes in the orientation of the bond angles, dependent on the distance to a particle. The dependence on r of both is characteristic for solid, hexatic and liquid phases[1] [3], and it is easy to get from optical observations.

2.3.4 Waves in Plasma Crystals

Longitudinal and transverse waves have been found in plasma crystals. The longitudinal waves propagate parallel to the particle motion and are compressional. They can be found in all thermodynamical phases of dusty plasmas. The transversal waves propagate perpendicular to the particle motion and have been observed only in the strongly coupled regime of liquid and solid phases. The dispersion relations depend on parameters such as Q_P, λ_D, the damping rate of the neutral gas and the direction of wave propagation and have been studied by [15]. Other wave phenomenons such as shock waves in plasma crystals can be found in [16], for example.

[1] crystalline: $g(r) \propto r^{-\eta(T)}$, $g_6(r)$ =const ($\eta(T) \leq 1/3$)
hexatic: $g(r) \propto e^{-r/\xi}$, $g_6(r) \propto r^{-\eta(T)}$ (ξ: scale length of translational order, $0 < \eta(T) \leq 1/4$)
liquid: $g(r) \propto e^{-r/\xi}$, $g_6(r) \propto r^{-r/\xi_6}$, $\xi = \xi_0$ (ξ_6: scale length of orientational order)

Of interest in this thesis are the 2-dimensional solid plasma crystals. The next chapter will treat the dynamics of such systems.

2.3.5 Equation of Motion of a Single Particle

Suppose we have generated a 2-dimensional (single layer) plasma crystal. The particles are arranged in a hexagonal lattice as in figure 2.4. Each particle can fluctuate around its mean lattice position, depending on the ratio of kinetic to potential energy. The equation of motion can be approximated by the 1-dimensional Langevin differential equation for a driven, damped harmonic oscillator [17]:

$$\frac{d^2r(t)}{dt^2} = -\omega_E^2 r(t) - \nu_{Ep}\frac{dr(t)}{dt} + \frac{1}{M_P}\xi(t) \tag{2.9}$$

$r(t)$ is the particle coordinate relative to its mean lattice site (so called displacement), M_P is the particle mass, ω_E is the Einstein frequency, ν_{Ep} is the Epstein drag coefficient and $\xi(t)$ is a fluctuating force (e.g. RF field, Brownian motion). The Einstein frequency is the frequency of the particle oscillation in its nearest neighbor cage combined with the confining potential and is typically of the magnitude of $3-6$ Hz. For a 1-dimensional oscillating particle with mass M_P and displacement $r(t)$ it can be written in dependence of the forces $\mathbf{F}_i$ acting on the particle due to the neighboring particles i, neglecting external forces [19]:

$$\omega_E^2 = \frac{1}{M_P}\sum_{i=1}^{N-1}\frac{\partial \mathbf{F}_i}{\partial x} \tag{2.10}$$

x indicates an arbitrarily chosen direction.

A rough estimation of ω_E for a screened coulomb potential as in equation (2.8) follows for small deviations r from the mean lattice site. In this case the restoring force F_R can be linearised and a spring constant k can be derived. Then ω_E is given by the relation:

$$\omega_E^2 = \frac{k}{M_P} \tag{2.11}$$

with the particle mass M_P. Later, in chapter 5.1.2.2, k will be derived for a linear chain of particles.

The Epstein drag coefficient ν_{Ep} is the frequency of collisions with neutral gas atoms [18]. It characterizes the damping rate of particle motion. It can be expressed as

$$\nu_{Ep} = \delta\sqrt{\frac{8M_g}{\pi k_B T_g}}\frac{p}{\rho_P R_P} \tag{2.12}$$

Here M_g, T_g and p are the mass, temperature and pressure of the neutral gas, ρ_P and R_P are the mass density and radius of the particles. δ is a factor between 1.0 and 1.44, depending on the way gas atoms are reflected by the particles. Usually 1.44 is assumed.

As a result, the motion of a particle is under the influence of a restoring force due to the interparticle potential, a frictional force diminishing E_{kin} and a fluctuating force increasing E_{kin}. Under some restrictions it can be solved for the mean square displacement $MSD(t)$ [19]. It can be derived from particle coordinates obtained from images by calculating a mean lattice site $\overline{r}$ for each particle by summing over its nearest neighbors, taking the deviation from $\overline{r}$ for each particle in one image, and then averaging over all particles in this image. This is done for each image, giving the time dependent $MSD(t)$. This technique requires a system without diffusion, that means particles should never leave their nearest neighbor cage. An example for the observation of a diffusive system can be found in [20].

In this thesis, not the average displacement will be used, but instead for each particle a time series of displacements $r(t)$ from the mean lattice site is analysed. The mean lattice site of a single particle will be derived independent of the neighboring particles as the average over all positions $r(t)$ of this particular particle. Before passing over to the methods of obtaining the time series, the theory of ergodic behaviour in general and in terms of the application to plasma crystals is treated in the next chapter.

Chapter 3

Ergodic Theory

A physical ergodic system is usually understood – in its simplest form – as a system were the time average of a quantity taken over a long time is equal to the average of the same quantity taken over an ensemble of identical independent realisations of the system at one time.

The following pages will try to explain the connection of this statement to dynamical properties of a physical system. For this purpose, plasma crystals have the advantage that it is possible to directly measure coordinates and velocities, yielding the statistical distributions and giving a direct determination of the phase space.

Section 3.1 introduces some general concepts of describing systems and ensembles, as it can be found in [21] or [22]. In section 3.2 the definition of the ergodic theorem and the conditions for ergodic behaviour are given, following [23] in the naming. Finally in section 3.3 the application of the ergodic theorem with regard to an experimental point of view, in particular for plasma crystals, is discussed.

3.1 Description of a Dynamical System

3.1.1 Hamilton Formalism

In order to illustrate the concept of a phase space, consider the example of a particle moving in a potential well. This particle is the system of interest. It is restricted to the area inside the potential well. At any time it will be located somewhere inside. One could now introduce a phase space for this particle. A phase space is a space in which each state, defined by all variables of a system, occupies one point. As variables, e.g. position or momentum, change during time, the system moves on a trajectory in phase space. For the particle, we assume a 1-dimensional oscillation around the center of the potential (the point where the potential is at its minimum). Therefore we can describe the particle in a 2-dimensional phase space by a phase function (the trajectory) $f(q(t), p(t))$. The variables

$q(t)$ and $p(t)$ are the position and momentum at time t. Since the particle's range of motion is restricted by the potential well, $q(t)$ can not take on every possible value. This also sets a limit on the particle's area in phase space. If furthermore the energy of the particle is conserved, the area in phase space visited by the particle will be determined by its constant energy, setting a limit on $p(t)$. This is the usual classical mechanics: the state of the system is described by its generalized coordinates and momenta $(q(t), p(t))$ and the motion is given by the Hamilton formalism:

$$\begin{aligned} H(q,p) &= \text{constant} && \text{total energy} \\ \frac{dq}{dt} = \frac{\partial H}{\partial p} \quad , \quad \frac{dp}{dt} &= -\frac{\partial H}{\partial q} && \text{equation of motion} \end{aligned} \tag{3.1}$$

One could now describe the particle by setting up its equation of motion and solving them. This would give an exact specification of the system's microscopic state at every time t.
In general, a system of N particles is located in a $2 \cdot d \cdot N$ phase space, where d is the number of degrees of freedom of one particle.
The phase function f depends on the $2 \cdot N$ generalized coordinates and momenta $(\mathbf{q}_1(t), ..., \mathbf{q}_N(t), \mathbf{p}_1(t), ..., \mathbf{p}_N(t))$, where $\mathbf{q}_i(t), \mathbf{p}_i(t)$ are d-dimensional vectors.

3.1.2 Probability Functions

In statistics, ensembles are used. An ensemble is an amount of identical physical systems. The system can be any number of particles. While the classical description treats a system by its equations of motion in phase space, in statistics the ensemble is represented by a probability function

$$F(\mathbf{q}_1(t), ..., \mathbf{q}_N(t), \mathbf{p}_1(t), ..., \mathbf{p}_N(t), t)$$

The probability to find a system of the ensemble in a phase volume

$$dV = dq_1^d ... dq_N^d dp_1^d ... dp_N^d$$

at time t in phase space is given by

$$F(\mathbf{q}_1(t), ..., \mathbf{q}_N(t), \mathbf{p}_1(t), ..., \mathbf{p}_N(t), t) dV \tag{3.2}$$

normalised by the whole phase space volume. One system at time t represents a microstate, while the whole ensemble is a macroscopic state. This leads to thermodynamical description of an ensemble.

3.1.3 Macroscopic Averages

In thermodynamics, systems are described by macroscopic averages of microscopic states. An ensemble of N particles, where each is in its microscopic state $q_i^d(t_k), p_i^d(t_k)$ $(i \in [1, N])$

at a given time t_k yield for a macroscopic quantity $A(q_i^d(t_k), p_i^d(t_k))$ the average of all microscopic states at that time:

$$\langle A \rangle = \langle A(q(t_k)_i^d, p(t_k)_i^d) \rangle_e = \int dV \, A(q_i^d(t_k), p_i^d(t_k)) F(q_i^d(t_k), p_i^d(t_k)) \tag{3.3}$$

where the index e indicates the ensemble average. Since there is no possibility to assign a certain state to one component of the ensemble, all information on the real motion of a single particle is lost.

The aim of ergodic theory is now to connect the thermodynamical quantity of the ensemble with the dynamical (microscopic) states of its subsystems, or in other words to show what conditions have to be fulfilled by a dynamical system in order to exhibit the thermodynamical properties which are given by the ensemble averages. For this purpose, time averages of single systems are introduced (chapter 3.2). From this follows the question, what kind of systems are subject to ergodic theory: it only deals with ensembles in thermodynamical equilibrium. This is essential, since if an average $\langle A \rangle_e$ of an instant has to be compared with an average $\langle A \rangle_t$ taken over time, any nonstationarity in A would influence the time average thus leading to different results.

The next section turns to the ergodic theorem itself, which is the basic part of ergodic theory, and to the restrictions of it to a special group of systems.

3.2 The Ergodic Theorem

The ensemble average of a quantity A was defined in equation (3.3) as the integral of A over all points q_i^d, p_i^d at a fixed time t_k in phase space weighted by the probability $F(q_i^d, p_i^d)$ to find any system of the ensemble at a certain point. It can be interpreted as the whole surface in phase space accessible to the system, since F is zero for all other points.

The time average of A is defined as the integral over all microscopic states $(q_i^d(t), p_i^d(t))$ the system i takes on for the time $t_m \to \infty$, so it is an integral along the trajectory in phase space:

$$\langle A \rangle_t = \lim_{t_m \to \infty} \frac{1}{t_m} \int_0^{t_m} dt \, A(q_i^d(t), p_i^d(t)) \tag{3.4}$$

The ergodic theorem states equality of both averages:

$$\langle A \rangle_e = \langle A \rangle_t \tag{3.5}$$

The existence of the integral over time in equation (3.4) is a mathematical question which is taken account of in books on ergodic theory (e.g. in [23]). However, of interest for the physicist is the condition for application of the theorem and the physical interpretation. Some important conditions are now specified.

1. $t_m \to \infty$
   The first problem occurring for the physicist is the time average over an infinite period, which is not realisable in experiment. But a restriction can be made: every physical effect of interest happens at a certain time scale τ. The total time t_m of measurement and averaging should be much larger than that,

   $$t_m \gg \tau \tag{3.6}$$

   Then the results of averaging should approximate $t_m \to \infty$ good enough.

2. The system must be closed. If not, the probability function F itself would be dependent on time, leading to a change of the density of a volume element in phase space with time (for the case $N = 1, d = 1$) :

   $$F = F(q(t), p(t), t) \to \dot{F} = \frac{\partial F}{\partial t} + \frac{\partial F}{\partial q}\dot{q} + \frac{\partial F}{\partial p}\dot{p} \neq 0 \tag{3.7}$$

   From equation (3.2) it follows, that the probability to find a system at point (q, p) in the volume dV in phase space will change with time. If dV is kept fixed, the probability density in dV has to change. Real physical systems are never perfectly closed systems. The condition can be weakened by the same reasoning as in point 1: the time scales of the change of a measured quantity due to interaction with surroundings should be much larger than the relevant time scale τ. Then the influence should be negligible.

3. Stationarity:
   A measurement of a physical quantity A over a time interval will usually yield a time series of values $A(t)$. In a non-stationary system, a mean value $\langle A \rangle_t$ calculated over consecutive time periods of length dt will change in time:

   $$\langle A \rangle_t = \langle A \rangle_t(t)$$

   If this is compared with an ensemble average at one time, it is very likely to find deviations. Therefore ergodic theory excludes non-stationary systems. From the thermodynamical point of view, this implies systems in equilibrium. Non-stationarity can be a property of the system itself, but it might also be an effect at another time scale as the one of interest, caused by external influences. This is called trend, and indicates a not properly isolated system. If the reason for the trend can be identified as independent of the actual dynamics, and if it does not influence the motion on relevant time scales, it is possible and acceptable to remove it. One example could be an external force which can not be abolished, like the Earth magnetic field. Trends are a large problem in the system examined in this thesis, as we will see in chapter 5.2. Essential is the time scale of the trend, as was discussed in point 2.

4. No interactions between systems of an ensemble. The systems used for ensemble averages must be independent realisations of the system. That is the definition of an ensemble. If there are e.g. correlations between particles, the particles are not independent systems, but the whole set of particles has to be seen as the system.

Under the above circumstances a system should exhibit ergodic behaviour. At least, this is usually assumed, but a general proof is difficult. One attempt to explain the equality of time and ensemble averages has been made by Boltzmann with the **ergodic hypothesis**. He claimed, that a system represented by a phase space trajectory will pass every point in phase space allowed by its energy for $t \to \infty$. If this be so, the whole accessible phase space would be filled, and the time average taken along the trajectory would for sure be equal to the ensemble average taken over the energy surface. But it has been shown that this assumption is wrong. Also the **quasi-ergodic hypothesis** is not very applicable. It says, that it is enough that the phase space trajectory is dense. Dense means, the trajectory does not reach every point in phase space, but comes arbitrarily close to each (in the mathematical sense). But here a general proof is missing, though it seems to be valid for a small class of systems [23].

Worth mentioning is the **asymptotic ergodic theorem** introduced by Khinchin [23]. The general ergodic theorem requires that equation (3.5) is fulfilled by all integrable quantities A. Only then the system is called ergodic. For each system, some quantities might be of more physical importance than others, so Khinchin restricted the number of quantities for which equation (3.5) has to hold to those of most physical interest and in spite of this restriction calls the system ergodic. He also does not demand a strong equality, but he allows a small difference ϵ between $\langle A \rangle_e$ and $\langle A \rangle_t$, which goes to zero asymptotically if the number of degrees of freedom goes to infinity:

$$\langle A \rangle_e - \langle A \rangle_t < \epsilon \to 0 \text{ for } N \to \infty \tag{3.8}$$

The assumption is that relation (3.8) is violated only on a small set in phase space if one uses only quantities of physical importance. The size of ϵ depends on the measure used in phase space, and can be derived in terms of set theory. Since Khinchin's theorem is completely mathematical, it is difficult to apply to real physical systems and has only been proved for a small class of systems.

3.3 Application of the Ergodic Theorem

3.3.1 Phase Space of Particles in Plasma Crystals

Since plasma crystals can be observed visually, by taking consecutive images of the crystal a direct measurement of the coordinates (x, y) and velocities (v_x, v_y) in one plane is possible. Thus one can measure a 4-dimensional phase space (x, y, v_x, v_y) directly for one particle. The single particle is from now on seen as the system, while the whole crystal is the statistical ensemble. A 4-dimensional phase space is difficult to represent, but the problem can be simplified. In a crystal, a mean lattice site can be assigned to each particle. The particle can only move in a small region around this, because the potential well of the surrounding particles repels it. So one can make a transformation to a coordinate system with the mean lattice site as the center and describe the particle motion with

polar coordinates (r, ϕ) in this new system. This is done for each particle, except edge particles. These should not be compared with inner particles since they are subject to other boundary conditions (particles on one side, confinement potential on the other). A restriction is now made by assuming radial symmetry for each particle. This is valid, if the potential well of the surrounding particles is approximately uniform. Then the only relevant motion is the deviation from the mean lattice site, r.
The velocity v is assumed to represent the thermal motion of the particles and follow a Maxwellian distribution. This kind of distribution is Gaussian (or normal) and depends on temperature and particle mass only. It will be explained in chapters 4.1 and 5.4.1 in detail. Here it should be noted, that an ideal Maxwellian distributed velocity is independent of the position r. Thus it is possible to examine r as the only quantity, reducing the phase space to one dimension. The velocity, if Maxwellian, could be analysed independently.

For the statistical methods used later, this phase space reduction will be done, but it has to be kept in mind, that any result is valid for the reduced space, and cannot be passed over to the real 4-dimensional phase space or any higher embedding of a particle. That means, if a result is found for r, it is valid for r only and should not be interpreted as anything else. If for example r or v exhibit equal behaviour for a single particle in time and for the ensemble, that accounts only for the absolute values of this quantities, since we are in a 1-dimensional space. It is not necessarily correct to follow from this that particles in plasma crystals are ergodic, but the ergodic theorem is fulfilled by that particular quantity r respectively v. This is what will be referred to as 'ergodic behaviour with respect to a quantity'.

3.3.2 Conditions of Ergodic Behaviour

In section 3.2 general conditions have been enumerated which have to be fulfilled by a system and an ensemble of systems to exhibit ergodic behaviour. This will be repeated here in particular for the plasma crystal with respect to the experimental possibilities.

1. Measurement time:
   The measurement time must be much longer than the typical timescales of interest. These are mainly given by $\tau_E = 2\pi/\omega_E$, the time scale of oscillations in the potential well, and by $\tau_{Ep} = \nu_{Ep}$, the time scale of damping by collisions with neutral gas atoms. $2\pi/\omega_E$ and ν_{Ep} are typically of the order of 3 - 5 and 1 Hz [15], which leads to timescales less than 1 s. It is no problem to exceed that time with the measurement time.

2. Closed system:
   A dust grain levitated in a plasma is not a closed system. A lot of forces act on a particle, but the important point is that the particle energy stays constant. The particle in a crystal is in equilibrium with its surroundings and achieves a steady state regarding to the energy short after it was injected into the plasma. The particle

is cooled down by neutral gas damping, but in opposite it gets heated by inelastic collisions with e.g. electrons [17]. So a particle can be seen as a system with a constant energy, and thus be treated as in a thermal equilibrium with a surrounding isolated outwards. Still the question remains, whether or not the energy transfers have an influence on the motion of interest.

3. Stationarity:
   Plasma crystals reach equilibrium very fast within a few seconds after the dust grains are inserted into the plasma [24]. If the external experimental parameters are kept constant, the state of the crystal does not change. The ensemble of particles could be assumed to be stationary from that point. But some effects which will be explained in section 5.2 lead to trends in the time series of particle coordinates. These have to be identified and subtracted.

4. Interactions:
   Interactions between the charged particles of a plasma crystal are the reason why crystals exist. One would expect that in this case it is not valid to take the crystal as an ensemble of independent realisations of a system. But on the one hand, the influences of the particles on each other could be seen as a fixed confining force which is the same for all particles (except edge particles). Then each particle sits in its nearest neighbor cage, while the neighboring particles do nothing else as creating a potential well. But if there is a correlated motion of particles inside the crystal, this should destroy ergodicity, since then the ensemble averages at each time would reveal trends related to the correlated motion, while these trends could average out for the time series measurements of a single particle

The last point shows the difficulty in the application of ergodic theory to plasma crystals as ensembles: The condition of independent systems can not be fulfilled for these strongly coupled systems. But what can be shown is how strong the interactions influence quantities derived from the coordinates. In other words: is it valid to do averages over all particles and all times to derive for example the particle temperature, or is it necessary to distinguish between time and ensemble averages due to correlations apparent in the ensemble averages.
In this thesis, we will not calculate any averages, but compare the distribution of measured deviations r from the mean lattice site of a single dust particle in time and of all particles in one image. The same will be done for the velocities v. The distributions will be examined by statistical methods such as the Kolmogorov-Smirnov and Kuiper test statistics, explained in section 5.5.

Chapter 4

Experiment and Data Preparation

In section 4.1 the basic experimental setup for plasma crystal experiments is described and in section 4.2 a short description of the particle tracking is given. The main focus after that is the identification of experimental errors and their magnitude in section 4.3. Some basic analysis techniques are summarized in that section, too. Then a rough estimation of the best range of experimental parameters is carried out in section 4.4 with respect to the expected measurement errors and the quantities of interest, namely the displacement from the mean lattice site r and the velocity v.

4.1 Basic Setup

An image of the experimental setup is shown in figure 4.1. Figure 4.2 shows sketches of the setup from the top and side few. The specifications are explained in the text below.

All experiments were performed in a GEC[1] RF-Reference Cell. This is a standard plasma chamber for experiments with dusty plasmas [25], shown in figure 4.1. The GEC cell is a high vacuum chamber with two horizontal electrodes with a separation of 4.7 cm between which the plasma is ignited. The lower electrode has a diameter of 10 cm and is capacitively connected to the electronics for generating the RF field. A cap can be laid on this electrode to manipulate the gradient of the potential. The upper grounded electrode consists of a metal ring with a glass inlay in the middle. The glass is coated with a conductive layer of ITO (Indium Tin Oxide). The purpose of the transparent upper electrode is the possibility to observe the crystal from above with a camera.
Neutral gas flow into the chamber is set by a mass flow controller in the range of 0.1 to 10 sccm (standard cubic centimeters). The gas pressure can be controlled by setting the position of a valve which leads to the vacuum pump. Here a turbomolecular pump compresses the gas first, which is important for reaching a low vacuum ($\approx 10^{-5}$ Pa) between experiments to reduce impurities (see figure 4.2).

[1] gaseous electronics conference

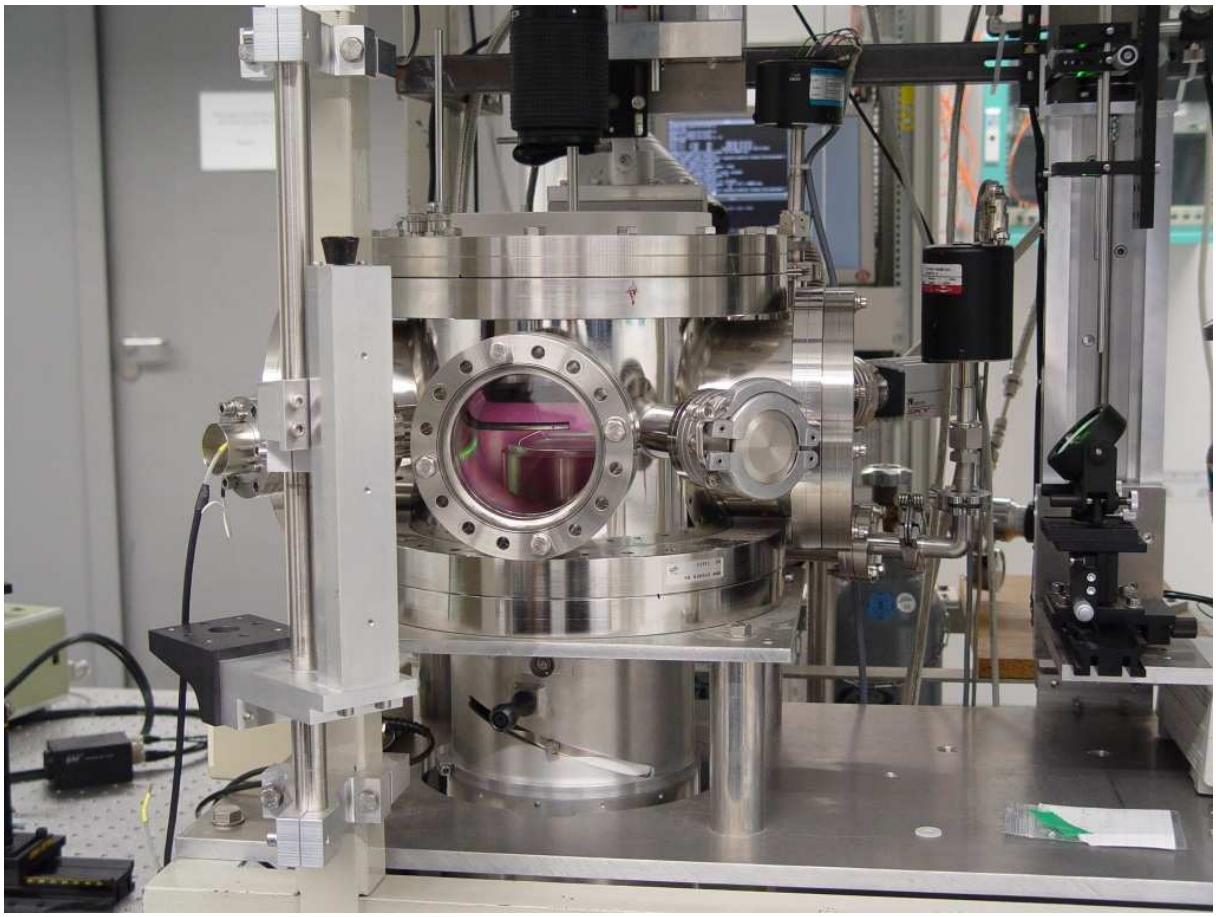

Figure 4.1: Image of the GEC cell used for experiments.

Dust particles are injected by a shaker installed on the top flange and reaching into the chamber. It can be moved over the lower electrode for particle injection. A thin wire of $\approx$ 7 cm length was installed horizontally. It could also be moved over the electrode and is used to push particles aside. This is necessary for experiments with single layers, since after particle injection always some particles are found in other layers. They can be pushed away by moving the wire and thus disturbing the potential.
Through a window on the side of the chamber the particles are illuminated by a laser. The laser beam shines in a horizontal sheet into the chamber between the electrodes (figure 4.2).
Some details are given in the following paragraphs.

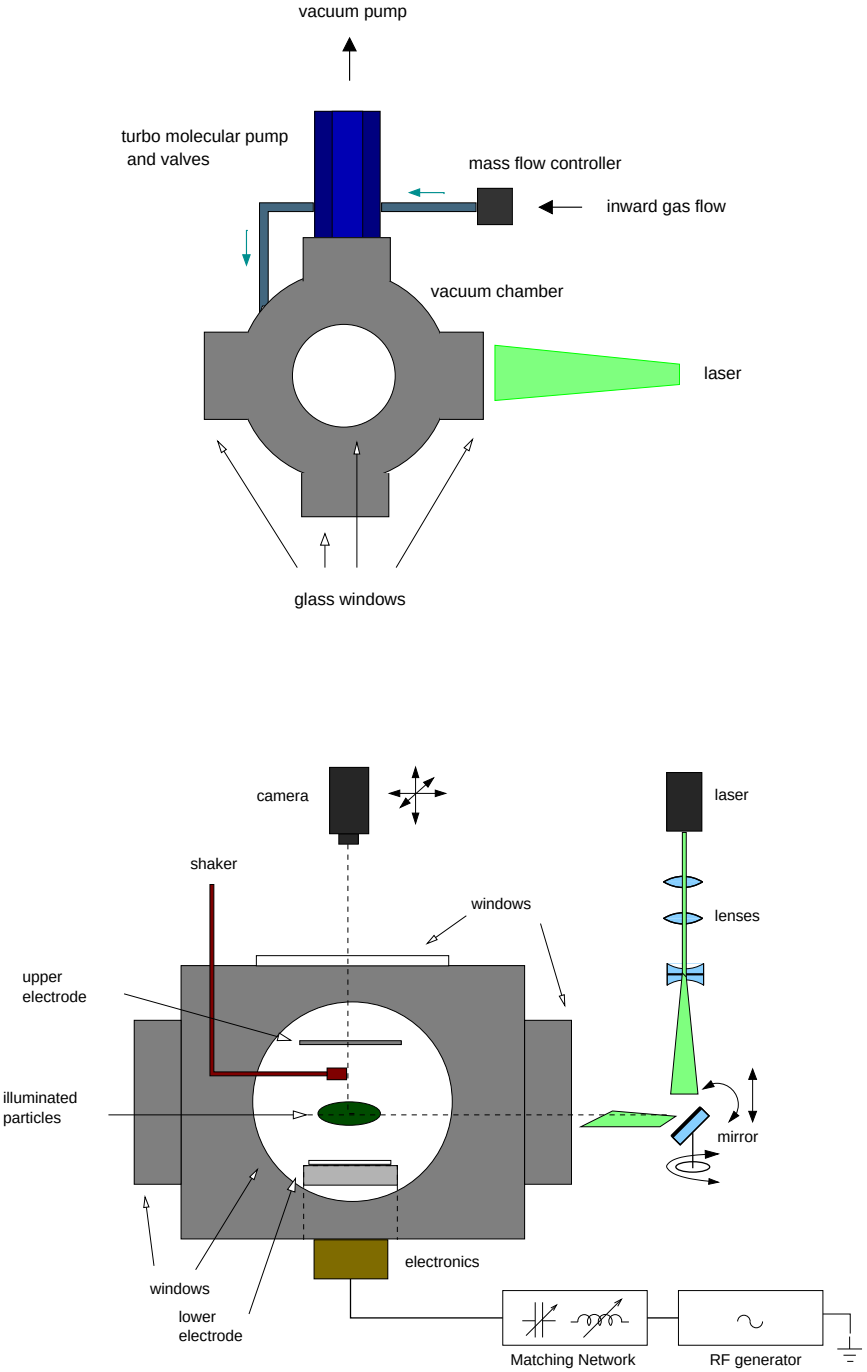

Figure 4.2: Top: Schematic top view of the experimental setup. Bottom: Schematic side view of the experimental setup

Electronics A radio frequency (RF) generator running at 13.56 MHz supplies a high frequency voltage to the lower elcetrode. In between a matching network is installed (indicated in figure 4.2). It consists of a coil and three capacitors which can be adjusted to get the optimal relation of forward and reflected power. Due to the capacitively coupling to the RF generator the lower electrode acquires a negative self bias after the plasma is ignited, which is caused by the (negative) net current of electron and ion fluxes onto the electrode surface.

Both self bias and peak-to-peak values of the RF voltage and current are displayed on an oscilloscope. The power of the RF field determines the strength of the vertical electric field and the horizontal confining potential by influencing the amount of electrons moving to the electrode surface. Therefore the levitation height and the horizontal extension of the crystal can be influenced by changing the RF power. The horizontal confinement is produced by a cap on the lower electrode, as shown in sketch 4.3. The cap has the diameter of the electrode of 10 cm and a height of 5.8 mm. A cavity in the center with diameter 58.1 ± 0.01 mm and a depth of 1.2 ± 0.01 mm manipulates the horizontal potential and produces a parabolic potential with the minimum in the center of the electrode. The particles see an increasing potential if they move away from the center and thus are confined.

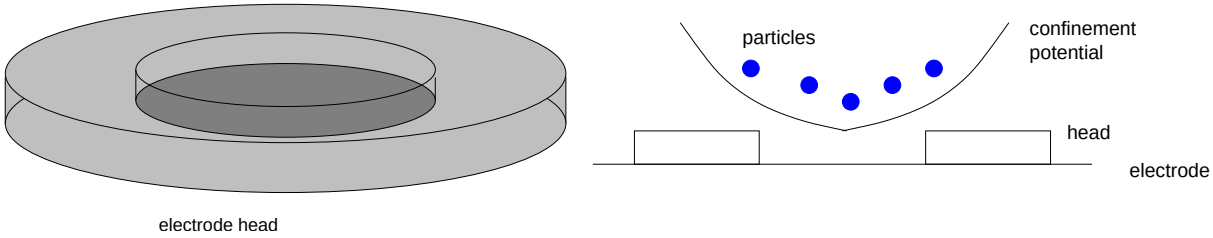

Figure 4.3: Electrode cap for manipulating the horizontal potential

Illumination The laser used for illumination was a $MoYO_3$ laser with a maximum power of 500 mW and a wavelength of 532 nm. It is mounted vertically, together with two convex and one concave lens (sketched in figure 4.2). The lenses expand the beam horizontally and focus it in the vertical direction. The vertical width of the beam at the focal point is approximately 100 μ m. A mirror mounted on a slide deflects the laser beam into the chamber. It can be moved vertically to the height of the particle cloud, and it can be rotated around the vertical and the horizontal (in direction to the chamber) axis. Before starting an experiment, lenses and mirror are aligned such that the laser sheet is parallel to the elcetrodes and the vertical focal point is in the center of the lower electrode.

Light Scattering by particles If electromagnetic waves hit an object, they induce dipoles by exciting charges on the surface. The dipoles oscillate with the frequency of the wave, and thus emit radiation in all directions. This is what one sees as scattered light. If the object is much smaller in extension than the wavelength of the incoming light, it behaves like one or just a few dipoles. The emitted waves are all in phase since there is nearly no spatial difference in the scattering regions, while the intensity of scattered light is proportional to the fourth power of the wavelength (Rayleigh-scattering).

In our case we have particles much larger in size than the laser wavelength. Here a lot of point-like dipols are excited on the surface. Each of the dipoles emits radiation in all directions. Due to the spatial extension of the particle, phase differences occur for scattered light coming from different regions of the particle. The emitted light can interfere, and minima or maxima of the scattered intensity appear. The intesity of scattered light is angle dependent and is strongest in the forward direction. This process is called Mie-scattering. Details are given in [26].

To give an impression on the particle visualisation, figure 4.4 shows an image of a plasma crystal levitated above the electrode and illuminated by the laser. The images has been taken from the side of the chamber.

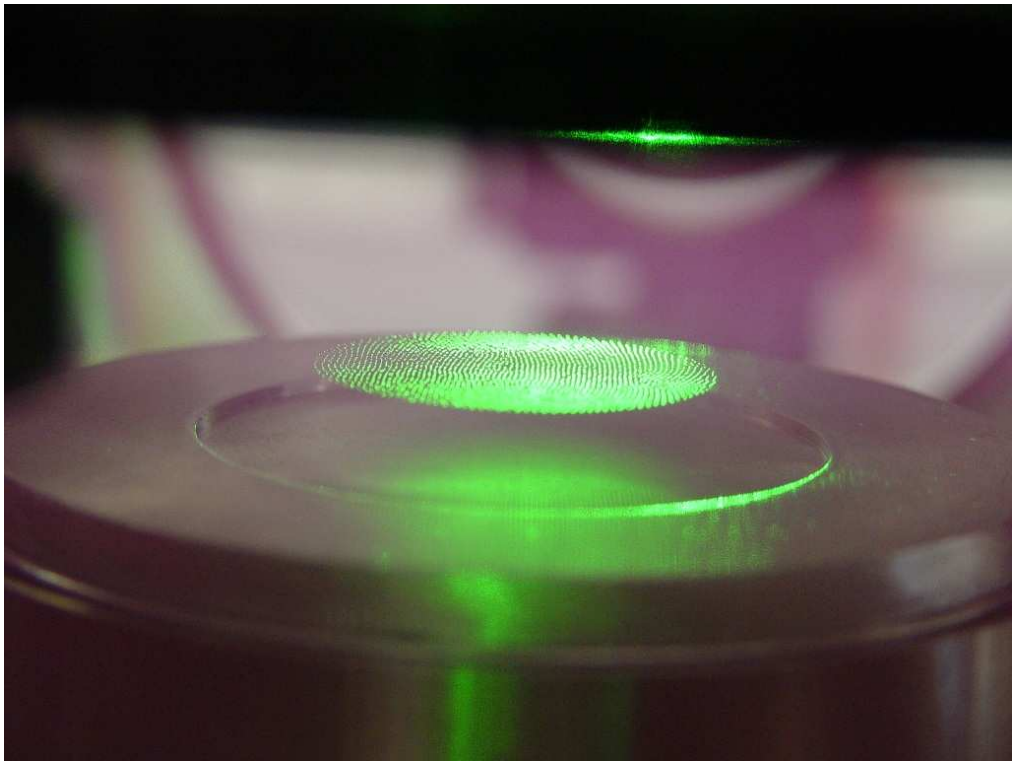

Figure 4.4: Single layer plasma crystal illuminated by the laser.

Camera A plasma crystal can be observed optically. This gives the possibility of direct measurement of the motion of particles in a lattice structure. To reduce the discreteness of measurement a camera with a high frame rate is needed. For optimal precision of the particle positions a high spatial resolution of the CCD chip is useful. The camera used is a CCD (charged coupled device) camera with a progressive scan interline transfer CCD chip. A CCD chip consists of cells or pixels out of a semiconducting material. When exposed to light, an amount of electrons proportional to the light intensity is excited separately in each cell. This leads to a voltage, which is read out at the end of each line for each cell, and interpreted as a brightness value.
The chip used provides a high vertical resolution by non interlaced scanning. That means, each line is scanned with a maximum frame rate of 30 fps (frames per second), so the vertical resolution is the full number of lines. This is accomplished by two separate channels to which the chip lines are alternately assigned. Both channels can be calibrated by changing the offset voltage until the image shows no differences between the lines (if not calibrated, horizontal stripes can be seen which would influence the particle tracking).
The output of $1024 \cdot 1024$ pixel black and white images with an effective photosensitive area of $1003 \cdot 1012$ pixel and a depth of 10 bit is directly written into streaming files to the computer storing device.
The spatial resolution (or magnification) depends on the lens used and on the distance to the object. It has been measured separately for each experiment by recording a millimeter scale at the distance used in the experiment. Since the chip has square pixels of size $9 \cdot 9$ μm, resolution is the same for the horizontal and vertical direction.
A filter for the wavelength of the laser (532 nm) is used to minimize the amount of light reflected into the chip per chance. It has a transmittivity of $T = 53$ % at $\lambda = 532$ nm and $T = 0$ % for $\lambda \geq 545$ nm or ≤ 515 nm. So it also cuts out all other wavelength such as plasma glow or day light, which could overlay the images.
The particles are seen as bright spots of a few pixels diameter in the images. With a pixel size of 9 μ m and a particle size of a few μ m one would expect one illuminated pixel per particle. In fact in the images the particles have sizes of up to 10 pixels in diameter. This enlargement is for example caused by diffraction and aberration in the optical components of the camera lens. Errors of this kind are likely, since the resolution of camera and lens are at the limit for objects of the chip cell size.

The next section will treat the extraction of data from the images. This and all other analysis was performed with the programming language IDL. The tracking was already implemented, but had to be adjusted to work with large data sets as those produced for this thesis.

4.2 Particle Tracking

The data acquired in an experiment consist of images (or frames) of the crystal as shown in the right panel of figure 4.5. In these, particle trajectories have to be found. This is done

in two steps. First, in each frame all visible particles are searched. A particle is identified as an accumulation of bright pixels. The minimum diameter expected for a particle (in pixels) and an intensity threshold are set to increase the accuracy of the algorithm by rejecting small bright spots arising from reflections and by excluding the background intensity. Values for diameter and threshold are found by hand for each experiment. The particle coordinates are then derived by taking the intensity weighted center of the area of all pixels belonging to one particle.
In the second step, each particle found is tracked through the frames by assigning the particles in consecutive frames to each other, if the spatial distance between them is small enough, that means if it is likely that the particle moved this distance between two frames. Since the particles in the crystal are more or less fixed to their lattice sites, this technique gives good results. Each particle is given a unique number, and thus can be identified in each frame (see figure 4.5, left panel). The coordinates, particle radius and mean intensity are stored in an array.

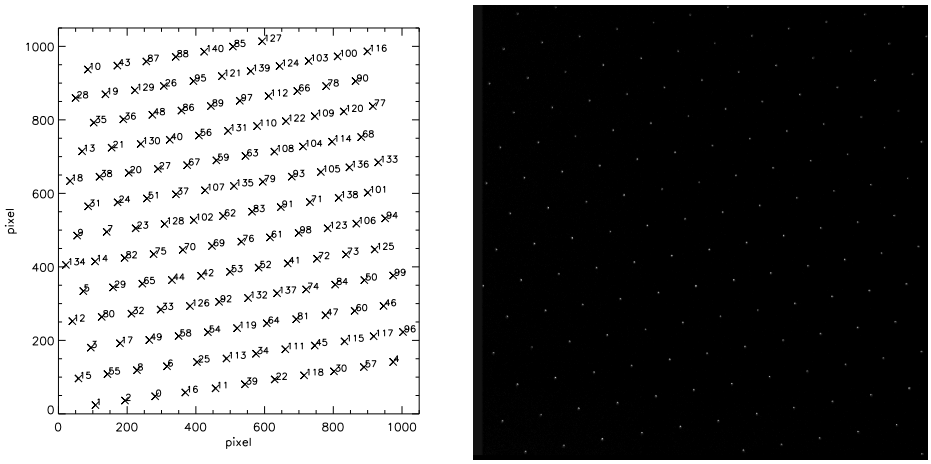

Figure 4.5: Image of a 2D plasma crystal (right) and numbering of particles after the tracking (left).

The result of an experiment thus consists of particle coordinates in the images. Since all analysis will be done on the coordinates or quantities derived from them, the main question is how exact these coordinates are and what kind of error in the positions is to be expected. This is the topic of the next section.

4.3 Experimental Errors

In general, measurement errors can be divided into systematic and random errors [27]. Systematic errors affect the whole measurement in the same way, e.g. a power fluctuation results usually in a radial movement of all particles at that time. Systematic errors should be excluded if possible during the experiment by keeping all parameters constant.

To detect any irregularities, the important experimental parameters should be recorded while taking measurements.

4.3.1 Gaussian Error Distribution

Random errors a more difficult to handle, since they exist nearly everywhere as a noise level. This kind of error is described by a Gaussian (or normal) probability distribution. By measuring a quantity x repeatedly N times while x does not vary itself, but is subject to a random error, the measured values x_i would be distributed like

$$f(x) = \frac{1}{\sqrt{2\pi}\sigma_x} \cdot e^{-\frac{(x-\overline{x})^2}{2\sigma_x^2}} \qquad \text{Gaussian distribution} \tag{4.1}$$

$$\sigma_x = \sqrt{\frac{1}{N-1}\sum_{i=1}^{N} |x_i - \overline{x}|^2} \qquad \text{standard deviation of } x \tag{4.2}$$

$$\overline{x} = \frac{1}{N}\sum_{i=1}^{N} x_i \qquad \text{mean of x} \tag{4.3}$$

$f(x_i)$ gives the probability to get a certain value x_i. Thus the x_i are spread around a mean value $\overline{x}$. The standard deviation σ_x is a measure of the width of the distribution and 68.3 % of all points are located in the interval $\overline{x} \pm \sigma_x$. Therefore, as a measure of the random error δx of a variable x, the standard deviation is taken as a good estimate: $\delta x = \sigma_x$. This error has to be propagated through each calculation with the data as follows.
If two independent variables x and y, with random errors δx and δy, are measured, then the errors propagate into a quantity $A(x, y)$ yielding an error δA given by

$$(\delta A)^2 = \left(\frac{\partial A}{\partial x}\delta x + \frac{\partial A}{\partial y}\delta y\right)^2 \tag{4.4}$$

$$= \left(\frac{\partial A}{\partial x}\delta x\right)^2 + \left(\frac{\partial A}{\partial y}\delta y\right)^2 \tag{4.5}$$

Where 4.5 holds for uncorrelated errors δx and δy. The term $\frac{\partial f}{\partial x}\delta x \cdot \frac{\partial f}{\partial y}\delta y$ vanishes in that case.

For finite N, the mean and standard deviation are subject to statistical uncertainties. The difference between an uncertainty and a random error is, that the error has a source, but the uncertainty appears because of the finiteness of the number of measurements. If a randomly distributed variable x is measured $N = 5$ times, it is possible to measure by chance only values from the left side of the error distribution. The mean is then shifted to that side. By increasing N this get more and more unlikely, and the measured x_i should approximate the continuous distribution $f(x)$. The statistical uncertainties in $\overline{x}$ and σ_x

can be expressed as:

$$\delta\overline{x} = \frac{\sigma'_x}{\sqrt{N}} \tag{4.6}$$

$$\delta\sigma_x = \frac{\sigma'_x}{\sqrt{2\cdot(N-1)}} \tag{4.7}$$

where σ'_x should be either known from a theoretical model for the distribution of x or it can be approximated by σ_x calculated from the data x with equation (4.2) for large data sets. The proof for the validity of this approximation can be found in [27].
The measured value $\overline{x}$ is an approximation of the theoretical mean $\overline{x}_{th}$ one would expect from a theoretical description of the system (for example a gaussian distribution with mean zero). $\overline{x}_{th}$ should lie in an interval $\overline{x} \pm z \cdot \sigma_x/\sqrt{N}$, if the theory is correct. The interval around $\overline{x}$ given by the standard error of the mean times a factor z is called the confidence interval. By choosing z, the width of the confidence interval can be adjusted with respect to the desired accuracy. The larger the interval is, the more likely it is that it includes the expected value $\overline{x}_{th}$, but the statement is not as strong then (e.g. one can choose $z = \infty$, but then the statement is useless because everything lies in this interval). Usually a confidence interval of $\pm 1.96 \cdot \sigma_x/\sqrt{N}$ is chosen, corresponding to a statistical security of 95 %. That means that in 95 % of all cases the conclusion that $\overline{x}$ is a reliable estimation of $\overline{x}_{th}$ is correct if $\overline{x}_{th}$ actually lies in the confidence interval. Usually different errors contribute to a measurement, for example the statistical uncertainty and k independent random errors δx_k. In this case, the errors sum up like:

$$\delta x_{tot} = \sqrt{(z\delta\overline{x})^2 + \sum_k \delta x_k^2} \tag{4.8}$$

4.3.2 Analysis Methods

If possible, before performing experiments the expected measurement errors should be found out. This has been done for the plasma crystal experiment. Before discussing that, some basic analysis procedures such as binning data into histograms and fitting a theoretical function as a model to a data set are described.

4.3.2.1 Histograms

An approximative probability distribution for a variable x measured N times can be obtained by counting how often x happens to be in a certain interval $x \pm dx$ (also called a bin) within the scale of possible outcomes of the measurement. This number, divided by N, gives the probability to find any measured x_i in the interval $x \pm dx$. By repeating the measurement very often, a more or less continuous distribution should emerge, if the data can be described by probability functions in fact.

The uncertainty is the width of the bin. Thus a small bin size is desired, but to approximate a continuous probability function, the bins should be large enough to contain enough points (at least more than one), and to smooth small fluctuations. For data which are assumed to follow a normal distribution, one usually takes a range of $\pm 3 \cdot \sigma_x$ around the mean as a reliable scale for possible values x_i. This should only be done if in fact most of the data are within that interval. Otherwise an appropriate range should be chosen. This interval is divided into N_{bin} bins with respect to the amount of data points, and the data points falling into each bin are counted and normalized by N yielding the histogram $h(\zeta)$. ζ represents the middle points of the bins and is used here to distinguish it from the measured x.
$h(\zeta)$ can now be compared with an assumed theoretical probability distribution $f_{th}(x)$ to test if it can be used as a model for the data. Usually one estimates the parameters relevant for $f_{th}(x)$ (e.g. mean and standard deviation for a gaussian distribution) from the data and uses these as start values for a fit of the function $f_{th}(x)$ to $h(\zeta)$ at the discrete points ζ_j. This procedure is described in the next section.

4.3.2.2 Fit Procedure

Starting from a theoretical function $f_{th}(x, a_1, .., a_m)$ dependent on m parameters, one tries to find the parameters $a_k, k \in [1, m]$ such that the resulting values of f_{th} are the best approximation of a given $h(\zeta)$. The fit procedure used was a combination of a least square fit and a gradient expansion algorithm. It is implemented in IDL and works roughly as follows (see [28] chapter 15):

1. Choose a model f_{th} for the fit. The model can be any mathematical function assumed to be the right one for $h(\zeta)$. The model function must depend on the variable x and on m parameters a_k.

2. Estimate good starting values for the parameters $a_{k,0}$ and calculate the function values $f_{th}(\zeta, a_{1,0}, ..., a_{m,0}) = f_{th}(\zeta, \mathbf{a_0})$ at the points ζ for these.

3. Calculate the least squares or χ^2 test statistic from $h(\zeta)$ and $f_{th}(\zeta, \mathbf{a_0})$ which is defined as
$$\chi^2 = \sum_{j=1}^{N_{bin}} \frac{(h(\zeta_j) - f_{th}(\zeta_j, \mathbf{a_0}))^2}{\sigma_j^2} \tag{4.9}$$
σ_j is the statistical uncertainty of each data point j. For a histogram the uncertainty is of the order of the bin size. χ^2 is a measure for the difference between both function. If they agree good enough, the fraction becomes 1 (then the difference is of the size of the uncertainty) and χ^2 is of the magnitude of N_{bin}.

4. Now the derivatives $\frac{\partial f_{th}}{\partial a_k}$ are derived yielding the change of χ^2 for a change in the

parameters:

$$\frac{\partial(\chi^2)}{\partial a_k} = -2\sum_{j=1}^{N_{bin}} \frac{h(\zeta_j) - f_{th}(\zeta_j, \mathbf{a_0})}{\sigma_j^2} \frac{\partial f_{th}(\zeta, \mathbf{a_k})}{\partial \mathbf{a_k}} \tag{4.10}$$

The aim of the fit procedure is to change the a_k in the direction of the gradient as long with respect to minimize equation (4.10) until the change of χ^2 is below a user supplied tolerance level. Then $f_{th}(\zeta, \mathbf{a_l})$ with the latest $\mathbf{a_l}$ is taken as the best estimate for $h(\zeta)$.

One comment on the interpretation of χ^2 is given. χ^2 should be of the magnitude of the number of bins N_{bin} minus the number of constraints N_{con} arising from the theoretical model. N_{con} is the number of independent parameters of the fit function. Then $\nu = N_{bins} - N_{con}$ is called the number of degrees of freedom and $\chi^2_\nu = \chi^2/\nu \leq 1$ is the condition for a good fit. χ^2_ν is called the reduced χ^2.

4.3.3 Measured Error Distribution

The two main sources contributing to the experimental error in plasma crystal experiments are the spatial discreteness of the measurements and the pixel-noise of the camera. The first is the uncertainty of the estimation of particle coordinates due to the finite extention of the CCD chip cells. The second one arises from the finite temperature of the chip, which causes the intensity values of the chip cells to fluctuate due to thermally excited electrons. This effect is called pixel-noise and is present also if no light shines on the chip. It can be examined by taking 'black' images while the lens is closed which allows a direct investigation of the pixel-noise.

Another approach of the error estimation, which includes nearly all sources, is the following: Some particles are dropped on the electrode surface while no RF field is applied and are illuminated with the laser. A series of images is taken and the particles are tracked with the same algorithm used for all other data. Now for all particles the differences from one frame to the next are taken. Since the particles do not move, the differences should be zero. Any deviation from zero gives an estimate of the effective error (caused by pixel-noise, tracking errors or vibrations of the experimental setup). The result is shown in 4.6 a). A histogram of all differences has been made, and a Gaussian distribution as in equation (4.1) has been fitted to the curve with σ_x and $\overline{x}$ as fit parameters. The χ^2_ν of the fit was 1.21 and thus a bit larger than the optimum of 1.

By examining the image one can see that the gaussian distribution seems not to be the best model for the error distribution, since the tails are not flat, but have local maxima symmetrically around zero. It has been found that they appear only for the intensity weighted tracking. If the tracking is done with a geometrical estimation of the particle location, the total error is larger but Gaussian. This problem will be treated below.

Another problem becomes visible in the close-up of the error distribution in plot 4.6 b). The middle peak also has broad tails deviating from Gaussian. It appears that two

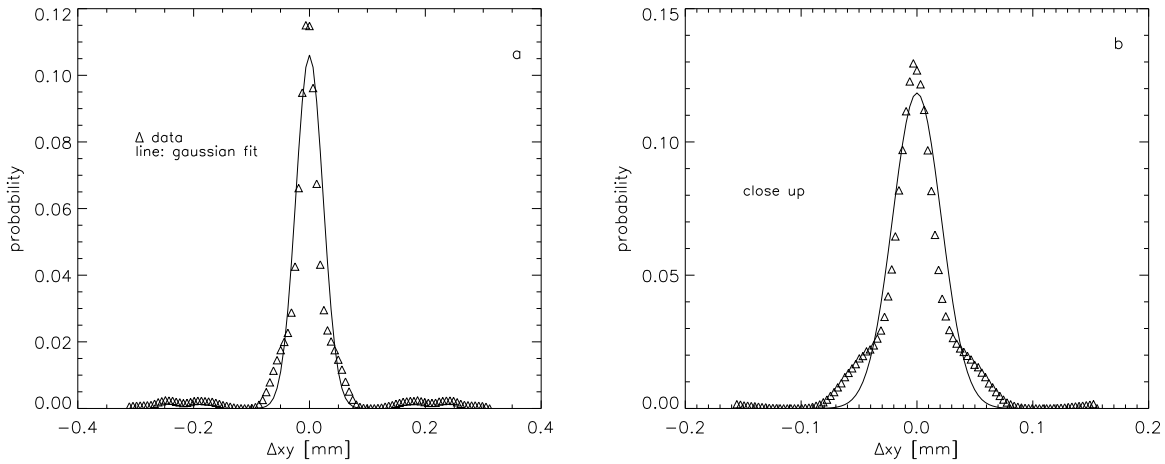

Figure 4.6: Left: Random measurement error distribution (normalized to unit area) and gaussian fit, Right: Close-up of the inner part of the error distribution

Gaussian distributions contribute to the error. In figure 4.7 the error distribution has been computed separately for the x and y direction and reveals a different error for each direction. Here the χ^2_ν was 0.89 for the x, and 0.33 for the y-direction, so both fits can be accepted. The standard deviations σ_x and σ_y as an estimation of the errors are listed in table 4.1. The values derived from the data by equation (4.2) are given for comparison.

	fit	data
σ_x [pixel]	0.013	0.046
σ_y [pixel]	0.046	0.094

Table 4.1: Standard deviations obtained by the fit and calculated from the data directly

The difference of errors in x and y was not expected, but could be explained by the CCD chip of the camera. It has two channels for readout while the consecutive lines are alternately attached to one channel. If the channels have a different offset the intensity values will jump up and down from line to line, which is the y-direction. This could expand the error distribution for y. Since the effect of changing the offset seems to be intensity dependent, is is difficult to completely prevent that difference.

Returning to the outlying maxima, it has been observed in a test experiment, that they occur in principal for badly illuminated particles, e.g. particles which are at a slightly different height than the rest and thus at the edge of the laser beam. Figure 4.8 shows an image of this test experiment, and the particles with broad trails are marked in the plot of particle positions on the left. One can see in the right image, that these particles are nearly not visible. In that experiment, the error seemed to be even larger than the particle

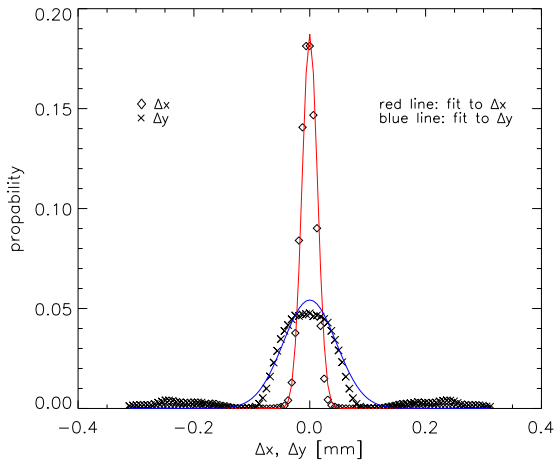

Figure 4.7: Error distribution (normalized to unit area) and Gaussian fit estimated separately for the x- and y-direction

motion. To diminish this error, attention was payed to obtain a good illumination of the whole particle layer during the experiments.
For further experiments, a flatter confining potential could be helpful. The confining potential is parabolic and particles in the center are levitated not as high as particles at the edge, thus leading to problems with uniform illumination (in figure 4.8 this effect can be seen, the marked particles are either at the center or the edges).

To take into account the dependence on the direction in the image and possible effects due to the tracking, an error of 0.1 pixel is taken as the error in the particle positions for both x and y.

$$\delta x = \delta y = 0.1 \text{ pixel}/m = 0.9 \ \mu\text{m}/m \tag{4.11}$$

m is the magnification of the image. Equation (4.11) rather overestimates the values obtained by the fit. The statistical uncertainty of δx was smaller than 10^{-5}. The quantity in μm is obtained by multiplying with the pixel size 9 μm of the CCD chip cells. From now on, only the expression δx is used for the error of x and y.

4.4 Estimation of Experimental Parameters

The random error pretends a particle motion where there is none. That might be misleading in the interpretation of data. Parameters like gas pressure, RF power, magnification and particle density must be chosen such, that the real particle motion exceeds the error far enough to be uniquely identified. In this section some restrictions for the parameters are derived. The result of this chapter has to be seen as a rough estimation. It is used only for getting an idea of the range of parameters to be set in the experiment in order

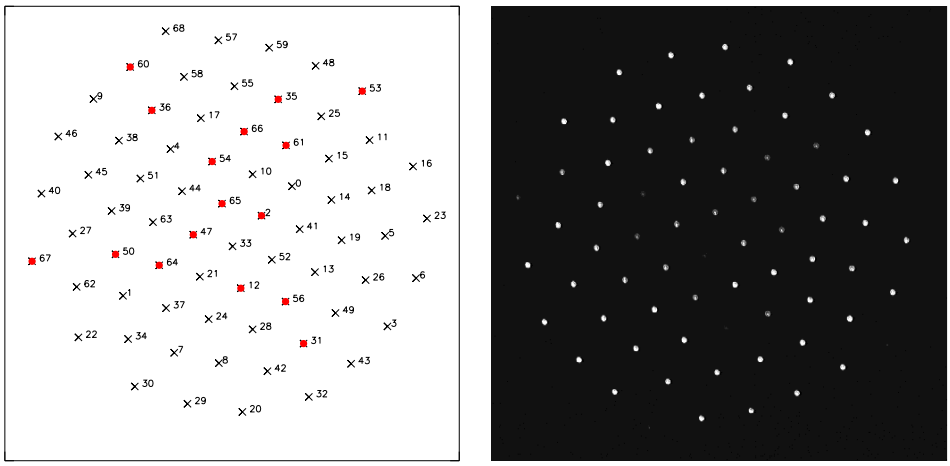

Figure 4.8: Right: Image of the crystal in the test experiment, Left: Particle positions in that frame. Marked on the left side are particles with local maxima in the distribution of the frame to frame displacement

to not measure only the error.

4.4.1 Basic Quantities

The quantities of interest which should be resolvable are the maximum deviation of a particle from its mean lattice site and its displacement from one frame to the next in dependence on the experimental parameters. These two values are crucial for the validity of a measurement. If they are in the range of or even smaller than the error δx, one will get just the error distribution as a result.
Assume a particle is located in a screened coulomb potential well generated by two surrounding particles with the same charge, but no interactions or energy transfer are allowed. Also friction is neglected, but the particle gets a constant temperature T.
We will use $r = \sqrt{(x - x_{ml})^2 + (y - y_{ml})^2}$ as the particle coordinate with respect to its mean lattice site (x_{ml}, y_{ml}) in the 2-dimensional crystal, assuming radial symmetry inside the nearest neighbor cage. The error δr of r is the same as δx:

$$\delta r^2 = \left(\frac{x - x_{ml}}{r}\right)^2 \delta x^2 + \left(\frac{y - y_{ml}}{r}\right)^2 \delta x^2 = \delta x^2$$

as follows from equation (4.4), but the number of degrees of freedom is reduced to 1 in this consideration. Further the approximation of a linear chain of particles is used as it is shown in the sketch 4.9.
According to the equipartition theorem [21], each degree of freedom of a system at temperature T has an average kinetic energy

$$E_{kin} = \frac{1}{2} k_B T \tag{4.12}$$

The potential well is given by the interparticle potential $\Phi_{IP}(\tilde{r})$ at a distance $\tilde{r}$ between two particles

$$\Phi_{IP}(\tilde{r}) = \frac{Q_P}{4\pi\epsilon_0(\tilde{r})} e^{-\frac{\tilde{r}}{\lambda_D}} \tag{4.13}$$

where Δ is the interparticle distance (distance between two lattice sites). It determines the potential energy $E_{pot}(\tilde{r}) = Q_P \cdot \Phi_{IP}(\tilde{r})$. Note that Φ_{IP} is defined for the distance between two charges, not for the distance to the mean lattice site. At (x_{ml}, y_{ml}) lies the minimum potential $\Phi_{IP}(\Delta)$ (figure 4.9), with the interparticle distance Δ.

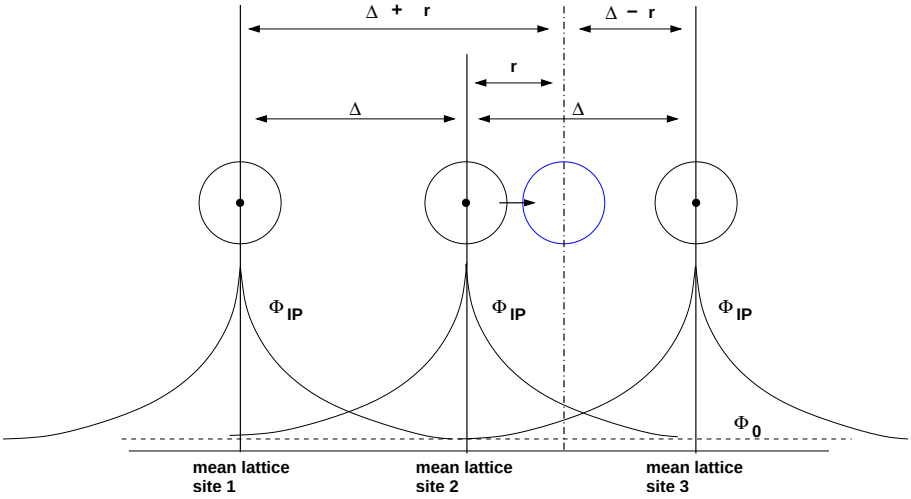

Figure 4.9: Linear chain of three particles.

The question is now with respect to experimental parameters,

1. How large is the average displacement $\langle \Delta r \rangle$ from one frame to the next?
2. What is the maximum deviation r_{max} a particle can move away from its mean lattice site?

4.4.2 Dependence of Thermal Motion

$\langle \Delta r \rangle$ should be dominated by thermal motion as long as the time steps Δt is small. Further a Maxwellian velocity distribution is assumed for the particles velocity v in one dimension:

$$F_{M1}(v) = \frac{1}{\sqrt{2\pi}\sigma_v} e^{-\frac{v^2}{2\sigma v}} \tag{4.14}$$

where σ_v is the standard deviation of the velocity v. $F_{M1}(v)$ is independent of the position r of the particle (see chapter 5.4.1). The particle can thus has a mean thermal velocity

$$\langle v \rangle = \sqrt{\frac{2k_B T}{M_P \pi}} \tag{4.15}$$

with M_P is the particle mass. This defines the average frame to frame displacement

$$\langle \Delta r \rangle = \langle v \rangle \Delta t \tag{4.16}$$

where Δt is the frame rate of the camera. Required is now

$$\langle \Delta r \rangle \gg \delta r = \delta x = 0.9 \mu \mathrm{m}/m \tag{4.17}$$

with the magnification m. The value for δr is taken from the error estimation in chapter 4.3.3. With equations (4.15) and (4.16) inserted equation (4.17) yields

$$\Delta t \sqrt{\frac{2k_B T}{M_P \pi}} \gg \frac{0.9\mu/\mathrm{m}}{m} \Rightarrow m \gg \frac{0.9\mu/\mathrm{m}}{\Delta t} \sqrt{\frac{M_P \pi}{2k_B T}} \tag{4.18}$$

The temperature and pixel-noise thus give a limit on the magnification to use.

A quantitative estimation is done in figure 4.10 for $\Delta t = 1/29$ s and $M_P = 5.5 \cdot 10^{-13}$ kg. The values correspond to the experiments done. The kinetic energy $k_B T$ is varied between 0 to 0.085 eV ($\hat{=}$ 0 to 990 K). The figures show the dependence of $\langle \Delta r \rangle$ on $k_B T$ (right panel), and the magnification versus $k_B T$ (left panel) for equality taken in equation (4.18). The plots must be interpreted as follows:
The magnification one has to choose to get a $\langle \Delta r \rangle$ for a given temperature, which exceeds the pixel-noise by far, must be much higher than the curve in 4.10 a).
Figure 4.10 b) shows the $\langle \Delta r \rangle$ which can be expected for different temperatures.

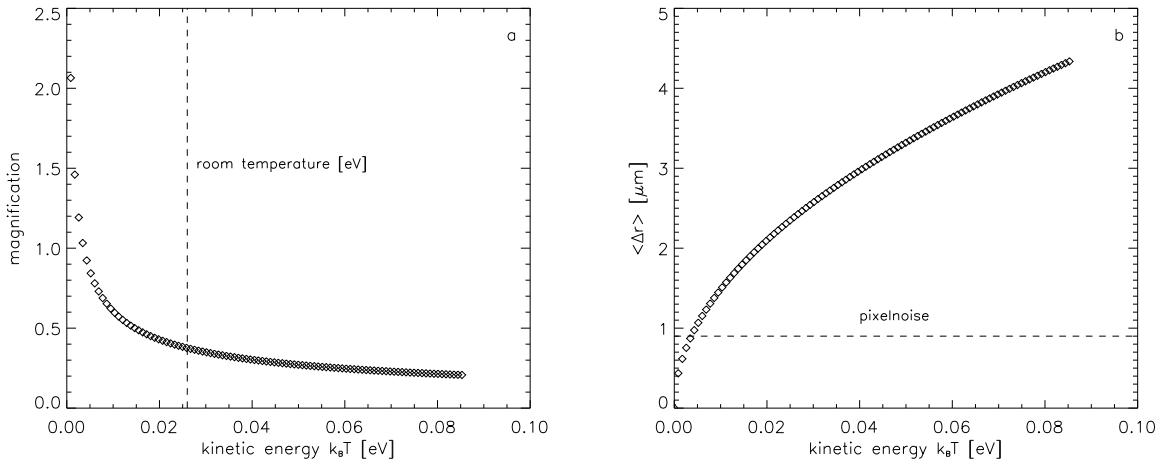

Figure 4.10: a) Magnification m vs. kinetic energy $k_B T$, b) $\langle \Delta r \rangle$ vs. kinetic energy $k_B T$ and pixel-noise for $m = 1$

4.4.3 Dependence of the Maximum Displacement

In section 2.2 the Coulomb coupling parameter Γ was introduced. If Γ is known, it defines the relation of mean kinetic energy to mean potential energy. This relation can be used to estimate the average deviation $\langle r \rangle$ of the particle from the mean lattice site.
The mean potential energy is given by the potential at the interparticle distance:

$$\langle E_{pot} \rangle = Q_P \cdot \Phi_{IP}(\Delta) = \frac{Q_P^2}{4\pi\epsilon_0 \Delta} e^{-\frac{\Delta}{\lambda_D}} \tag{4.19}$$

For a strongly coupled system such as the plasma crystal and one degree of freedom follows for Γ

$$\begin{aligned} \Gamma = \frac{2Q_P^2 e^{-\frac{\Delta}{\lambda_D}}}{4\pi\epsilon_0 \Delta k_B T} &\gg 1 \\ \frac{Q_P^2}{4\pi\epsilon_0 \Delta} e^{-\frac{\Delta}{\lambda_D}} &\gg \frac{k_B T}{2} \end{aligned} \tag{4.20}$$

This applies to the average energies. Nevertheless the particle can move up the potential well as long as its thermal energy exceeds the change of E_{pot} during this step, since equation (4.20 is valid for the averaged energies only:

$$\frac{1}{2} k_B T \geq \Delta E_{pot} \tag{4.21}$$

When equality holds, r_{max} is reached. Now an expression for ΔE_{pot} has to be found. In the model with a chain of three particles the base potential Φ_0 is given by the potential at the mean lattice site produced by both neighbors:

$$\Phi_0 = 2 \cdot \Phi_{IP}(\Delta) \tag{4.22}$$

$$\Rightarrow E_{pot,0} = Q_P \Phi_0 \tag{4.23}$$

The potential energy at a place r is

$$E_{pot}(r) = Q_P \Phi_{IP}(\Delta + r) + \Phi_{IP}(\Delta - r) \tag{4.24}$$

For small deviations r the change of the potential energy can be written as

$$\begin{aligned} \Delta E_{pot} &= E_{pot}(r) - E_{pot,0} \\ &= Q_P \left(\Phi_{IP}(\Delta + r) + \Phi_{IP}(\Delta - r) - 2 \cdot \Phi(\Delta) \right) \geq \frac{1}{2} k_B T \end{aligned} \tag{4.25}$$

In this consideration the equality holds for the maximum distance r_{max} the particle can move away from the mean lattice site. To get a handy expression for r_{max} some simplifications have to be made. First, $\Phi_{IP}(\Delta + r) + \Phi(\Delta - r)$ is expanded in a Taylor series around

$r = 0$. This consideration is valid for small deviations r. It will lead to an underestimation of r_{max}. But the purpose of finding the parameter range will be fulfilled sufficiently:

$$\begin{aligned}
\Phi_{IP}(\Delta + r) + \Phi_{IP}(\Delta - r) &= \\
= \Phi_{IP}(\Delta) + \frac{\partial \Phi_{IP}}{\partial r}|_{r=0} \cdot r &+ \frac{1}{2}\frac{\partial^2 \Phi_{IP}}{\partial r^2}|_{r=0} \cdot r^2 + \\
+\Phi_{IP}(\Delta) - \frac{\partial \Phi_{IP}}{\partial r}|_{r=0} \cdot r &+ \frac{1}{2}\frac{\partial^2 \Phi_{IP}}{\partial r^2}|_{r=0} \cdot r^2 + O(r^3) \approx \\
&\approx 2 \cdot \Phi_{IP}(\Delta) + \frac{\partial^2 \Phi_{IP}}{\partial r^2}|_{r=0} \cdot r^2
\end{aligned} \tag{4.26}$$

The linear term cancels out due to the symmetry of the model. The second derivative at the position $r = 0$ is given by

$$\frac{\partial^2 \Phi_{IP}}{\partial r^2}|_{r=0} = \Phi_{IP}(\Delta) \left(\left(\frac{\Delta + \lambda_D}{\Delta \lambda_D} \right)^2 + \frac{1}{\Delta^2} \right) \tag{4.27}$$

For ΔE_{pot} and equality in equation (4.25) follows

$$\begin{aligned}
\Delta E_{pot} &= 2 \cdot Q_P \Phi_{IP}(\Delta) + Q_P \Phi_{IP}(\Delta) \left(\left(\frac{\Delta + \lambda_D}{\Delta \lambda_D} \right)^2 + \frac{1}{\Delta^2} \right) \cdot r_{max}^2 \\
&\quad -2 \cdot Q_P \Phi_{IP}(\Delta) \\
&= Q_P \Phi_{IP}(\Delta) \left(\left(\frac{\Delta + \lambda_D}{\Delta \lambda_D} \right)^2 + \frac{1}{\Delta^2} \right) \cdot r_{max}^2 \qquad (4.28) \\
&= \frac{1}{2} k_B T \qquad (4.29)
\end{aligned}$$

Solved for r_{max} and with $\kappa = \Delta / \lambda_D$ and the definition of Γ we get:

$$\begin{aligned}
r_{max} &= \sqrt{\frac{k_B T}{2 Q_P \Phi_{IP}(\Delta)}} \sqrt{\frac{\Delta^2 \lambda_D^2}{\Delta^2 + 2\lambda_D \Delta + 2\lambda_D^2}} \\
&= \sqrt{\frac{\Delta^2}{\Gamma}} \sqrt{\frac{1}{2 + 2\kappa + \kappa^2}}
\end{aligned} \tag{4.30}$$

Here also $r_{max} \gg \delta r$ should be fulfilled.

Now the difficult part starts: correct starting values for the parameters have to be chosen, and their dependencies on real experimental parameters like pressure and RF power have to be found. These were taken mainly from [10]. The assumption is a linear dependence of λ_D and Γ of pressure and peak-to-peak voltage and a connection between the mean interparticle spacing and λ_D.

Dependencies

1. $\Delta \approx 2\lambda_D \Rightarrow \kappa = 2$

2. $n_e \propto pU_{pp}$: The electron density is proportional to the neutral gas pressure p times RF peak-to-peak voltage U_{pp}. It follows for λ_D and Δ:

$$\lambda_D = \sqrt{\frac{\epsilon_0 k_B T}{q_e^2 n_e}} = \lambda_{D0}\sqrt{\frac{n_{e0}}{n_e}} = \lambda_{D0} \cdot \sqrt{\frac{p_0 U_{pp,0}}{p_1 U_{pp,1}}} \tag{4.31}$$

$$\Delta = 2\lambda_D = 2\lambda_{D0} \cdot \sqrt{\frac{p_0 U_{pp,0}}{p_1 U_{pp,1}}} = \Delta_0 \cdot \sqrt{\frac{p_0 U_{pp,0}}{p_1 U_{pp,1}}} \tag{4.32}$$

3. With 1. and 2. follows for Γ:

$$\Gamma \approx \frac{2 \cdot Q_P^2 e^{-2}}{4\pi\epsilon_0 2\lambda_D k_B T} = \frac{2 \cdot Q_P^2 e^{-2}}{4\pi\epsilon_0 2\lambda_{D0} k_B T}\sqrt{\frac{p_1 U_{pp,1}}{p_0 U_{pp,0}}} = \Gamma_0 \cdot \sqrt{\frac{p_1 U_{pp,1}}{p_0 U_{pp,0}}} \tag{4.33}$$

   The charge could be approximated by the particle radius, but this relation is not used here.

With that we get for r_{max}:

$$r_{max} = \frac{\Delta}{\sqrt{\Gamma}}\frac{1}{\sqrt{10}} = \frac{2\lambda_{D0}}{\sqrt{10\Gamma_0}}\left(\frac{p_0 U_{pp,0}}{p_1 U_{pp,1}}\right)^{3/4} \tag{4.34}$$

Required is

$$r_{max} \gg \delta r = 0.9\mu\mathrm{m}/m \tag{4.35}$$

To increase the quality of statistics the number of particles N_P in the field of view should be as large as possible. It is connected to Δ as follows:

The area of the field of view as seen by the camera is A = A'$/m^2$ (A': chip size).
Each particle in a hexagonal crystal structure has an area of

$$\mathrm{A}_P = \frac{1}{2} \cdot n \cdot 2 \cdot a \cdot \tan(\frac{\alpha}{2}) = 6 \cdot (\frac{\Delta}{2})^2 \tan 30° = 0.87 \cdot \Delta^2 \tag{4.36}$$

for $n = 6$: number of edges, $a = \frac{\Delta}{2}$, $\alpha = 30°$.
For N_P particles in the field of view follows:

$$\mathrm{A} = \frac{\mathrm{A'}}{m^2} = N_P \cdot \mathrm{A}_P = N_P \cdot 0.87 \cdot \Delta^2 \tag{4.37}$$

$$\Rightarrow N_P = \frac{\mathrm{A'}}{m^2 0.87 \Delta_0^2}\frac{p_1 U_{pp,1}}{p_0 U_{pp,0}} \tag{4.38}$$

For given p_1, $U_{pp,1}$ the numbers of particles can be derived.

Estimation of starting values The following values except the last were taken from [10] as starting values:

- $p_0 = 2.7$ Pa
- $U_{pp,0} = 60$ V
- $\lambda_{D0} = 0.85 \cdot 10^{-3}$ m $\rightarrow \Delta = 1.7 \cdot 10^{-3}$ m
- $Q_0 = 17 \cdot 10^3$ q_e
- $k_B T = 0.026$ eV ($\hat{=}$300 K)
- A'$= 1024 \cdot 1024 \cdot 9 \cdot 10^{-12}$ m^2 $= 8.49 \cdot 10^{-5}$ m^2

$\Rightarrow \Gamma_0 = 8550$
With the above starting values equation (4.34) is evaluated graphically in figure 4.11 for a wide range of $p_1 U_{pp,1}$. The pressure ranges from 1 to 5.9 Pa, $U_{pp,1}$ from 40 to 140 V. The plot shows r_{max} versus $U_{pp,1}$ while the colors indicate the change of p_1. For comparison, the location of the pixel-noise for the magnifications $m = 1$, $m = 1.5$ is included. N_P is calculated for the same ranges and $m = 1, m = 1.5$. It is presented in the plot 4.12 versus $U_{pp,1}$.

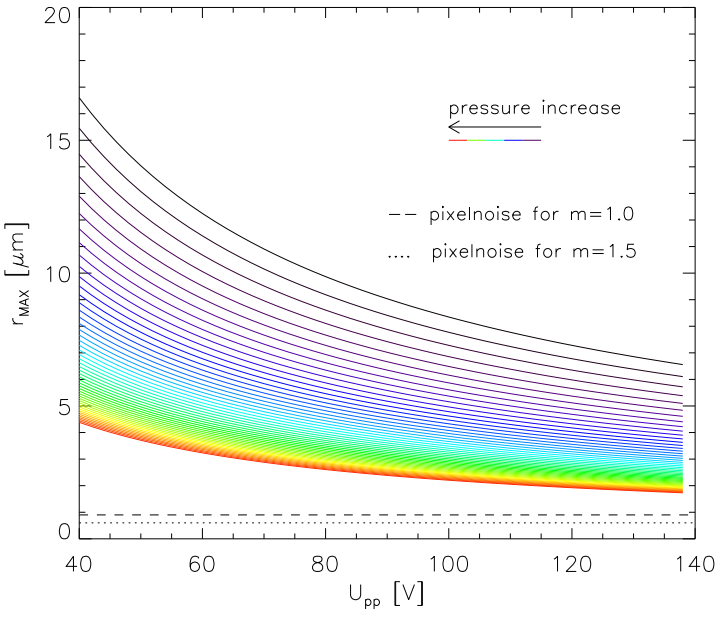

Figure 4.11: Maximum distance from mean lattice site vs. $U_{pp,1}$. The colors indicate different pressures from 1.0 Pa to 5.9 Pa.

Summary of Parameter Estimation As follows from figure 4.10 a) the magnifications choosen for data recording should be much larger than $m = 0.4$ to exceed the measurement error if room temperature is assumed. This is not a problem, since usually at least $m = 1$ is choosen. Further $\langle \Delta r \rangle$ is nearly almost higher than the expected pixel-noise.

r_{max} seems not to be strongly dependent on both $U_{pp,1}$ and p_1. The change between the extrema for $\Delta U_{pp,1} = 100$ V and $\Delta p_1 = 4.9$ Pa is just 2 μm. But still δr is exceeded by far, which was the required condition.
The number of particles in the field of view shows a stronger dependence on $U_{pp,1}$ and p_1. To reach $N_P \geq 100$, a peak-to-peak voltage > 100 V and a pressure > 4 Pa should be choosen for a low magnification of $m = 1$, whereas at higher magnifications in the range of 1.5 a high N_P is difficult to reach. Since the lower resolutions does not break condition (4.35), it should be concluded in favour of higher N_P to take the low magnification for experiments. What also has to be considered for the parameter settings is that too low pressure and voltage will lead to melting of the crystal, since Γ decreases with $\sqrt{p \cdot U}$. Another restriction is the plasma itself. At low gas densities the plasma destabilizes due to lack of ionized atoms while at low voltages there is not enough power to ionize the gas. From observations in test runs follows a minimum pressure of 1 Pa, and a minimum power at the RF generator of $1 - 2$ W (this sets also the voltage at the electrode).
N_P is restricted to the upper limit by the fact, that due to the radial confinement, particles will arrange in a 3-dimensional crystal, if N_P is too high. It showed up that for obtaining a single layer of particles, $N_P \approx 200$ is a realistic value for the particle sizes used and $m \approx 1$.

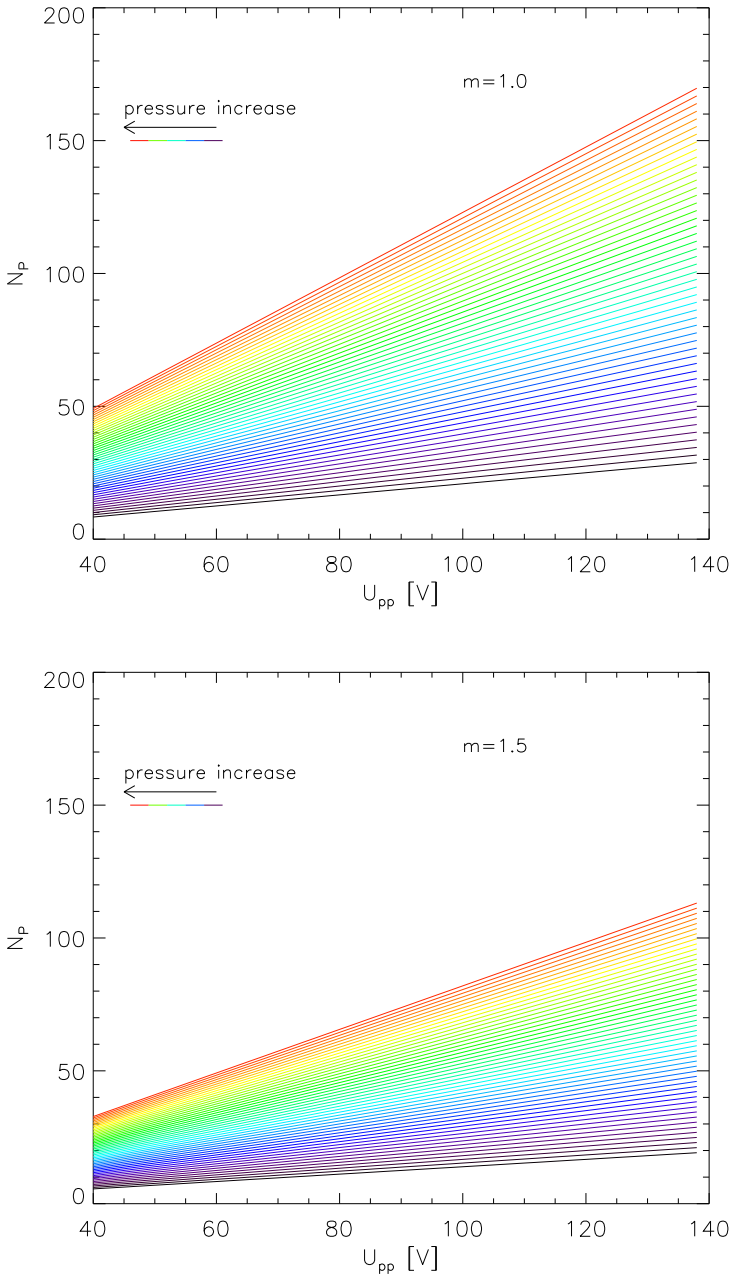

Figure 4.12: N_P vs. $U_{pp,1}$ for two magnifications $m = 1.0$ (top) and $m = 1.5$ (bottom). The colors indicate different pressures from 1.0 Pa to 5.9 Pa.

Chapter 5

Analysis

The analysis of the data sets consists of different steps, starting with the dynamical properties of the macroscopic crystal as a whole, down to the single particles as systems in themselves. The aim is to prepare and investigate the data in order to make it possible to give a statement about ergodic behaviour of particles in the plasma crystal with respect to the condition of a stationary system and with the restriction of strongly coupled components of the ensemble.

In section 5.1 the specifications of the performed experiments are given. A first rough analysis of the data with regard to relevant length and time scales of the system is done, based primarily on the experimental settings.

Section 5.2 treats the plasma crystal as a macroscopic system which acts on external influences. This behaviour can be identified in section 5.2.1 as different trends in the time series of averaged spatial coordinates and velocities. The time series are then decomposed into the motions common to all particles and the intrinsic dynamics of the single particles. This is done by the removal of trends in section 5.2.2.

After common trends are removed from the data, the dynamical behaviour of the single particles is the subject of interest. The particle motion is described by the time series of the displacement of a particle from its mean lattice site and by its velocity. First the particular time series of each particle is tested for stationarity as an preliminary condition of ergodic behaviour in section 5.3. Then the distribution functions describing the dynamics of the particles will be investigated in section 5.4.

The last step is a test for ergodic behaviour of the particles in section 5.5 with regard to their displacements and velocities. The test is carried out with usual statistical methods.

5.1 Performed Experiments

A 2-dimensional plasma crystal with a hexagonal structure was generated and used for analysis. No particles were located above or below of the layer. Attention is payed to the fact, that a large number of particles is needed for good statistics with regard to the ensemble. Long-time measurements were recorded to further improve the statistics by obtaining long time series of particle coordinates. In section 5.1.1 the detailed experimental setup and settings for this experiment are described. After that the expected typical length and time scales are estimated from the measured data and experimental settings in section 5.1.2. A comparison of two magnification settings is done in section 5.1.3. The results of this chapter are finally summarized in section 5.1.4.

5.1.1 Specifications

Starting from the basic setup described in chapter 4.1, the details for the data acquisition used for analysis are given here. Table 5.1 gives an overview of the experimental parameters.

Power and Pressure In our experiments we used an Argon discharge. The gas flow into the chamber was reduced to a low rate of 0.5 sccm. The valve for pressure control was set fixed to keep the pressure constant at 4.25 Pa. No gas flow and a closed valve would be best to decrease the influences on the crystal, but then the plasma quality due to enhanced gas impurities. The radio frequency at the lower electrode was at 13.56 MHz. Six measurements have been made for three different peak-to-peak voltages and two magnifications. Since the RF generator supplies an unstable voltage for low powers in the range of 1 W, an additional damping device with a damping of 6 dB was connected between RF generator and matching unit. The generator can thus be operated at higher powers without increasing U_{pp}. Unfortunately the result was not as well as hoped. Still power fluctuations appeared that affected the plasma crystal.
Self bias voltage U_{SB} and effective RF peak-to-peak (pp) voltage $\tilde{U}_{pp}$ and current $\tilde{I}_{pp}$ were read from the oscilloscope with an accuracy of ≈ 5 %. The measured values are damped by the electronics by a factor $D = 46.3$ dB (power damping). $\tilde{I}_{pp}$ is displayed as a voltage $\tilde{U}_{I,pp} = \tilde{I}_{pp} \cdot 1\ \mathrm{M\Omega}$. The voltage and current values applied to the electrode are calculated by using the relation for power damping:

$$P_{in} = P_{out} \cdot 10^{D/10dB} \tag{5.1}$$

for input and power P_{in}, P_{out} respectively. With $P \sim U^2$ and $P \sim I^2$ follows:

$$\Rightarrow U_{pp} = \left(\tilde{U}_{pp}\right) \cdot 10^{D/20dB} \tag{5.2}$$

$$I_{pp} = \left(\frac{1}{1\mathrm{M\Omega}}\tilde{U}_{I,pp}\right) \cdot 10^{D/20dB} \tag{5.3}$$

Particles and Illumination The particles were Formaldehyde-Melamine monospheres with a diameter of 8.9 ± 0.1 μm and a mass of $5.5 \cdot 10^{-13}$ kg. They are relatively large particles and are expected to aquire a charge $\approx$ 13000 q_e (see chapter 2.2). The radial confinement was contrived by the metal cap on the lower electrode described in chapter 4.1. The laser was set to 213 mW. The maximum of 500 mW was not used, because the laser sheet can trap the particles or push them if the power is too high, thus influencing the motion.

Camera Images have been taken at two magnifications for each voltage setting to test whether the effect of the pixel-noise, which becomes smaller at higher magnifications, makes any difference in the analysis. The camera was set to a frame rate of 29 frames per second (fps) and a exposure time of 30 ms. At each run 10000 images have been taken, of which 9999 could be used for analysis ($\hat{=}$ 345 s). The first image has to be rejected because it has a large time difference to the next due to the initialisation of the frame grabber.
A lens with a fixed focal distance of 200 mm was used. To increase the maximum magnification, spacer rings where inserted between lens and camera. These increase the distance between lens and CCD-chip. Thus the camera can be moved closer to the object but still can be zoomed in.

The magnification had been obtained by taking images of a defined scale with exactly the same camera and lens setting as used for the recording of images during the experiments.

Table 5.1 lists the specifications of the experiment. Numbers are given to the different measurements, and these will be referred to later. For experiments Ia,IIa,IIIa spacer rings with 8 and 27.5 mm length were used, for the others a third ring with 14 mm was added.

Experiment Number	Ia	Ib	IIa	IIb	IIIa	IIIb
self bias [V]	-27.7	-28.0	-33.0	-34.2	-37.5	-36.8
voltage (pp) [V]	121	122	142	146	155	153
current (pp) [μA]	357	359	405	421	442	442
forward power at RF generator [W]	37	30	47	42	60	47
pressure [Pa]	4.25	4.28	4.25	4.28	4.25	4.29
magnification	0.992	1.494	0.992	1.494	0.992	1.494
resolution [mm/pixel]	0.0091	0.0060	0.0091	0.0060	0.0091	0.0060

Table 5.1: Experimental settings.

The a-series includes the measurements with low camera resolution. The b-series was recorded at the corresponding higher resolution, but approximately the same power settings as before. What should be noted is that the power supplied by the RF generator is much lower for the b-series, but though yielding nearly the same U_{pp} as the related

a-measurements. It was found out that the problem must be an internal error of the RF generator, the cause of which could not be identified yet. But important for the experiment are the peak-to-peak values as they are in fact applied to the electrode.

5.1.2 Expected Scales

In chapter 4.4 the frame to frame motion $\langle \Delta r \rangle$ and the maximum deviation r_{max} from the mean lattice site were introduced. With pressure and peak-to-peak voltage of the experiment these quantities can be derived as an estimate of the relevant length scales. This is also a test on the validity of the approximations done, since the mean interparticle spacing Δ can be estimated directly from the images and can be compared with the assumption $\Delta \approx 2\lambda_D$ used in the estimation. Also the Einstein-frequency $\omega_E = 2\pi\nu_E$ and the Epstein drag coefficient ν_{Ep} will be calculated since they determine the typical time scales of a plasma crystal experiment.

5.1.2.1 Length Scales

Thermal motion Equation (4.16) with p and U_{pp} from table 5.1, the particle mass $M_P = 5.5 \cdot 10^{-13}$ kg, $\Delta t = 1./29$ s and by assuming room temperature $T = 290$ K yields for $\langle \Delta r \rangle$

$$\Delta r_{th,expected} = \sqrt{\frac{2k_B T}{M_P \pi}} \Delta t = 2.35 \ \mu\text{m} \tag{5.4}$$

for all measurements. Due to effects mentioned in chapter 2.3.3 the particle temperature could be much higher in fact. Later it will be derived from the velocities which are obtained as the difference between consecutive frames divided by the time difference between the frames, Δt. As comparison, the motion pretended by the pixel-noise $\delta r = 0.9\mu\text{m}/m$ would be of the magnitude of

$$\begin{aligned} \delta r &= 0.907 \ \mu\text{m} \quad \text{for } m = 0.992 \\ \delta r &= 0.602 \ \mu\text{m} \quad \text{for } m = 1.494 \end{aligned} \tag{5.5}$$

Even for the low magnification the noise is still smaller by more than a factor of 2. The error in the velocities, $\sqrt{2}\delta r/\Delta t$, is in the range of 37.2 and 24.7 μm/s respectively while $\langle v \rangle = \langle \Delta r \rangle_{th,expected}/\Delta t$ is 68.15 μm.

Maximum deviation The derivation of r_{max} contained other useful quantities as the coupling parameter Γ or the screening length λ_D which are treated here, too. With equation (4.34) the expected maximum deviation from the mean lattice site is derived. To estimate λ_D as 1/2 times the interparticle distance, for each frame Δ is derived as $\sqrt{\frac{A}{0.87 N_P}}$ with the image size A and the number of particles in the field of view N_P under the assumption of a hexagonal lattice (see equation (4.37)). Then the average Δ of all frames

is determined with the standard deviation taken as the error.
Two values for λ_D have been calculated: $\lambda_{D,exp} = \Delta/2$, as it was assumed in the parameter estimation in section 4.4.3, and $\lambda_{D,est} = \lambda_{D0} \cdot \sqrt{p_0 U_0 / p_1 U_1}$ (equation (4.31)) with $p_0 = 2.7$ Pa and $U_{pp,0} = 60$ V. Also the coupling parameter Γ is derived with equation (4.33) and finally the ratio $\kappa = \Delta/\lambda_{D,est}$ which should be approximately 2 if the assumption $\Delta = 2\lambda_D$ is fulfilled in the plasma crystal. Panel 5.1 shows all quantities in dependence of U_{pp}.

The maximum deviation (upper right image) is in the range of 5 μm and thus sufficiently larger than the error δr. The interparticle distance decreases slowly with increasing U_{pp}, accordingly the same hold for $\lambda_{D,est}$. $\lambda_{D,exp}$ exceeds this value not very far, thus both approximations yield the same results. The coupling is very strong with Γ of the order of $2 \cdot 10^4$ for all measurements and increases with peak-to-peak voltage. κ lies in the range of 2 to 2.1, increasing with U_{pp}.

Experiment Number	Ia	Ib	IIa
N_P	190	110	194
r_{max} [μm]	5.03	5.03	4.91
Δ [μm]	800 ± 10	834 ± 18	783 ± 7
$\lambda_{D,exp}$ [μm]	400 ± 5	391 ± 9	378 ± 4
$\lambda_{D,est}$ [μm]	401	399	370
Γ	19939	20068	21618
Experiment Number	IIb	IIIa	IIIb
N_P	81	197	82
r_{max} [μm]	4.93	4.88	4.88
Δ [μm]	791 ± 13	757 ± 10	753 ± 6
$\lambda_{D,exp}$ [μm]	417 ± 7	395 ± 5	376 ± 3
$\lambda_{D,est}$ [μm]	364	355	355
Γ	21962	22565	22515

Table 5.2: Quantities estimated from the data. N_P: number of particles in the field of view; r_{max}: expected maximum deviation from mean lattice site; Δ: mean interparticle spacing; $\lambda_{D,exp} = 2\Delta$: screening length; $\lambda_{D,est}$: screening length estimated with equation (4.31); Γ: coupling parameter (equation (4.33))

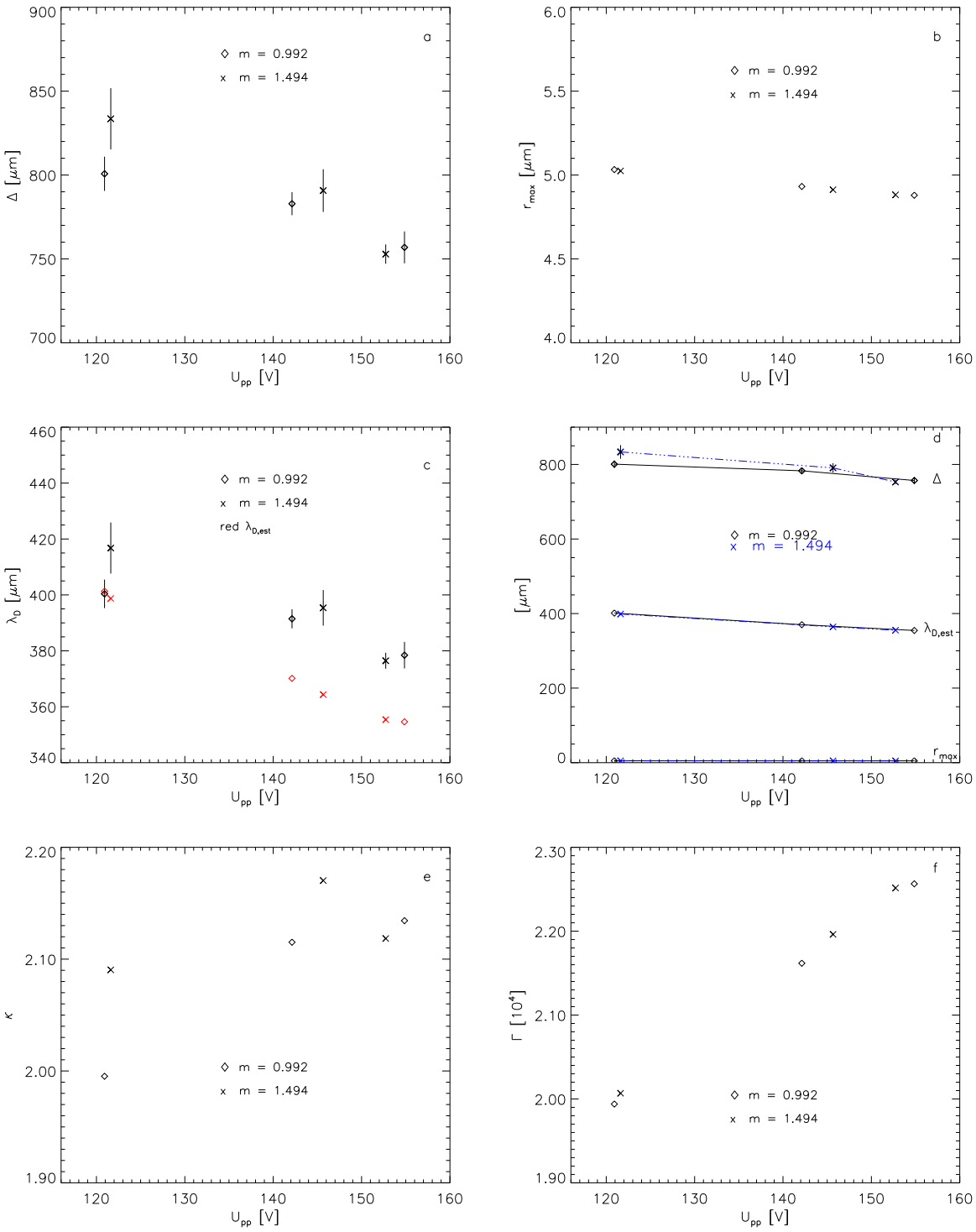

Figure 5.1: Plotted versus U_{pp} are a) Mean interparticle spacing Δ, b) r_{max}, c) $\lambda_{D,exp}$ (black) and $\lambda_{D,est}$ (red), d) Comparison of the magnitudes of Δ, λ_D and r_{max}, e) $\kappa = \Delta/\lambda_{D,est}$, f) Γ.

5.1.2.2 Time Scales

Einstein frequency The Einstein frequency can be estimated by the approximation of a linear chain of particles as introduced in chapter 4.4. In this consideration the restoring force acting on a particle for a small deviation r from its mean lattice site can be written as

$$F_R = -\text{grad}(\Delta E_{pot)} = -k \cdot r \tag{5.6}$$

with the spring constant k and the potential energy ΔE_{pot}. Using the expression for ΔE_{pot} as it was approximated in equation (4.28) and the relation $\omega_E^2 = k/M_P$ it follows

$$F_R = -\text{grad}\left[Q_P \Phi_{IP}(\Delta)\left(\left[\frac{\Delta + \lambda_D}{\Delta \lambda_D}\right]^2 + \frac{1}{\Delta^2}\right) \cdot r^2\right] = -k \cdot r \tag{5.7}$$

$$\begin{aligned} \Rightarrow k &= 2 \cdot (Q_P \Phi_{IP}(\Delta)\left(\frac{\Delta^2 + 2\lambda_D \Delta + 2\lambda_D^2}{\Delta^2 \lambda_D^2}\right) \\ &= 2 \cdot \left(\frac{Q_P^2}{4\pi\epsilon_0 \Delta^3} e^{-\kappa}(2 + 2\kappa + 2\kappa^2)\right) \end{aligned} \tag{5.8}$$

where $\kappa = \Delta/\lambda_D$. Therefore ω_E is given by

$$\omega_E = \sqrt{\frac{1}{M_P} \cdot 2(2 + 2\kappa + \kappa^2)\frac{Q_P^2}{4\pi\epsilon_0 \Delta^3} e^{-\kappa}} \tag{5.9}$$

It will be used here to estimate the frequency of oscillations of a particle in its nearest neighbor potential well. M_P is given by the experiment as $5.5 \cdot 10^{-13}$ kg, $\kappa = \Delta/\lambda_D = 2$ will be used since it. Since the charge is not known exactly, in figure 5.2 $\nu_E = \omega_E/2\pi$ is shown for an interval of charges in the range of $1 - 2 \cdot 10^4 q_e$. ν_E is the frequency in Hz, while ω_E is the circular frequency given in rad/s.

ν_E ranges from 2 to 5 Hz for different charges and interparticle distances. This yields for the time scale τ_E:

$$\tau_E = \frac{1}{\nu_E} = \frac{2\pi}{\omega_E} = 0.2, .., 0.5 \text{ s} \tag{5.10}$$

Epstein frequency The Epstein frequency is the frequency of collisions of dust particles with the neutral gas atoms, i.e. it determines the damping rate, and was given by equation (2.12):

$$\nu_{Ep} = \delta \sqrt{\frac{8 m_g}{\pi k_B T_g}} \frac{p}{\rho_P R_P} \tag{5.11}$$

With the mass of the argon gas atoms $m_g = 39.948$ u $= 66.34 \cdot 10^{-27}$ kg, temperature of the neutral gas $T_g = 290$ K, neutral gas pressure $p = 4.25$ Pa, material density of the

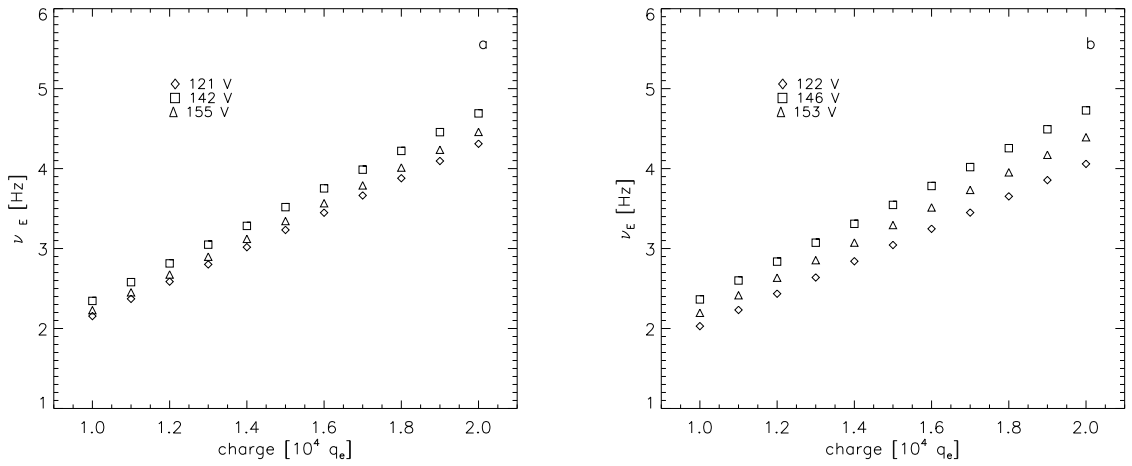

Figure 5.2: ν_E in dependence of the particle charge for $\kappa = 2$ and Δ from table 5.2. a) low resolution, b) high resolution

dust particles $\rho_P = 1490$ kg m^{-3}, particle radius $R_P = 4.45 \cdot 10^{-6}$ m and, as mentioned in chapter 2.3.5, $\delta = 1.44$ follows for ν_{Ep}:

$$\nu_{Ep} = 5.997\text{Hz} \tag{5.12}$$

The timescale τ_{Ep} is therefore:

$$\tau_{Ep} = 1/\nu_{Ep} = 0.167 \text{ s} \tag{5.13}$$

Both time scales are very short compared with the measurement time of nearly 6 minutes and reasonable far from the time resolution of the camera of $1/29 = 0.034$ s.

5.1.3 Comparison of Different Magnifications

One series of measurements had been taken at a higher magnification but the same pressure and voltage settings as the other series. Since the number of particles in the field of view is rather small at high magnifications, the statistical investigations will suffer. In the last section it has been found that length and time scales derived on the basis of the interparticle distance taken out of the measurements coincide. Here the velocities, namely the absolute velocities, will be compared among each other for the corresponding voltage. The aim is to investigate how much the error δx in the coordinates, caused by pixel-noise, influences the measurements at low magnifications. Though from the parameter estimation in chapter 4.4 one would expect a small error in x and y even for magnifications of 1, this might be different for the velocity, since the error $\delta v = \sqrt{2}\delta x/\Delta t$ is higher by a factor of $\sqrt{2}$.

If the error has large effects on the velocity distributions at low magnification, one would detect a difference in the the mean value $\overline{v}$ between high and low magnification, since the error would shift $\overline{v}$ to lower values. Since the error is the same in every frame for every particle, $\overline{v}$ is calculated as the mean over all particles N_P and frames N_f:

$$\overline{v} = \frac{1}{N_P}\frac{1}{N_f}\sum_{i=1}^{N_P}\sum_{k=1}^{N_f} v_{ik} \tag{5.14}$$

Figure 5.3 shows $\overline{v}$ plotted versus the different voltages and for both magnifications. The value for data set Ia (diamond at 121 V, m=0.992) deviates by 20 % of the corresponding value for Ib (m=1.494). But all values of the data sets with low magnification lie within the error bars of the measurement with corresponding high magnification. For significant influence of the pixel-noise a lower $\overline{v}$ would be expected for the low magnification. Since all values coincide very well within the errors, it can be concluded – not considering any other effects leading to differences between both series – that the pixel-noise does not affect the data sets recorded with low magnification much more than it affects the data sets with $m = 1.494$.

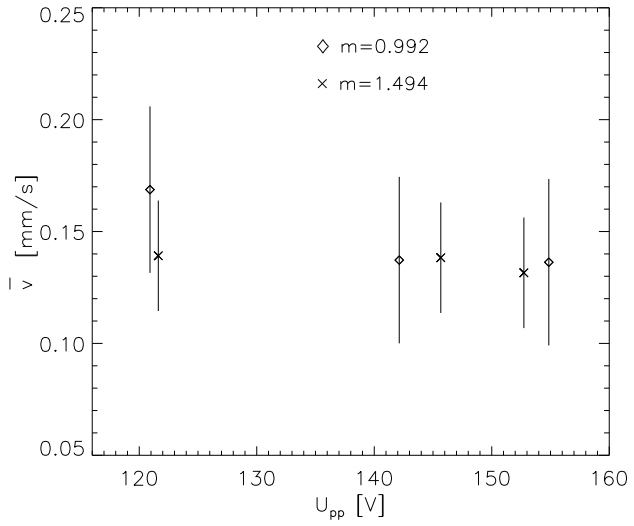

Figure 5.3: Mean absolute velocity $\overline{v}$ vs. U_{pp} as comparison for both magnifications. The error bars include the measurement error.

5.1.4 Summary

In summary, the length scales expected should be resolvable compared to the measurement error, even for the lower magnification, as it was expected from the parameter estimation

done before, since

$$\begin{aligned} \langle \Delta r \rangle &> \delta r \\ r_{max} &\gg \delta r \end{aligned} \tag{5.15}$$

was found.
The time scales of motion are far below the measurement time t_{meas}

$$\tau_E \ll t_{meas} \quad , \quad \tau_{Ep} \ll t_{meas} \tag{5.16}$$

so the condition of long measurement times compared with the relevant dynamical time scales from chapter 3.3.2 is fullfilled.
The system investigated is strongly coupled which might destroy ergodic behaviour since the condition of independent systems is violated.
The measurements at different magnifications reveal the same macroscopic properties as it is expected for experiments with the same parameter settings. Note that the series at different voltages were recorded consecutive for one magnification setting. Then the magnification was changed and the measurements repeated. Though the system did not change during that time with respect to the quantities derived in this chapter. This indicates a stable system in equilibrium with its surroundings, so the condition of a 'closed' system as it was interpreted in chapter 3.3.2 is also fullfilled.

From now on especially the measurements at low magnification are treated, since the smaller measurement error $\delta x = 0.9\mu\text{m}/m$ for $m = 1.494$ had no significant relevance on the quantities derived in this section. The disadvantage of the high magnification is the small number of particles visible in the field of view of the camera, which decreases the validity of the statistics where large numbers of data points for the ensembles are needed.

5.2 Stationarity of the Plasma Crystal

In chapter 3 it was emphasized that stationarity is a necessary condition for ergodic behaviour. Stationarity of a time series $x(t)$ means in general, that for any choosen starting time t_k, the statistical properties of $x(t_k), .., x(t_{k+n})$ do not change in time ($k, n \in N, n > k$). But stationarity is not an overall property visible in all variables of a system. A time series of measurements can be stationary on certain time and length scales, but non-stationarities become visible on others.
Trends are non-stationarities usually happening at much larger time and length scales than the dynamics of the system. In an ensemble of particles, common motions due to external influences can appear. They normally do not affect the dynamics on small scales, but make it difficult to handle quantities like the displacement from the mean lattice site, since they cause a time dependence of the mean lattice site itself and the nature of this dependence is not known in the beginning.

In this chapter averages will be taken over all particles. This is only used to identify common motions of the particles on large scales, which are not subject to the examination of ergodic behaviour. The results of this chapter are to be interpreted only in the sense of detrending, not as a dynamical description of a single particle. Two methods of detecting trends will be discussed in section 5.2.1. The identification of the reasons leading to observed trends and the removing of them from the data will be subject to section 5.2.2.

5.2.1 Detection of Common Trends

Trend analysis is done on the displacements $r(t)$ and the velocities $v(t)$.
The displacement $r_i(t_k)$ of a particle i at a time t_k is defined as the absolute difference $\sqrt{(x_i(t) - x_{ml,i})^2) + (y_i(t) - y_{ml,i})^2}$ of the particle position to its mean lattice site $(x_{ml,i}, y_{ml,i})$, where $x_{ml,i}$ and $y_{ml,i}$ are calculated as the average over the whole time series of coordinates and $k \in [1, N_t]$:

$$x_{ml,i} = \frac{1}{N_t} \sum_{k=1}^{N_t} x_i(t_k) \quad , \quad y_{ml,i} = \frac{1}{N_t} \sum_{k=1}^{N_t} y_i(t_k) \tag{5.17}$$

The velocity components $v_{x,i}(t), v_{y,i}(t)$ of a particle are obtained by the difference of the coordinates between two consecutive frames k, $k+1$ divided by the frame rate. They determine the absolute velocity $v_i(t)$.

$$\begin{aligned} v_{x,i}(t) &= \frac{x_i(t_{k+1}) - x_i(t_k)}{\Delta t} \quad , \quad v_{y,i}(t) = \frac{y_i(t_{k+1}) - y_i(t_k)}{\Delta t} \\ v_i(t) &= \sqrt{v_{x,i}(t)^2 + v_{y,i}(t)^2} \end{aligned} \tag{5.18}$$

5.2.1.1 Running Mean and Standard Deviation

To test a time series for stationarity or trends, a good option is to calculate quantities like mean and standard deviation averaged over sliding windows (consecutive overlapping intervals) in the time domain. Due to averaging, statistical uncertainties have to be taken into account. In a stationary time series, the averaged quantities should not deviate from each other within the errors. Usually values within a confidence interval of $\pm 3\sigma$ around a global mean are accepted as good enough to origin from a stationary time series. σ is here the standard error of the mean over all windows. It was introduced in equation (4.6) as a standard deviation obtained from a theoretical distribution or from a large amount of data points divided by $\sqrt{n}$ where n is the number of points contributing to the global mean.

Running mean $\overline{r}_{i,w}$ and standard deviation $\sigma_{r,i,w}$ are calculated for all N_P particles ($i = 1, ..., N_P, w = 0, ..., N_w - 1$, N_w number of windows) of a data set and for two window sizes L of 300 and 900 frames. The total length of a trajectory is N_t points. Thus we can

write for the mean and its error:

$$\overline{r}_{i,w} = \frac{1}{L}\sum_{j=0}^{L-1} r_i(t_{L\cdot w+j}) \quad , \quad \delta\overline{r}_{i,w} = \sqrt{\delta r^2 + (3\cdot\frac{\sigma_{r,i,w}}{\sqrt{L}})^2} \tag{5.19}$$

and for the standard deviation:

$$\begin{aligned} \sigma_{r,i,w} &= \sqrt{\frac{1}{L-1}\sum_{j=0}^{L-1} |r_i(t_{L\cdot w+j}) - \overline{r}x_{i,w}|^2} \quad , \\ \delta\sigma_{r,i,w} &= \sqrt{\delta r^2 + (3\cdot\frac{\sigma_{r,i,w}}{\sqrt{2(L-1)}})^2} \end{aligned} \tag{5.20}$$

with the measurement error δr and the statistical uncertainty included in the terms for the errors $\delta r_{i,w}$ and $\delta\sigma_{r,i,w}$. δr is equal to the δx estimated in section 4.3.3 as it was shown in section 4.4.1. For the velocities $v_i(t)$ the procedure is the same, while here the measurement error is $\delta v = \sqrt{2}\delta r/\Delta t$.
As an example, figure 5.4 shows the typical development of the running mean and standard deviation for one particle.

To detect trends common to the time series of all particles, averages are taken over all particles for each window w and the error is propagated. Any common motion will add up in the averaged quantities and reveal a significant feature, while random or uncorrelated fluctuations will be smoothed.

$$\hat{r}_w = \frac{1}{N_P}\sum_{i=1}^{N_P} \overline{r}_{i,w} \quad , \quad \delta\hat{r}_w = \sqrt{\sum_{i=1}^{N_P}\left(\frac{\delta\overline{r}_{i,w}}{N_P}\right)^2 + \left(3\cdot\frac{s_{\hat{r}}}{\sqrt{N_P}}\right)^2} \tag{5.21}$$

$$\hat{\sigma}_{r,w} = \frac{1}{N_P}\sum_{i=1}^{N_P} \sigma_{r,i,w} \quad , \quad \delta\hat{\sigma}_{r,w} = \sqrt{\sum_{i=1}^{N_P}\left(\frac{\delta\sigma_{r,i,w}}{N_P}\right)^2 + \left(3\cdot\frac{s_{\hat{\sigma}}}{\sqrt{N_P}}\right)^2} \tag{5.22}$$

$s_{\hat{r}}$ and $s_{\hat{\sigma}}$ are the standard deviations of the $\overline{r}_{i,w}$ respectively $\sigma_{r,i,w}$ for all particles i in one window. The factor 3 is choosen as the confidence limit in the statistical error. In figures 5.5 and 5.6 $\hat{r}_w$, $\sigma_{r,w}$, $\hat{v}_w$ and $\sigma_{v,w}$ are plotted. The global mean for the window size 300 is displayed as a green line together with the confidence interval (dashed green lines).

The displacements show clear deviations in the mean $\hat{r}_w$. Notable is that the fluctuations of the standard deviation $\sigma_{r,w}$ are rather small. This indicates that the nonstationarity detected is not due to a change of the shape of the distribution of r, but more due to a trend which is not connected to the particle dynamics. In contrast, a nonstationarity in the intrinsic dynamics of a system would be expected to change the shape and thus the standard deviation of the distribution describing the system.

Further the running mean seems not to be dependent on the window size, but the standard deviation is. A linear trend could cause this behaviour: By increasing the window size the

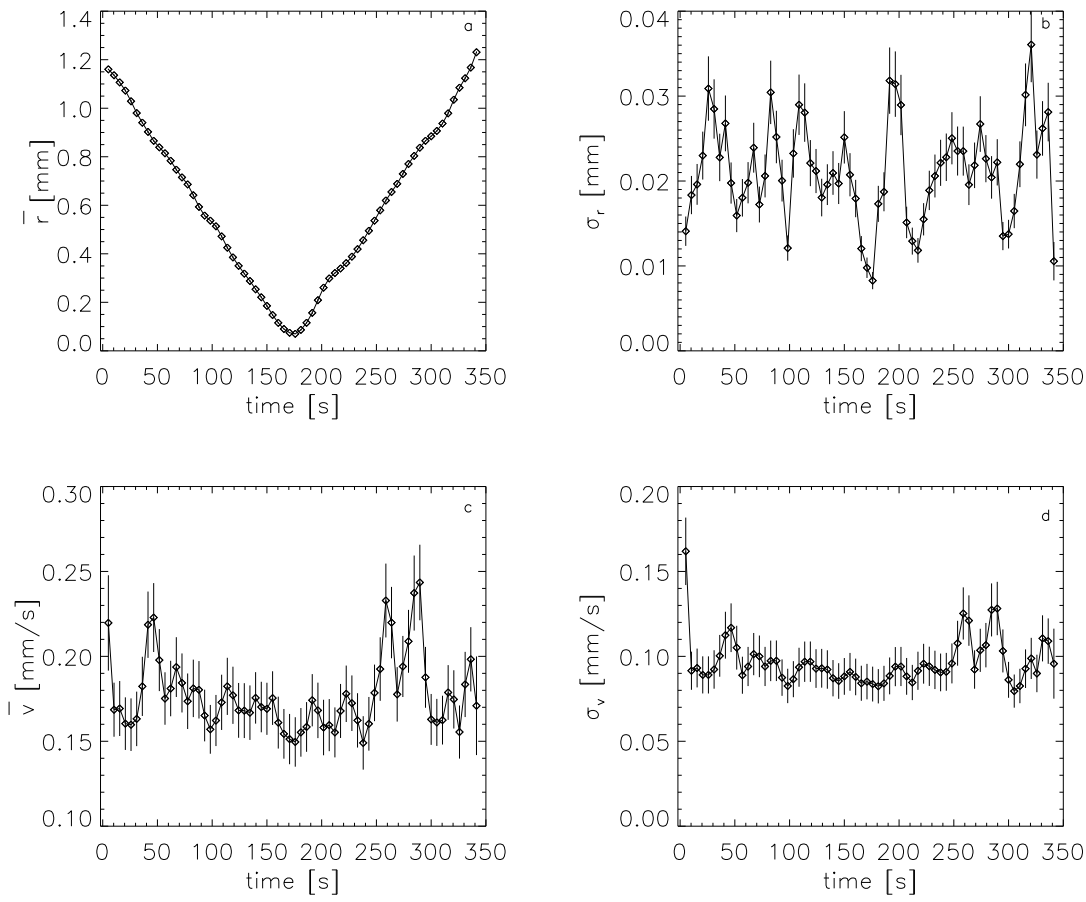

Figure 5.4: Example of the development of running mean and standard deviation for one particle. a) $\overline{r}_{i,w}$, b) $\sigma_{r,i,w}$, c) $\overline{v}_{i,w}$, d) $\sigma_{v,i,w}$. The error bars include the position error δr and δv respectively, and the statistical uncertainty. For $\overline{r}_{i,w}$ the error was too small to be visible.

mean is not affected in this case since the points spread symmetrical around the mean. But the distance of the points to the mean gets larger, thus the standard deviation increases.

The velocities v in figure 5.6 reveal nearly no trend in the averaged quantities, and here the difference between the window sizes is very small for both mean and standard deviation. Except some randomly appearing peaks which are caused by external influences, as will be explained later, common trends are not overwhelming.

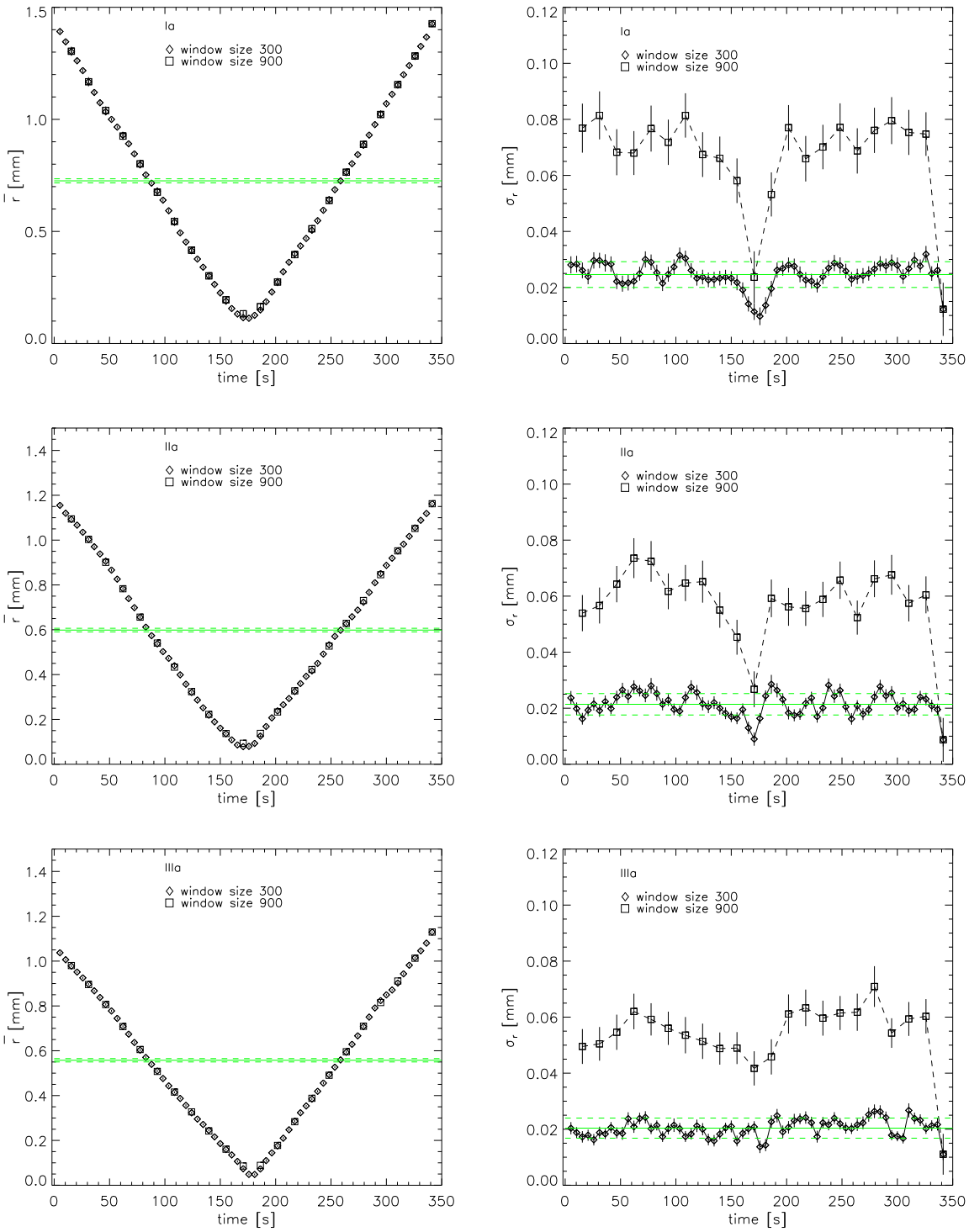

Figure 5.5: Running mean $\hat{r}_w$ (left images) and running standard deviation $\hat{\sigma}_{r,w}$ (right images) for two window sizes. Data sets Ia, IIa, IIIa (low resolution). The error bars where only plotted for $L = 300$, if both data sets where too close.

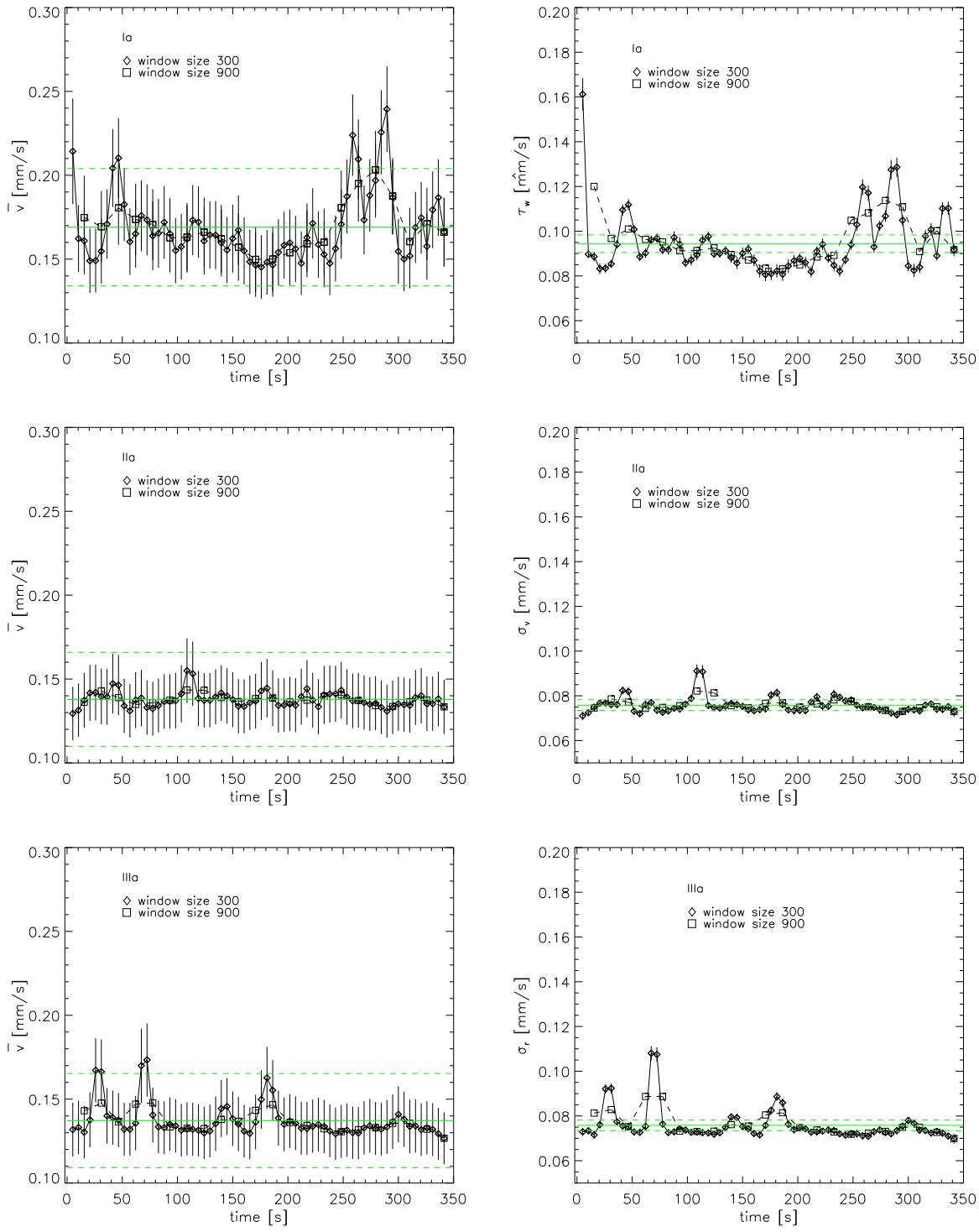

Figure 5.6: Running mean $\hat{v}_w$ (left images) and running standard deviation $\hat{\sigma}_{v,w}$ (right images) for two window sizes. Data sets Ia, IIa, IIIa (low resolution).

Note that for each averaging an error has been derived. From this a quantitative estimation of the deviations from the global mean is obtained. The global mean is given by the average over all windows of the corresponding quantity, e.g. $\hat{r}$ for the displacement. The upper and lower limit are the measurement error propagated into $\hat{r}$ and the statistical error of 3 times the standard error of the mean, as in equation (5.21). It is denoted $\delta\hat{r}$. The deviations are now quantified by calculating the absolute difference between each point $\hat{r}_w$ and the mean over all windows $\hat{r}$. This is done for the window length 300 frames for mean and standard deviation of displacement and velocity. The derived difference should be smaller than $\delta\hat{r}$ for a stationary system. Therefore

$$\Sigma = |\hat{r}_w - \hat{r}| - \delta\hat{r} \leq 0 \qquad \text{assumed for stationary systems} \tag{5.23}$$

The percentage of Σ smaller zero is plotted in figure 5.7 for displacements and velocities of each data set.

The assumption of a trend in the displacements is confirmed by the small percentage of values within the confidence interval, while the velocities are not affected much by that. The small percentage for the standard deviation of the velocity of the measurement at 121 V is very likely caused by the sharp peaks in $\sigma_{v,w}$, not by a shift.

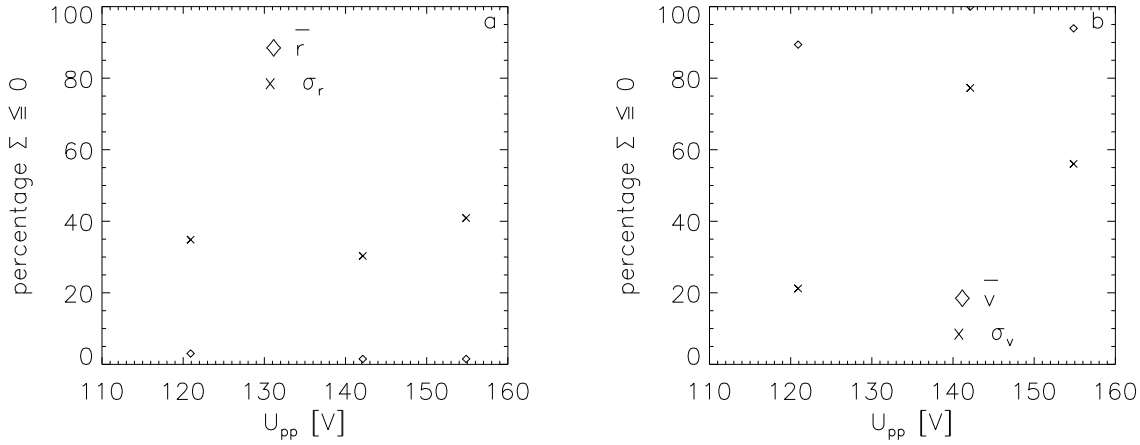

Figure 5.7: Percentage of differences Σ smaller zero for a) running mean and standard deviation of the displacement, b) running mean and standard deviation of the velocities. For stationary systems ≈ 100 % should be smaller zero.

As a second estimator for nonstationary behaviour, the frequencies of the system will be investigated by Fourier analysis methods.

5.2.1.2 Power Spectra

A power spectrum gives information on the frequencies appearing in a system. It is obtained by Fourier transform methods.

Fourier Transform A function $h(t)$ in time domain can be connected to a function $H(\nu)$ in the frequency domain by the Fourier transforms [28]:

$$H(\nu) = \int_{-\infty}^{\infty} h(t) e^{2\pi i \nu t} dt \quad h(t) = \int_{-\infty}^{\infty} H(\nu) e^{-2\pi i \nu t} d\nu \tag{5.24}$$

with ν is the frequency, t the time and i is the imaginary unit.

For discrete data sets with an even sampling rate Δt and N sampling points the function $h(t)$ can be described by $h_k = h(k\Delta t)$ where $k \in [0, N-1]$. Also the Fourier transform is discrete now, with the frequencies $\nu = n\Delta\nu = \frac{n}{N\Delta t}$, $n \in [-N/2, +N/2]$. The negative frequencies yield the same results as the positive if $h(t)$ is real. Equation (5.24 is now described by:

$$H_n = H(n\Delta\nu) = \sum_{k=0}^{N-1} h_k e^{2\pi i k n/N} \quad h_k = \frac{1}{N} \sum_{n=0}^{N-1} H_n e^{-2\pi i k n/N} \tag{5.25}$$

which is the definition of the Fast Fourier Transform (FFT).

A limit for the frequencies given by the sampling rate Δt. A signal with a periodicity of the sampling rate will always be the same in each measurement, so it will be detected as a constant, even if it is for example a sine wave. The highest possible frequency which can be detected, has its maximum and minimum amplitudes at consecutive sampling points. The upper limit is called Nyquist critical frequency and is defined as

$$\nu_{max} = \frac{1}{2\Delta t} \tag{5.26}$$

Periodic motion at higher frequencies can falsify the result since it is transformed to a different frequency than its real.

On the other hand, a motion which happens only one time during the whole measurement can not be identified as happening with a certain frequency. To detect the frequency, the motion has to appear at least two times during measurement, e.g. a sine wave has to do one full period. Depending on which effects in a system one wants to observe with Fourier methods, the measurement time has to be choosen properly. Further the number of data points N of the time series determine the frequency resolution $\Delta\nu = 1/(N\Delta t)$.

The leakage of frequencies into other frequency intervals is called aliasing. By using windows in the time domain, one can decrease aliasing. The windows are usually functions convolved with the data which cut the data into segments thus preventing the leakage of lower frequencies.

Power Spectrum The power spectrum of a quantity h_k in the time domain is defined as the values of power P at the frequencies ν_n, given by the Fourier transform H_n of h_k:

$$P(\nu_n) = \frac{1}{N^2}[|H_n|^2 + |H_{N-n}|^2] \qquad \text{for} \quad n \in [1, N/2 - 1]$$
$$P(\nu_n) = \frac{1}{N^2}|H_n|^2 \qquad \text{for} \quad k = 0, N/2 \tag{5.27}$$

It is usually normalized such, that the sum of all $P(\nu_n)$ is equal to the mean squared amplitude $1/N \cdot \sum_{k=0}^{N-1} |h_k|^2$ of the h_k.

The power spectrum can be used as an indicator of nonstationarity, but not as a proof. If at low frequencies there is considerable power, there are motions at long length scales (low frequencies) in the system, such as trends can be. Further it can give useful informations on periodicities in the system.

A first example shows the power spectrum for r_i of one particle, and the velocity power spectrum for the same particle in figure 5.8. The Nyquist frequency is 14.5 Hz for a sampling rate of 1/29 s for all measurements. The frequency resolution is 0.0035 Hz for $N = 8192$ points (this values improves the speed of the FFT).

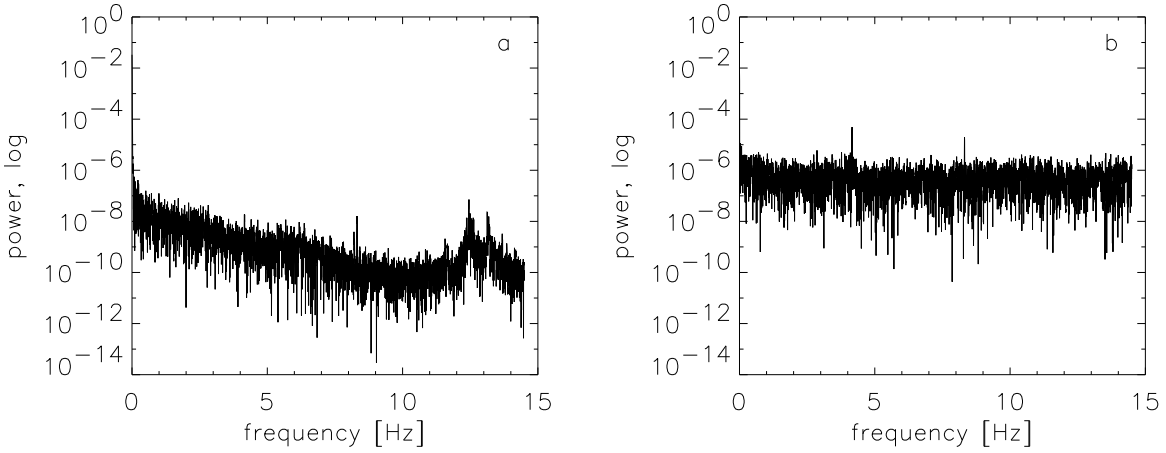

Figure 5.8: Power spectrum of a) $r(t)$ and b) $v(t)$ of one single particle. The power is normalized to the mean squared amplitude.

For each particle, the power spectra P_i of the displacements r_i and velocities v_i are computed. These are then averaged over all particles for each frequency and plotted in figure 5.9.

Interpretation of the Power Spectra The velocity power spectra reveal nearly flat spectra for all data sets, which coincides with a distribution of data points similar to

white noise (Gaussian distribution). Further an increase of noise towards lower frequencies can be seen. To emphasize this, the fraction of power located in the frequency ranges [0,0.01], [0.01,0.1], [0.1,1], [1,5], [5,10], [10,15] Hz is displayed in the graph 5.10 a) for the displacements and in b) for the velocities. Here also a slight increase of power at low frequencies emerges, while the increase of power for the displacements is much more pronounced. This could be an indication of nonstationarities such as long-term trends, which appear at low frequencies but exceed the smaller range of intrinsic motion with respect to the power.

Three sharp peaks are found located approximately at the frequencies 4.1 Hz, 8.3 Hz and 12.5 Hz. These appear in all data sets and for both velocity and displacement (the peak at 12.5 Hz is hidden in the high frequency noise for the displacements). Since they are visible for all data sets equally, and do not depend on the physical quantity r or v, they are likely caused by an external influence. The two peaks at 8.3 and 12.5 Hz could be the first and second harmonics of the 4.1 Hz peak (harmonics appear at $k \cdot \nu, k \in N$). Also possible is a camera vibration in resonance. The 12.5 Hz peak could be caused by a vertical oscillation of the particles. To emphasize the peaks, the maximum values of power in frequency intervals of 1 Hz from 0 to 15 Hz are displayed in figure 5.11. The mentioned peaks are marked.

Finally at 6 to 7 Hz a bump appears in the power spectra of the displacements. It is also common for all data sets, but does not emerge in the velocity power spectra, where at best a slight drain can be seen around 7 Hz. The frequency range matches the expected values foe the Einstein frequency of oscillations of particles around their mean lattice site. Power increases within this bump, so the energy of the crystal must be increased by an event happening at that frequency. It has been found, that a correlated oscillation of particles in the crystal can couple to that frequency. This is also called a saturated instability and was found by [14].

However, it is difficult to assume any reasons for the features of the power spectra unless the trends in the system have been investigated. After the detrending procedure we will repeat the spectral analysis and compare the structures to detect any correlations of frequencies which vanished with common trends.

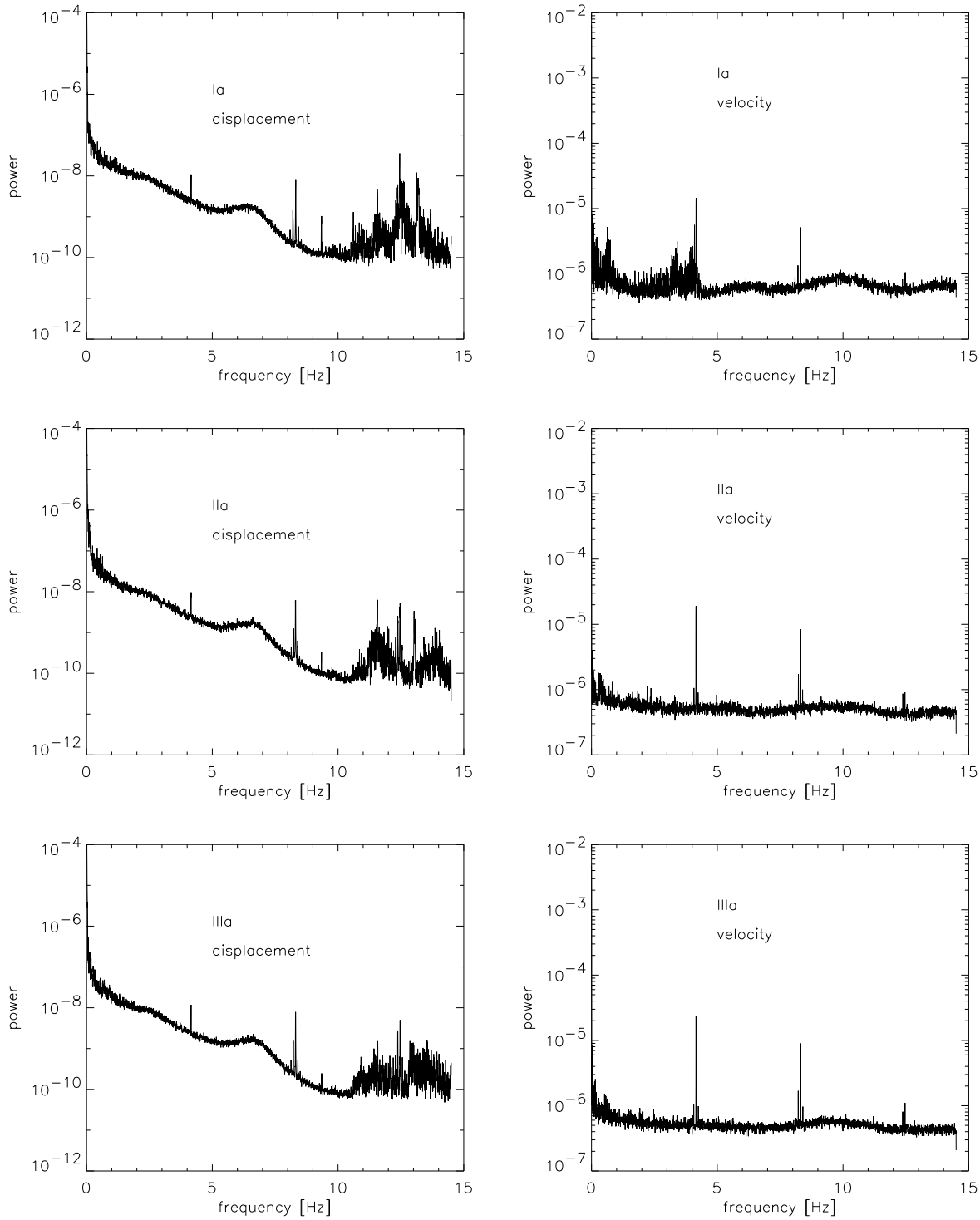

Figure 5.9: Power spectra of displacement (left) and velocity (right), averaged over all particles. Data sets Ia, IIa, IIIa (low resolution). The y-axis has a logarithmic scale.

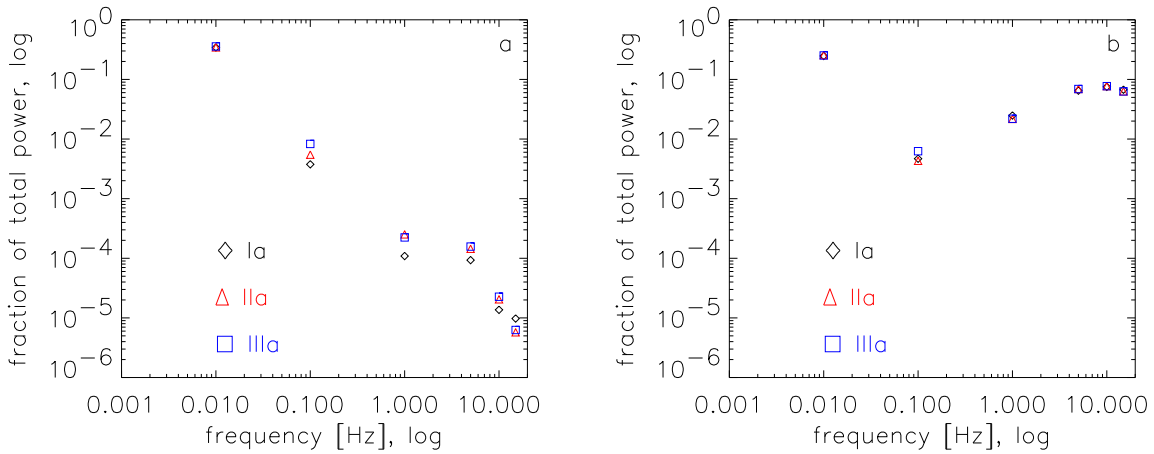

Figure 5.10: Log-log plot of the fraction of total power in frequency ranges [0,0.01], [0.01,0.1], [0.1,1], [1,5], [5,10], [10,15] Hz for a) displacement and b) velocities.

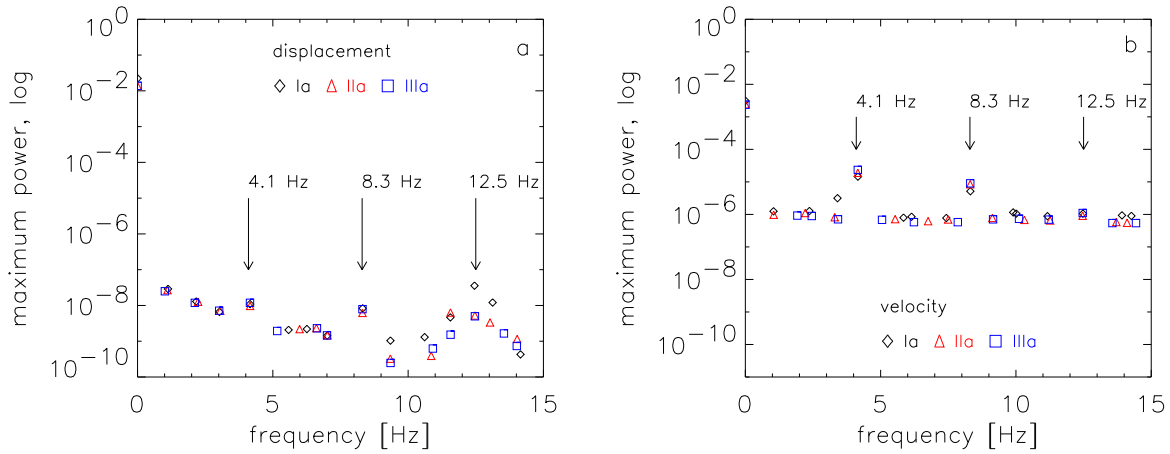

Figure 5.11: Maximum values of power in frequency intervals of 1 Hz from 0 to 15 Hz for a) displacement and b) velocities. Marked by arrows are the peaks detected in the power spectra.

5.2.1.3 Summary

The time series of averaged displacements reveal strong nonstationarities likely caused by trends on long time and length scales. This is emphasized by the deviations of the running mean and by the analysis of the frequency spectrum which shows an increase of power towards low frequencies.

The velocities seem to be rather stationary with respect to the averaged quantities, but the power spectra show the same feature as the displacements although weaker by some magnitudes. But if a trend contaminates the particle coordinates it will for sure also affect the velocities derived from them, though it can not have high influences if it happens on much larger time scales than the frame rate which determines the velocity.

The reasons of the nonstationarities could partly be connected to common particle motions, which will be the subject of the next section.

5.2.2 Removing of Common Trends

Removing trends from a time series is a lengthy business. The danger is to remove not only the trend, but part of the dynamics too. Filters, for example high pass or smoothing algorithms, should only come into use, if one knows how they affect the parts of the time series not subject to the trend. Since not much is known about sources, time or length scales of trends in plasma crystals, the detrending must be done more carefully by finding theoretical models for the trends and apply them to the data.
Thus a measured time series $x_{meas}(t)$ can be splitted into

$$x_{meas}(t) = x_{trend}(t) + x_{fluct}(t) \tag{5.28}$$

were $x_{trend}(t)$ is any time dependent trend and $x_{fluct}(t)$ a motion fluctuating around the trend, which is the quantity of interest. In the following chapters, $x_{trend}(t)$ will be identified in more detail for the plasma crystal. This will be done for the original coordinates $x(t)$ and $y(t)$ in the images. Trends which can be identified will be fitted as models to the data. After each section, the treated trend is subtracted from the coordinates, and the 'new' coordinates are used as input for the next step. These will be named x and y again to simplify the terms. Displacement $r(t)$ and velocity $v(t)$ for further investigation will then be derived from the detrended time series.

In figure 5.12 one can see the reason for the large deviations of $\overline{r}_w$. The trajectories of all particles of a data set (IIa) are drawn for 2000 consecutive frames. Visible becomes a rotation of the whole crystal, which will be treated in section 5.2.2.1. Further an oscillation of the whole crystal in the confining potential well is assumed, but not visible in the plot. The sharp peaks in the trajectories will be subject to chapter 5.2.2.4.

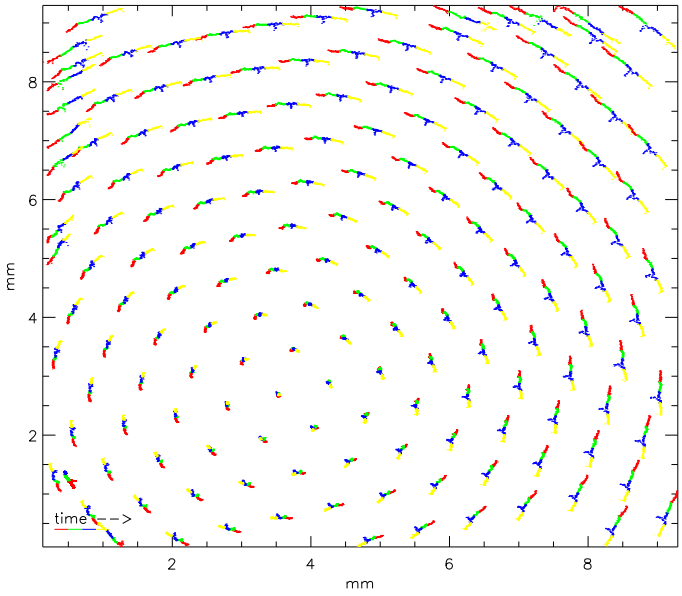

Figure 5.12: Overlay of particle trajectories of 2000 consecutive frames. The colors from red to yellow indicate the propagating time.

5.2.2.1 Rotation

The rotation of the crystal has been observed as an effect due to magnetic fields [29]. Here the earth magnetic field B_E is likely to be the source of rotation. Due to the high electric field in the chamber, a $\mathbf{v} \times \mathbf{B_E}$ drift acts on the ions. These drag the dust particles with them and cause the crystal to rotate within the confinement. For low U_{pp} the rotation is a rigid body rotation ([29]) and could easily be substracted for all particles. It will be examined if this is the case here.
With the rotation equation (5.28) can be written as

$$\begin{pmatrix} x(t) \\ y(t) \end{pmatrix} = \begin{pmatrix} x_{rot}(t) \\ y_{rot}(t) \end{pmatrix} + \begin{pmatrix} x_{rest}(t) \\ y_{rest}(t) \end{pmatrix} + \begin{pmatrix} x_{fluct}(t) \\ y_{fluct}(t) \end{pmatrix} \tag{5.29}$$

The index *rest* indicates trends not identified yet. For a rigid body rotation, the angular velocity Ω is constant for all particles. By introducing polar coordinates $R(t), \Theta(t)$ one can write down the transformation

$$x_{rot}(t) = \overline{R} \cdot \cos(\Theta_0 + \Omega \cdot t) + X \qquad y_{rot}(t) = \overline{R} \cdot \sin(\Theta_0 + \Omega \cdot t) + Y \tag{5.30}$$

with X, Y are the coordinates of the rotation center, $\overline{R}$ is the constant mean radius of the particle to (X, Y), Θ_0 is the starting angle and Ω is the constant angular velocity. The aim is now to fit a rotational motion to each single particle trajectory by the use of the fitting procedure described in section 4.3.2.2 with values for Ω and (X, Y) as result. The

function used for the fit was:

$$\begin{aligned}(x_i(t)-\overline{x}_i)^2+(y_i(t)-\overline{y}_i)^2 &= \\ [X_i+\overline{R}_i\cos(\Theta_{i,0}+\Omega_i t)-\overline{x}_i]^2 &+ [Y_i+\overline{R}_i\sin(\Theta_{i,0}+\Omega t)-\overline{y}_i]^2 \end{aligned} \tag{5.31}$$

with $\overline{x}_i, \overline{y}_i$ denoting the mean of the coordinates x_i, y_i for one particle. The parameters estimated by the fit were $\overline{R}_i$, $\Theta_{i,0}$, Ω_i and the coordinates of the center of rotation, X_i, Y_i. The index i emphasizes that all values are obtained for each particle in particular here. Starting values were derived by finding a center of rotation with geometrical methods, and then transforming $x(t)$ and $y(t)$ to polar coordinates, which yielded R and Θ_0. Then the velocities of Θ were derived as the difference of Θ in two frames, divided by the time interval Δt between two consecutive frames. The mean of all velocities gave an estimate of Ω_i.

The advantage of the above function was, that both particle coordinates x and y are connected. This restricts the parameter range and the fit gives more secure results, since the parameters as $\overline{R}_i$, $\Theta_{i,0}$ and Ω_i should not vary for x and y of one particle. One more restriction is, that Ω,X and Y should be the same for all particles, if the model is correct. In figure 5.13, the values obtained for Ω_i are displayed. As global angular velocity Ω the median of all Ω_i is taken. The median is derived by taking the middle of all obtained values. It has the advantage that far outlying points are not weighted as much as by the mean value. In this case, points which deviate strongly must be seen as wrong fitting results, since there can be just one center of rotation. The mean absolute deviation $1/N_P \cdot \sum_{i=1}^{N_P} |\Omega_i - \Omega|$ is taken as a measure for the deviation of Ω_i from the median (as the median, the mean absolute deviation is not as sensitive to outlying points as the standard deviation).

Ω_i is plotted versus $\overline{R}_i$ in figure 5.13, and one can see that outlying points are located at low $\overline{R}_i$. That means they originate from particles located nearly at the rotation center. There it is difficult to fit a rotation due to the small distances the particles move on the circle.

Further a linear fit to $\Omega_i(\overline{R}_i)$ justifies the assumption of a rigid body rotation, since the gradient of the line is close to zero (see also table 5.3). Figure 5.13 shows the angular velocities versus U_{pp} for the different data sets in comparison in the lower right panel. The rotation seems to decrease slowly for higher voltages.
The location of the center of rotation is displayed in panel 5.14, where X_i is plotted versus Y_i as obtained for each particle. Here also the median had been taken as common value and is marked in red. In that diagram also the motion of the rotational center between the different measurements can be observed. This motion is induced by the change of U_{pp}.

Experiment	Ia	IIa	IIIa
Ω [rad/s] (median)	-0.0023 ± 0.0002	-0.0020 ± 0.0001	-0.0017 ± 0.0003
Ω_{fit} [rad/s] (lin. fit to $\Omega_i(R_i)$)	-0.0024	-0.0021	-0.0018
gradient of $\Omega_i(R_i)$ [rad·s^{-1}m^{-1}]	$9.3 \cdot 10^{-6}$	$1.54 \cdot 10^{-5}$	$1.41 \cdot 10^{-5}$

Table 5.3: Ω obtained as median from the Ω_i and fit parameters of the linear fit to $\Omega(\overline{R}_i)$

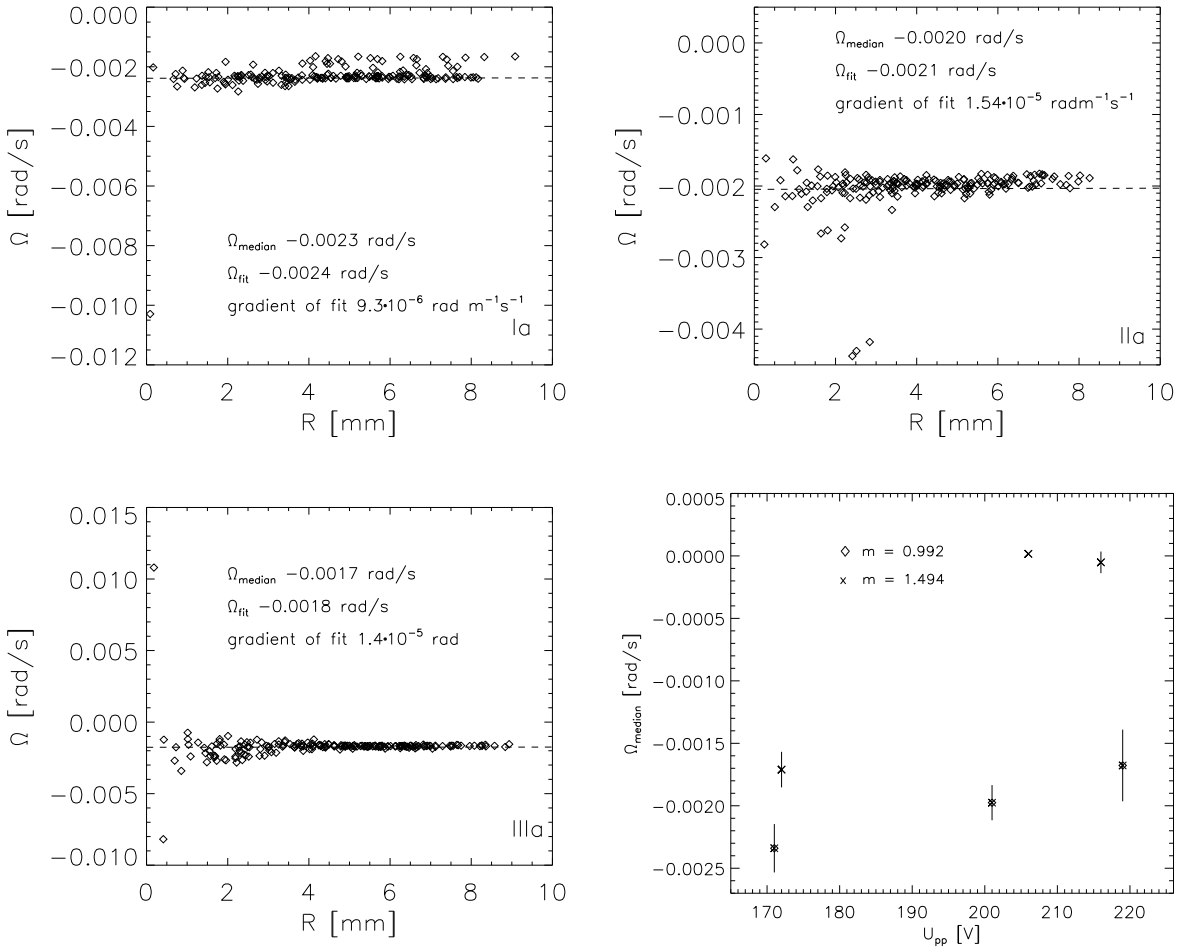

Figure 5.13: Ω_i vs. $\overline{R}_i$. The dashed lines are linear fits to $\Omega_i(\overline{R}_i)$. The median of Ω_i and the fit parameters are displayed in the diagrams. The lower right panel shows the median Ω vs. U_{pp} for all data sets.

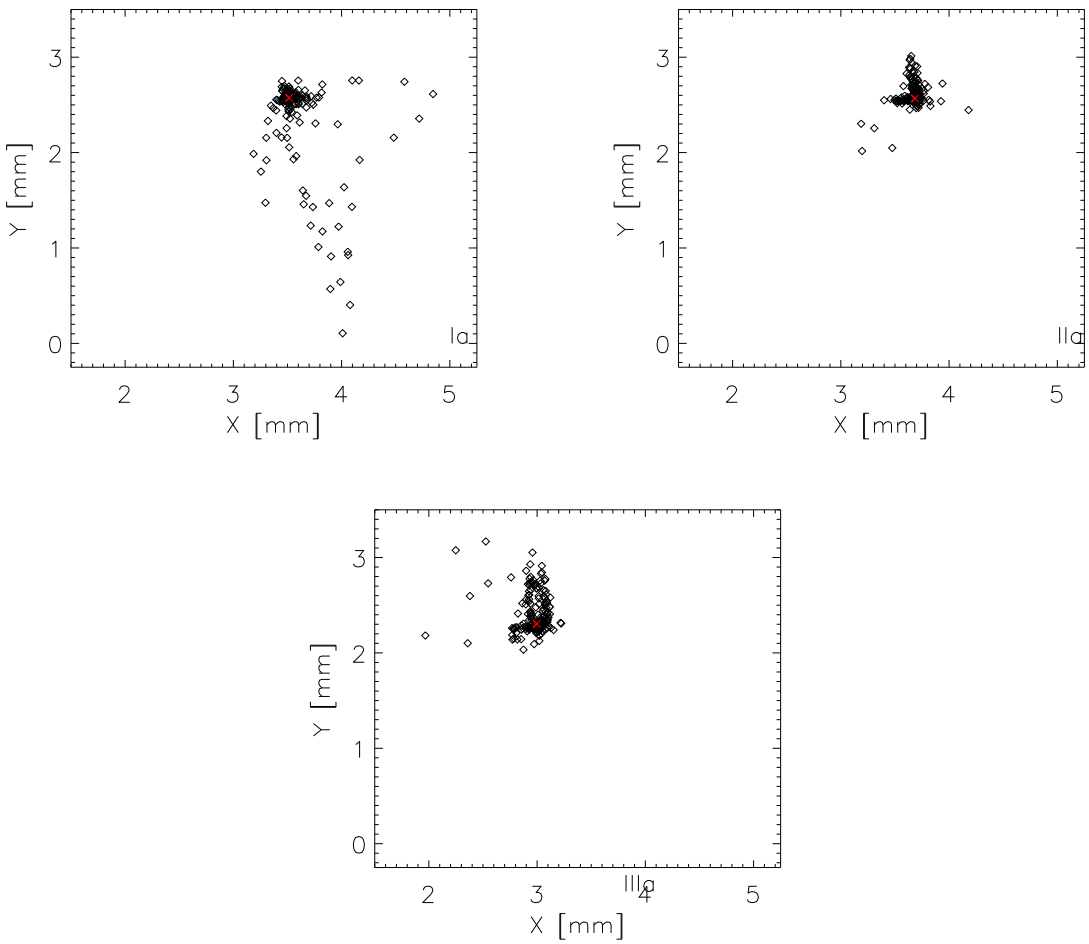

Figure 5.14: Y_i vs. X_i. The red cross marks the median (X, Y) for all particles.

5.2.2.2 Oscillation in the Confinement Potential

The next step was to assume an oscillation of the whole crystal in the external confinement potential. This would show up in a translational motion of X and Y:

$$\begin{pmatrix} x(t) \\ y(t) \end{pmatrix} = \begin{pmatrix} x_{rot}(t) \\ y_{rot}(t) \end{pmatrix} + \begin{pmatrix} x_{trans}(t) \\ y_{trans}(t) \end{pmatrix} + \begin{pmatrix} x_{rest}(t) \\ y_{rest}(t) \end{pmatrix} + \begin{pmatrix} x_{fluct}(t) \\ y_{fluct}(t) \end{pmatrix} \tag{5.32}$$

with

$$x_{trans}(t) = X(t) \quad , \quad y_{trans}(t) = Y(t) \tag{5.33}$$

The time dependent $X(t), Y(t)$ have been found by taking the X and Y from the previous section as starting values, and calculating for each particle a mean radius $\overline{R}_i$. Then in each frame k the $\overline{R}_{i,k}$ of the visible particles $N_{P,k}$ were taken and following function was fitted to them for each frame k:

$$\overline{R}_{i,k}^2 = (x_{i,k} - X_k)^2 + (y_{i,k} - Y_k)^2 \tag{5.34}$$

This function makes use of the assumption that, in the case of constant particle radii, the above condition has to be fulfilled in every frame k by all particles i visible in that frame.

The fit yielded time dependent $X(t)$ and $Y(t)$, which are plotted in figure 5.15 for data set Ia, IIa, IIIa. There are some sharp peaks visible, which indicate a fast non-periodic shaking of the whole crystal. This looks like an external disturbation, very likely caused by power fluctuations of the RF generator (see chapter 5.2.2.4).

The translational motion of the rotation center happens at the highest time scales recorded. Thus it differs from other trends which only become visible on large time and length scales. Note that by subtracting $X(t)$ and $Y(t)$ from the time series of $x_i(t)$ and $y_i(t)$ respectively, the motion of particles is transformed into a moving coordinate system. Fluctuations such as camera vibrations will be eliminated in this coordinate system, too.

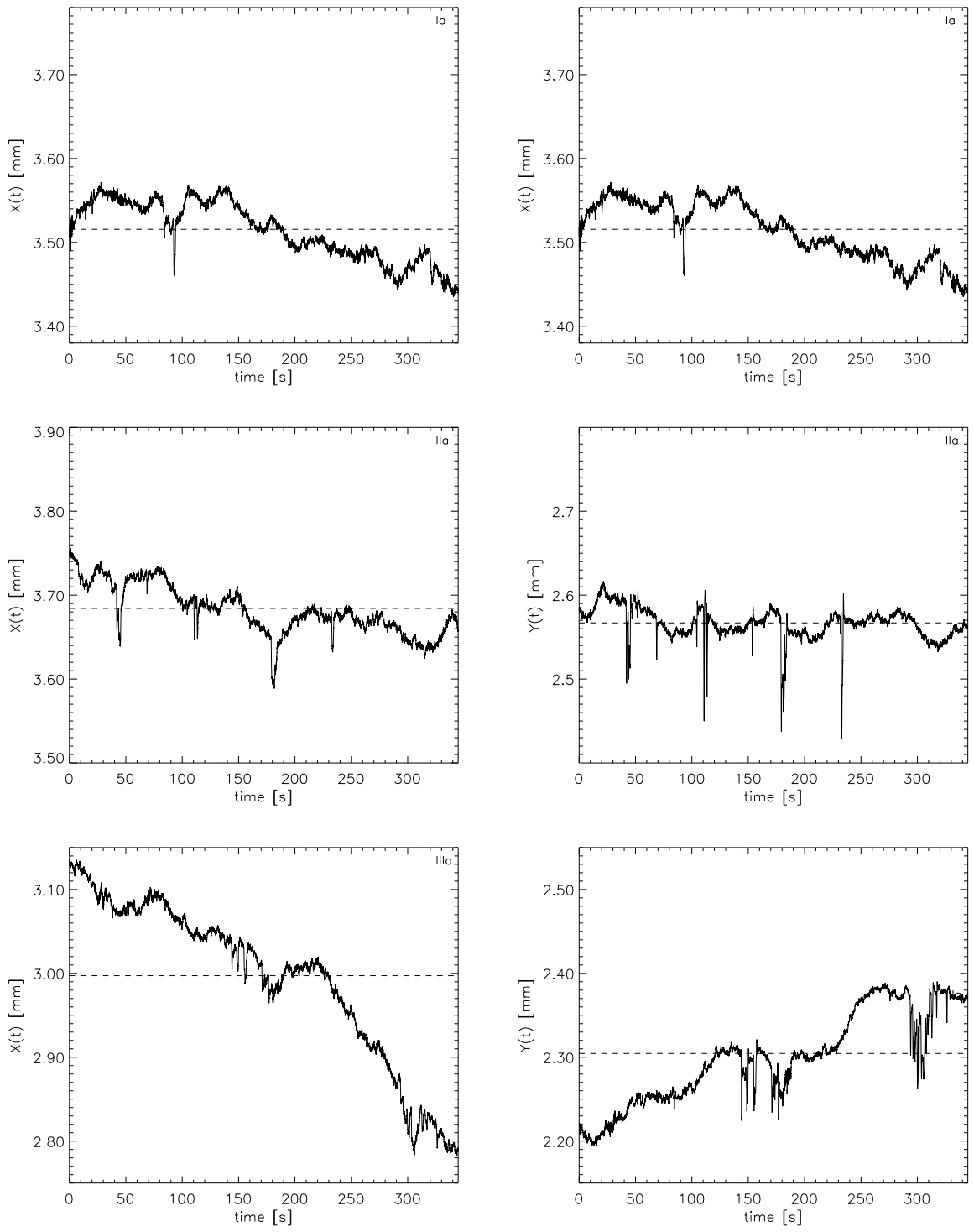

Figure 5.15: $X(t)$ (left) and $Y(t)$ (right). The dashed line is the median value of X or Y from the first fit (equation (5.31)) which was used as starting value here.

5.2.2.3 Flows

After eliminating rotation and translational movements, there still seemed to be a trend left, at least for some particles as indicated in figure 5.16. A linear fit

$$x_i(t) = x_{i,0} + c_{x,i} \cdot t \qquad y_i(t) = y_{i,0} + c_{y,i} \cdot t \tag{5.35}$$

has been made on the trajectories. The gradients $c_{x,i}, c_{y,i}$ are represented as arrows in figure 5.16, which show the direction and the relative strength of the motion for each particle. For comparison the magnitude of the arrows is illustrated in the lower right part of the image.
There seems to be a slow linear flow of groups of particles in opposite directions in the crystal. The problem here was that a common model could not be found, though there is clearly visible spatial connection of the flow for the particles. Therefore, for each particle the gradient of the linear fit to this particle has been subtracted.

The reason for the flow could be either a shear flow or an artefact due to the former detrending procedures. If the particles did not rotate on pure circular trajectories but on elliptical orbits around $(X(t), Y(t))$, the subtraction of a circular motion could pretend a flow in the crystal. An indicator for this is the time scale of the motion. In data set IIa the linear flow for a particle with a gradient yields a velocity of $9.75 \cdot 10^{-3}$ mm/s. The angular velocity for this data set was $2.0 \cdot 10^{-3}$ rad/s $= 11 \cdot 10^{-3}$ mm/s for a radius of approximately 5.5 mm. Both velocities are of the same order of magnitude, which also accounts for other particles. It is difficult to decide from this if a real physical flow or an artefact of other detrending is the case here.

5.2.2.4 Radial Contractions of the Crystal

The changing of the radius observed in figure 5.12 could be identified as a problem with the RF power generator. Small fluctuations of the power caused the crystal to contract ('breath') through an influence on the strength of the confinement. There is no way to fit a model to this disturbation. Even if it would be possible, the question arises whether the fluctuation of the particles around their mean lattice site is somehow affected by the change in the confinement. The best way seemed to be to cut out the disturbed segments from the trajectories of all particles.

To locate the radial fluctuation in time as a common motion, again polar coordinates have been calculated from the detrended time series, all particle radii $\overline{R}_{i,k}$ in each frame k are summed up, yielding a 'total' radius $\overline{R}_k$ for each time step:

$$\overline{R}_k = \sum_{i=1}^{N_{P,k}} R_{i,k} \tag{5.36}$$

This has been normalized by division by $\overline{R}_0$ (total radius in the first frame), and plotted in figure 5.17. Every time a 'breathing' appeared, the mean radius shows larger fluctuations.

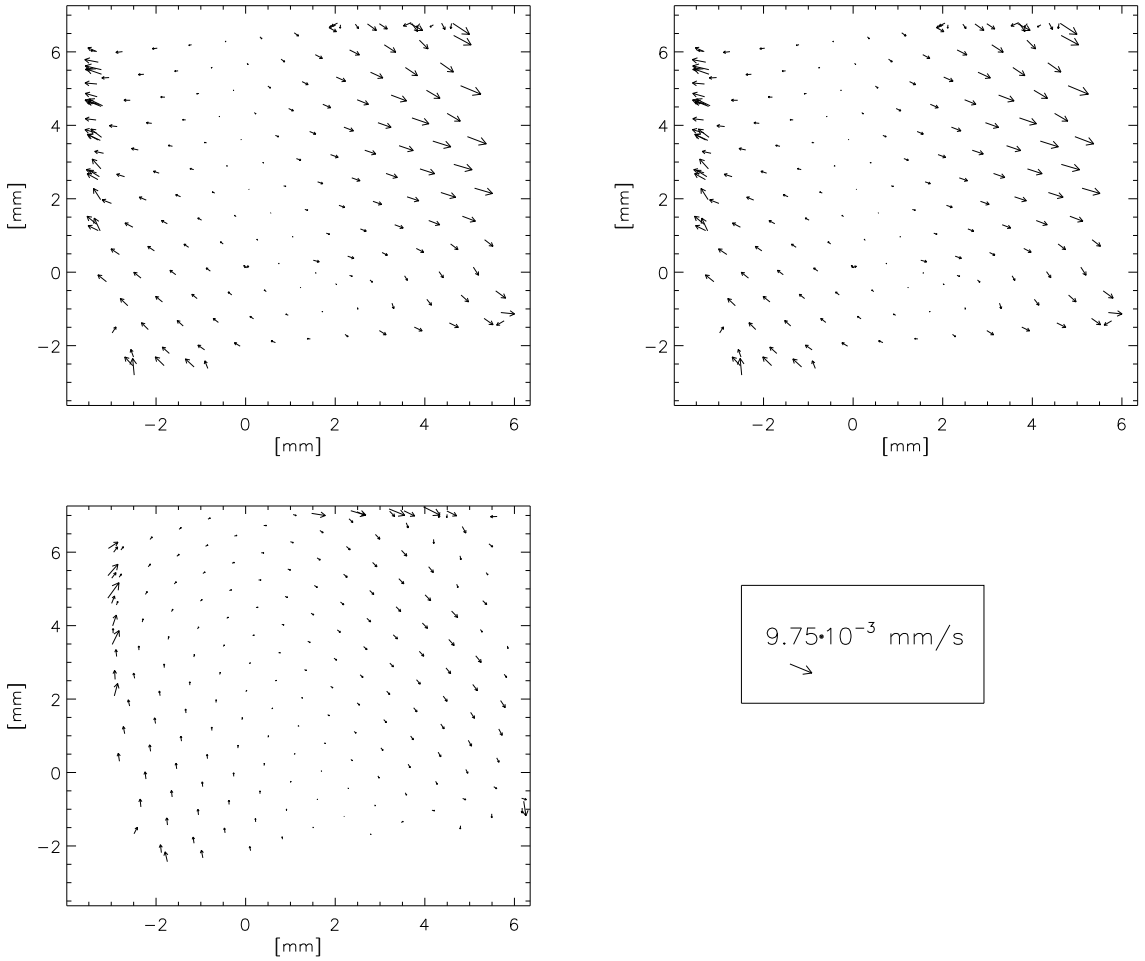

Figure 5.16: Flow of particles represented as arrows for data sets Ia (upper left), IIa (upper right) and IIIa (below).

Overplotted is the total radius calculated for the original (not detrended) data. Some of the fluctuations are not clearly visible in the $\overline{R}_k$, but showed up in the original data. The pieces of trajectories which were removed are marked in colors.

5.2.3 Result of Detrending

The result of the detrending is graphically shown in figure 5.18 for one data set. The trajectories of all particles in the field of view are plotted, as they are located in the crystal, after the different steps of trend removing.

In summary, following model was fitted to the particle trajectories:

$$\begin{aligned} x(t) &= X(t) + \overline{R} \cdot \cos(\Theta_0 + \Omega t) + c_x t + x_{fluct}(t) \\ y(t) &= Y(t) + \overline{R} \cdot \sin(\Theta_0 + \Omega t) + c_y t + y_{fluct}(t) \end{aligned} \tag{5.37}$$

It includes a rotation of the whole crystal, a translational motion of the crystal due to oscillations in the confining potential and a common flow of groups of particles. Also a radial fluctuation with respect to the center of rotation has been treated.

The coordinates used from now on are only the fluctuating parts $x_{fluct}(t)$ and $y_{fluct}(t)$, without the segments identified as disturbed by power fluctuations.
From this, for each particle i with a trajectory length of N_t points the mean lattice site $x_{ml,i}, y_{ml,i}$ and displacement $r_i(t)$ are calculated:

$$x_{ml,i} = \frac{1}{N_t} \sum_{k=1}^{N_t} x_{fluct,i}(t_k), \qquad y_{ml,i} = \frac{1}{N_t} \sum_{k=1}^{N_t} y_{fluct,i}(t_k) \tag{5.38}$$

$$r_i(t) = \sqrt{(x_{fluct,i}(t) - x_{ml,i})^2 + (y_{fluct,i}(t) - y_{ml,i})^2} \tag{5.39}$$

The velocities for further examination are calculated from the detrended time series as described in equation (5.18). To give an impression on the kind of data sets which will be used for further analysis, the time series of the displacement $r(t)$ and the absolute velocity v are displayed in figure 5.19 for one particle before (left panels) and after (right panels) the detrending procedure.

Repeat of the Test for Stationarity As a final test, running mean and standard deviation are calculated with the same technique as in section 5.2.1 and presented in figures 5.20 and 5.21 for the time dependence of the quantities, and in figure 5.22 the percentages of deviations Σ from the mean as defined in equation (5.23) smaller zero are shown.

Though the deviations of the running mean of the displacements are smaller by the order of 100, and instead of a linear course now fluctuate around the mean, still only a maximum of 60 % of the values of $\hat{r}_w$ lie within the confidence interval for data set Ia, while this value decreases strongly for data sets IIa and IIIa. The standard deviations $\hat{\sigma}_{r,w}$ also still deviate for different window sizes and reach a maximum of 70 % of points close enough to the mean.

The situation for the velocities looks better by far with regard to a stationary time series. Nearly 100 % of all point for $\hat{v}$ and $\hat{\sigma}_{v,w}$ are located within the lines indicating the allowed deviation.

Before a last statement is given to the stationarity of the system, the power spectra are analysed.

The frequency analysis done before is also repeated and displayed in the diagrams 5.23 where the spectra are shown, 5.24 with the total power in the frequency ranges [0,0.01], [0.01,0.1], [0.1,1], [1,5], [5,10], [10,15] Hz and the maximum power in frequency intervals of 0.1 Hz5.25.

The sharp peaks at 4.1, 8.3 and 12.5 Hz stayed for the displacement spectra. For the velocities the last one vanished, but it can be concluded that the origin of the peaks will be, as discussed in section 5.2.1.2, externally triggered.

The high frequency noise in the displacement spectra vanished. It might have corresponded to the oscillation of the whole crystal, which was fitted to the data as a frame-to-frame motion, so it happened at the highest frequency, namely the camera frame rate. This could have appeared as a high frequency noise due to aliasing. Also the low frequency noise in the velocity spectra is gone.

What is left is the increase of power to low frequencies in the displacement spectra, which will be interpreted as a nonstationarity, since this coincides with the results of the running averages. Also the bump at 7 Hz stayed, so it was not induced by one of the detected trends, but more likely due to the correlated particle oscillation explained before.

As a final conclusion we state that though a lot of common particle motions were detected and subtracted from the data, still nonstationarities are left in the average displacements. The velocities instead can be called stationary. Further the analysis of the frequency spectra reveals a feature which seems to be a common particle oscillation not caused by external forces, but by correlations due to particle interaction.

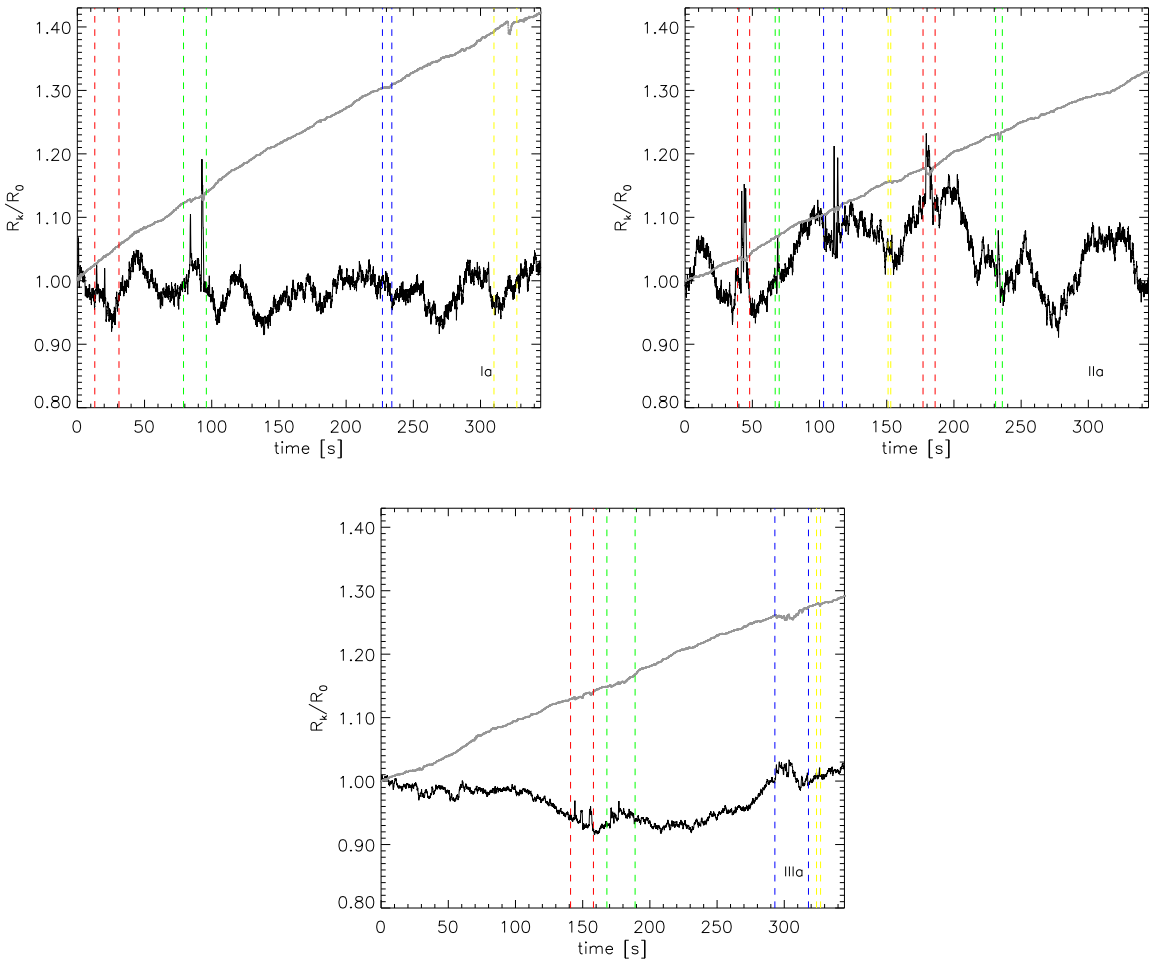

Figure 5.17: $\overline{R}_k$ vs. time for an illustration of radial breathing. The grey graph is the total radius of the original, raw data. The vertical colored lines mark the segments that are cut out between.

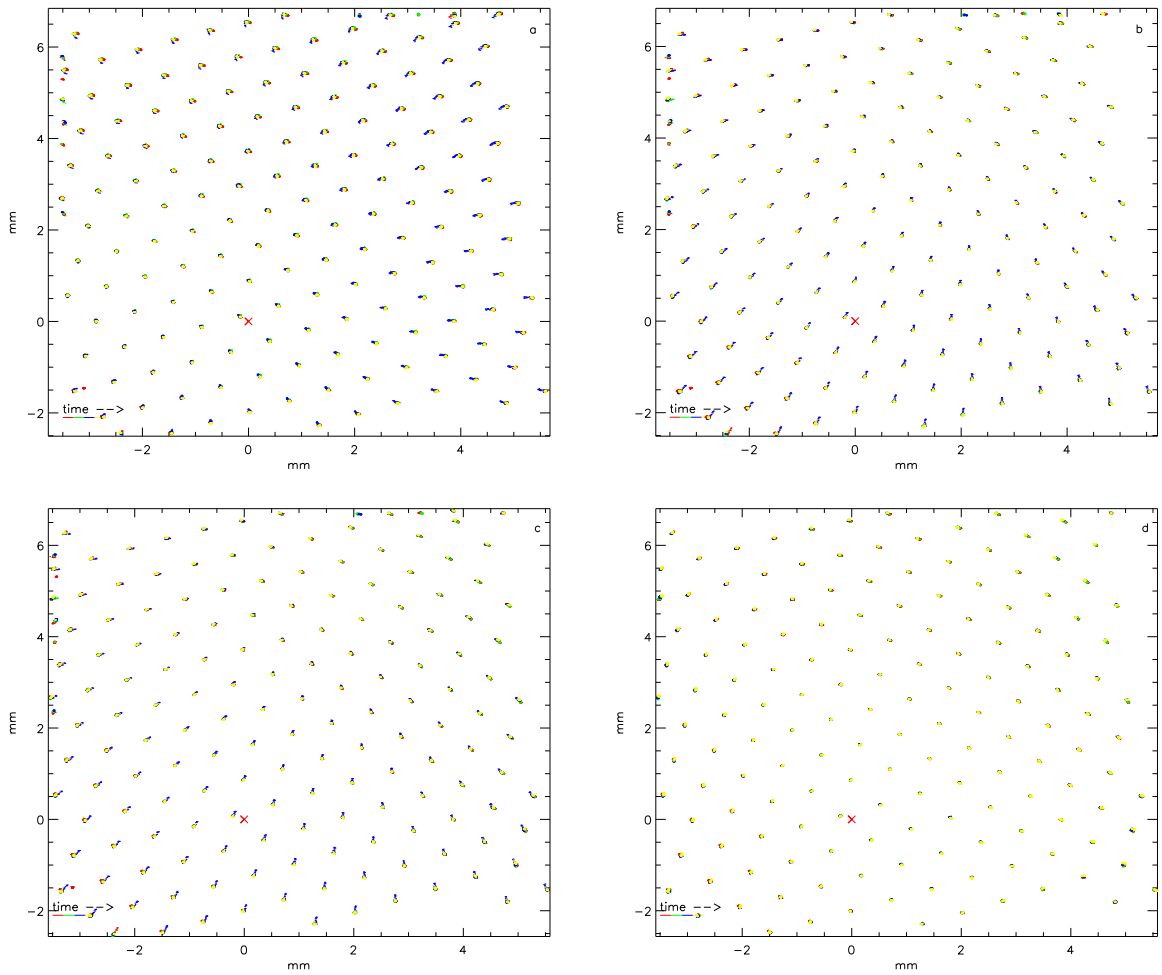

Figure 5.18: Effect of removing common trends from the data. The images show an overlay of the particle coordinates of 2000 frames after the consecutive subtraction of following trends: a) Rotation, b) Translation, c) Linear flow, d) Segments with large radial fluctuations.

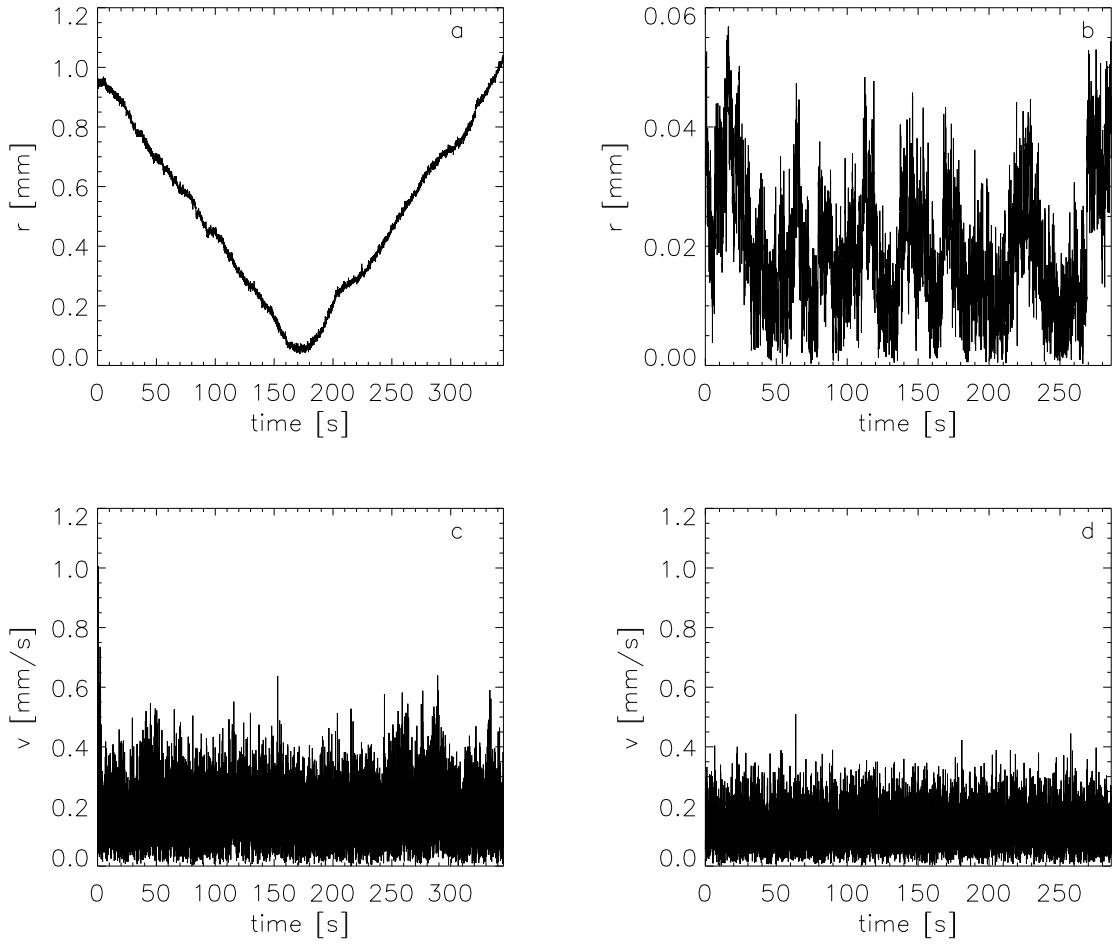

Figure 5.19: Top panels: Time series of $r(t)$ of a single particle before (left) and after (right) the detrending. Bottom: Velocity $v(t)$ before (left) and after (right) detrending for the same particle.

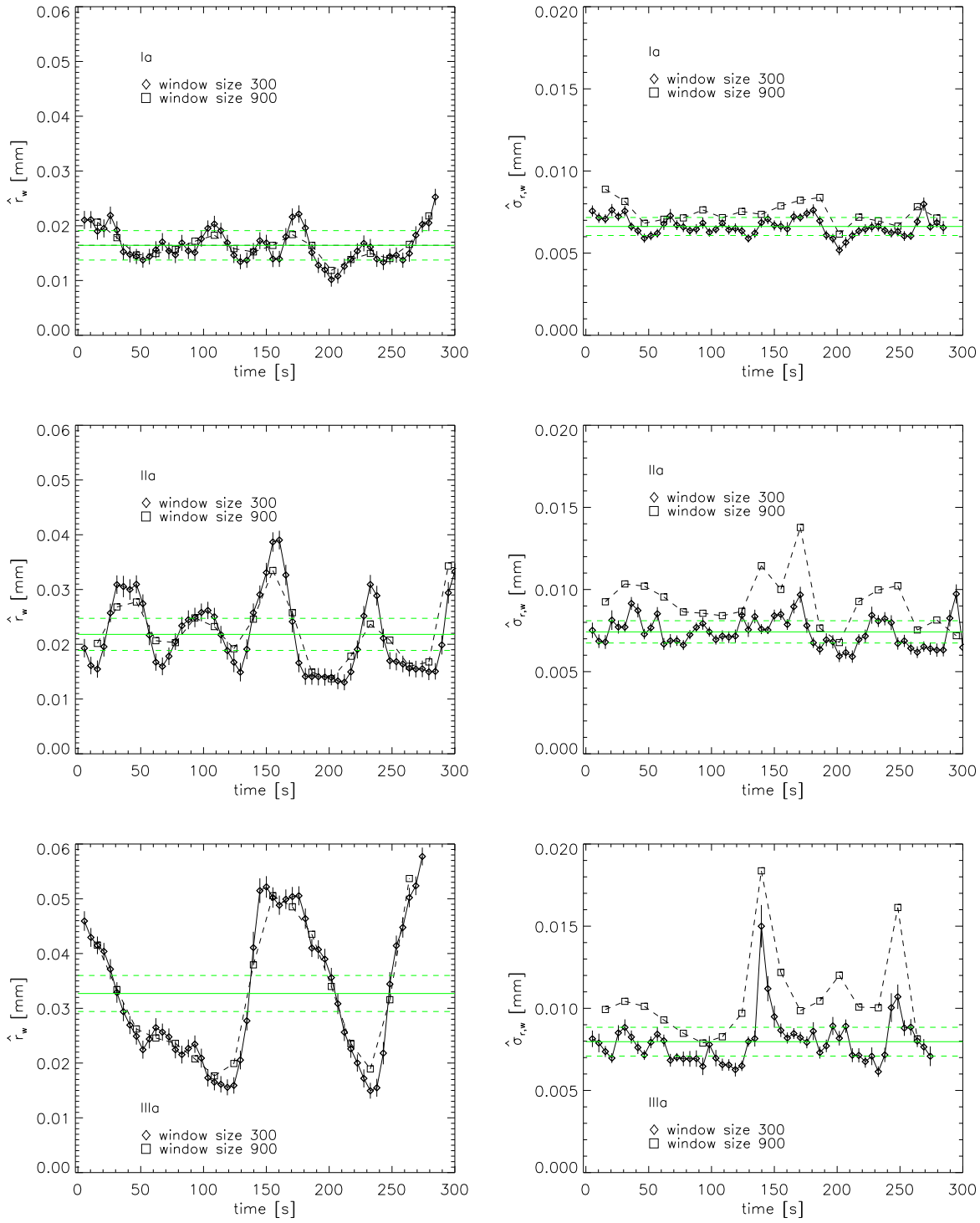

Figure 5.20: Running mean $\hat{r}_w$ (left images) and running standard deviation $\hat{\sigma}_{r,w}$ (right images) for two window sizes. The error bars where only plotted for the window size 300. The solid line shows the mean over all frames.

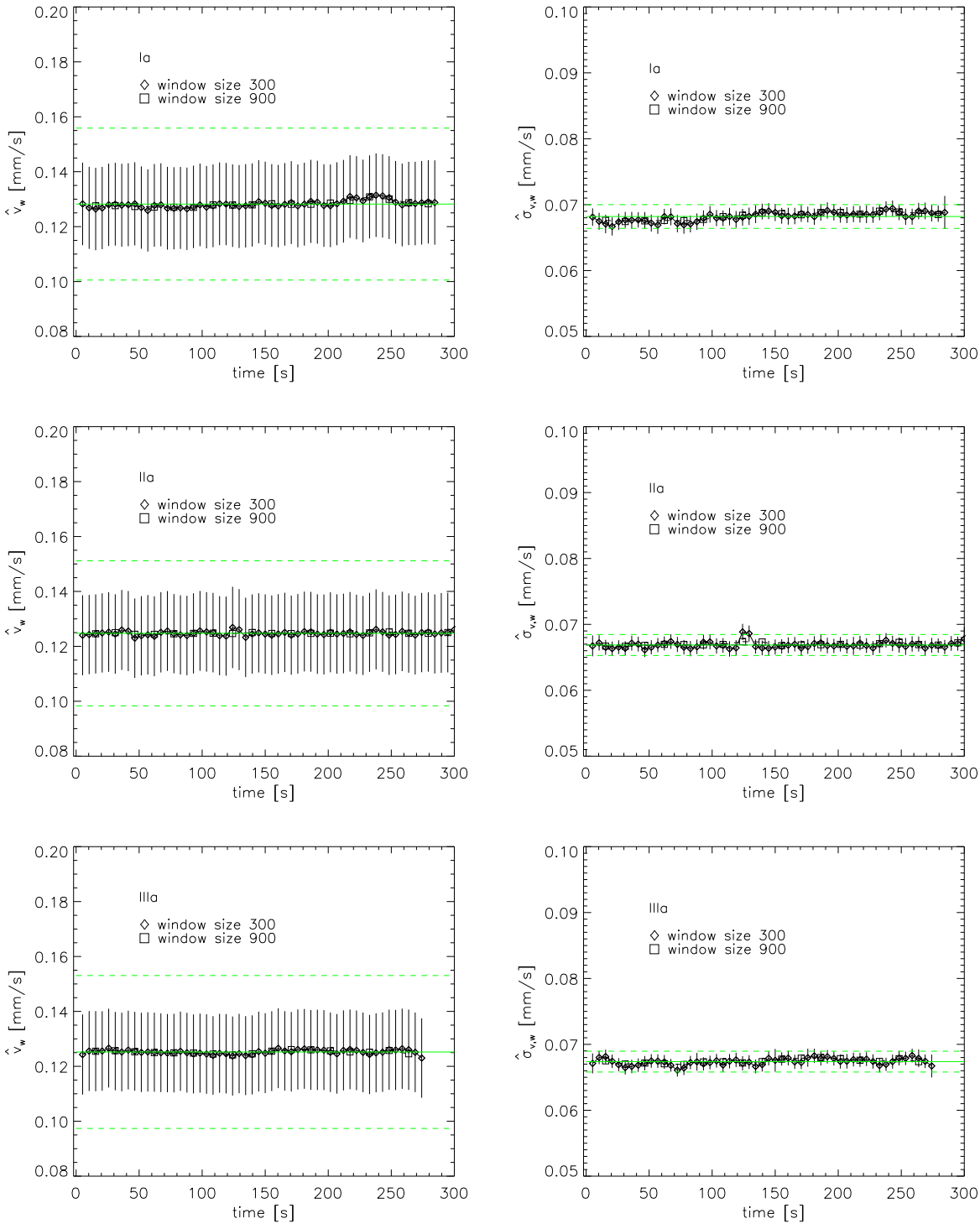

Figure 5.21: Running mean $\hat{v}_w$ (left images) and running standard deviation $\hat{\sigma}_{v,w}$ (right images) for two window sizes. The solid line shows the mean over all frames.

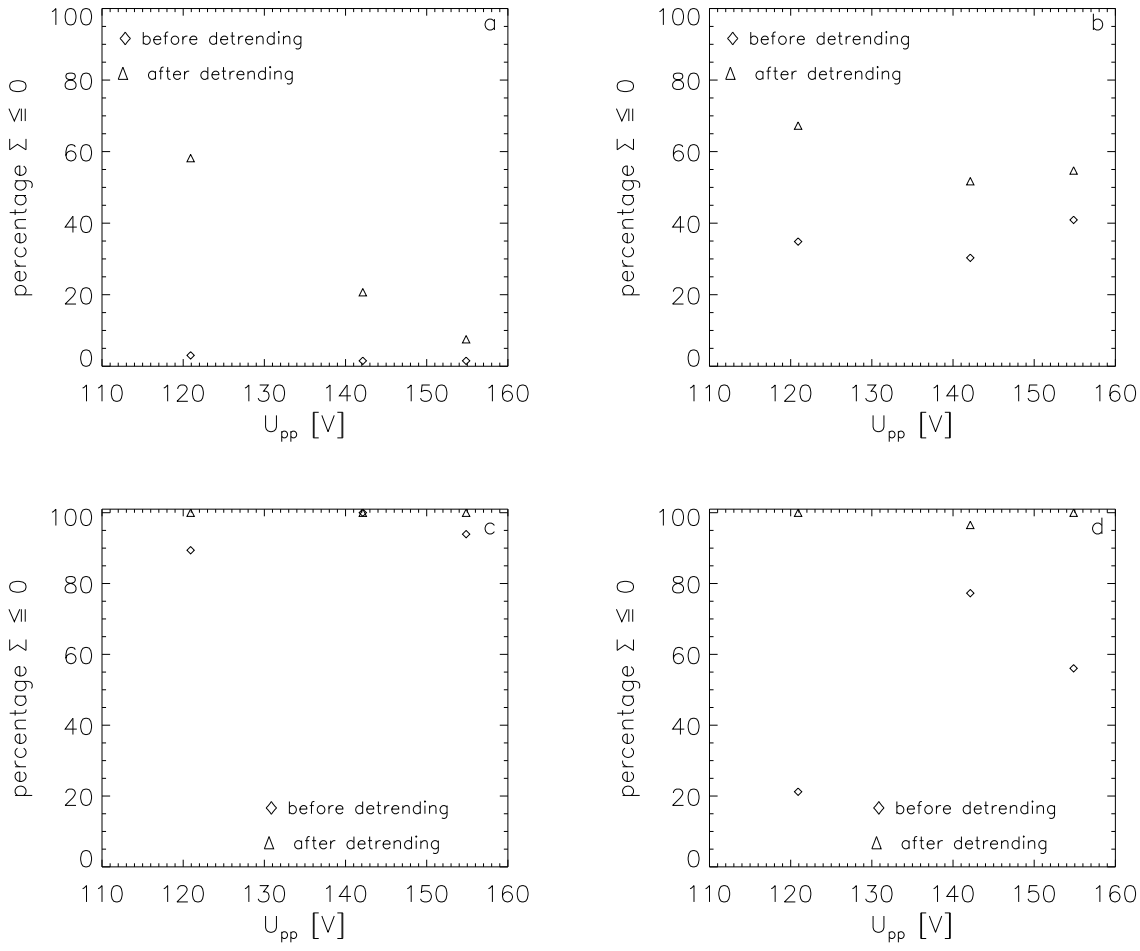

Figure 5.22: Percentage of differences Σ smaller zero compared with the quantities before trends were removed for a) running mean of the displacement, b) running standard deviation of the displacement, c) running mean of the velocity, d) running standard deviation of the velocity. For stationary systems 100 % should be smaller zero.

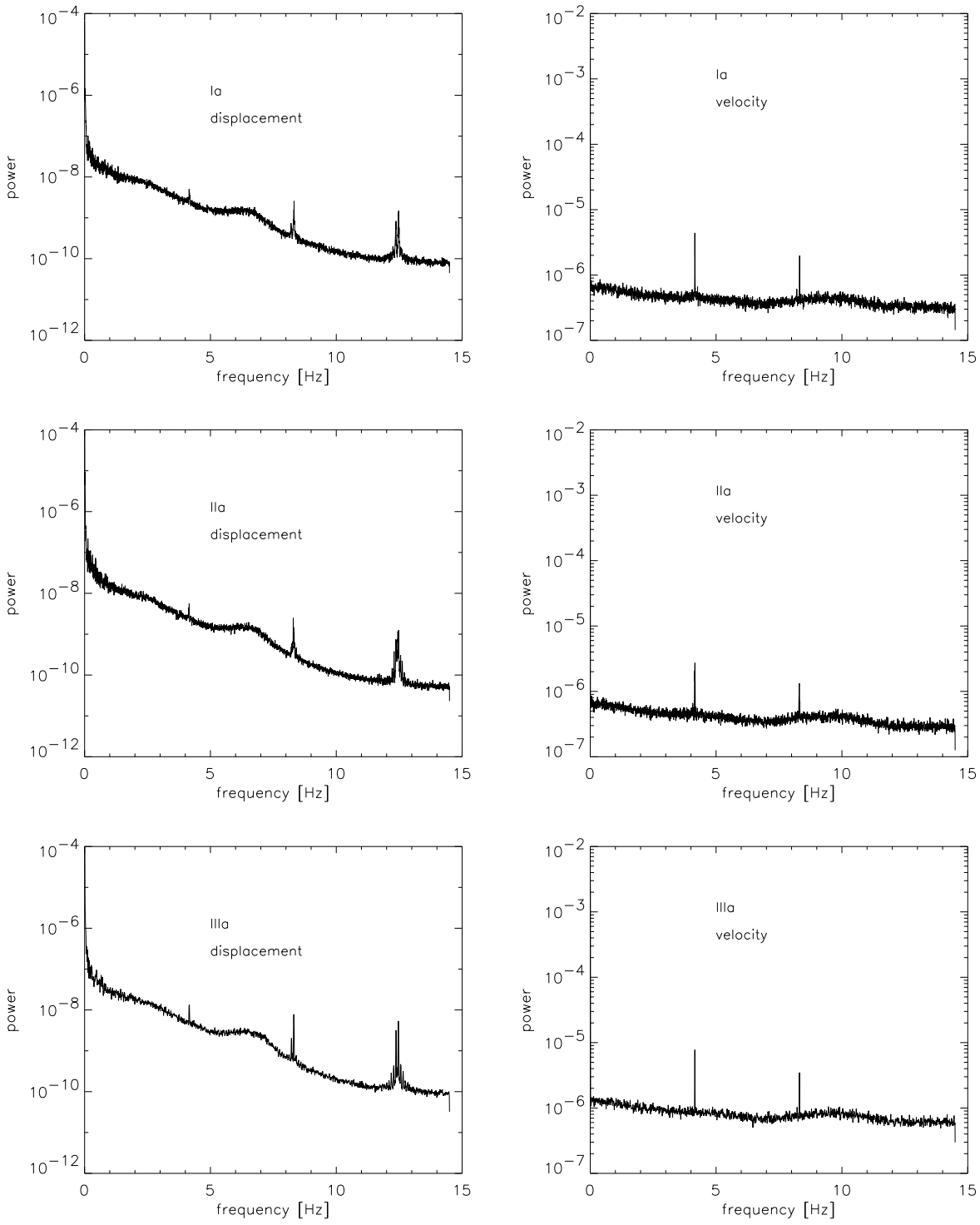

Figure 5.23: Power spectra of displacement (left) and velocity (right), averaged over all particles. Data sets Ia, IIa, IIIa after detrending.

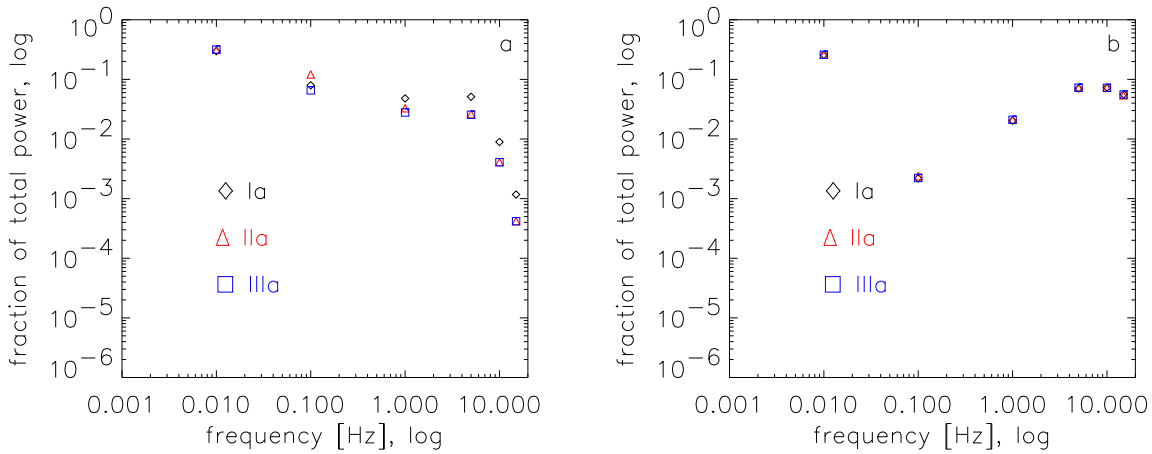

Figure 5.24: Log-log plot of the fraction of total power in frequency ranges [0,0.01], [0.01,0.1], [0.1,1], [1,5], [5,10], [10,15] Hz for a) displacement and b) velocities.

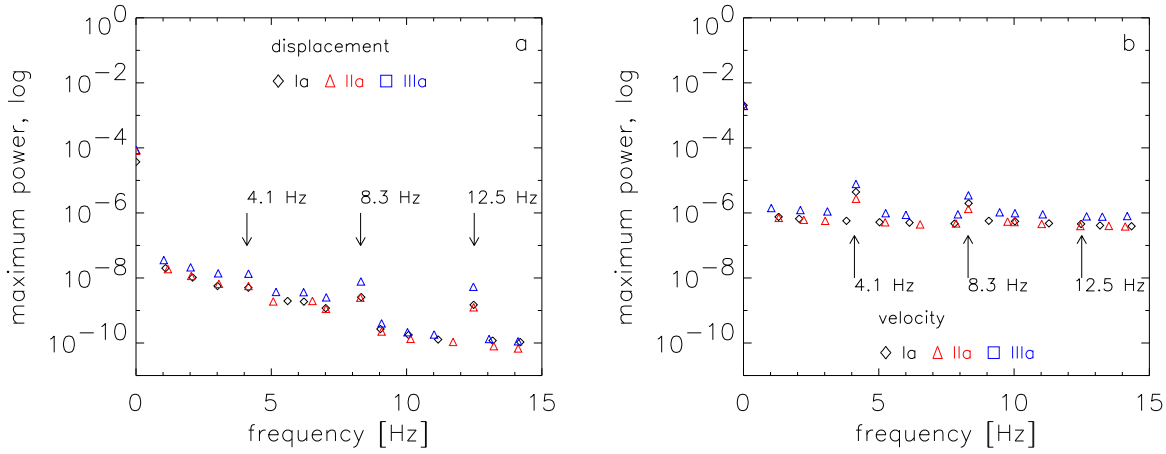

Figure 5.25: Maximum values of power in frequency intervals of 1 Hz from 0 to 15 Hz for a) displacement and b) velocities. Marked are the peaks detected before the detrending.

5.3 Stationarity of the Single Particle Time Series

The data was examined on global trends in chapter 5.2.1. These were removed from the data in chapter 5.2.2. But only common motions of all particles were investigated. Now we have obtained time series of displacements r and velocities v for each single particle. Since these will be used for further investigation in spite of the averaged values, the stationarity of the particular time series is of interest here. Sure any artefact of trends identified should show up here, but the quantity of nonstationarities in these time series is of interest for the interpretation of later results.

An examination of running quantities for each particle is possible but difficult to present for more than 100 particles and three data sets. A qualitative picture of the situation can be obtained as follows. For each particle i running mean and running standard deviation are calculated for $r_i(t)$ and $v_i(t)$ for two windows which cover the first and last half of its whole trajectory length, respectively. The consecutive values with indices 1 and 2 are now plotted against each other (figures 5.26 and 5.28). If they are equal for all particles in certain limits, the resulting points (one point per particle) should accumulate at one spot on the bisecting line. The more the values deviate from this line, the more they differ. A high difference is caused by larger changes in the quantities. The spreading of points in the plane should lie within the statistical and experimental errors. Also the values for different particles should not deviate much, since similar averages of velocities and displacements for the single particles are expected if no disturbing influences act on parts of the crystal. Since this test is done with two windows only, it does not prove or disprove stationarity, but it shows, if at least no long time drifts seems to exist.

To set the a limit for the significance of a deviation of the running mean and standard deviation between both windows the error of these quantities has been estimated for each single particle as

$$\begin{aligned} \delta\overline{r}_{1,2} &= \sqrt{\delta r^2 + (\sigma_{r,1,2}/\sqrt{N_w})^2} \\ \delta\sigma_{r,1,2} &= \sqrt{\delta r^2 + (\sigma_{r,1,2}/\sqrt{2(N_w-1)})^2} \end{aligned} \tag{5.40}$$

. The particle time series are called stationary, if

$$\begin{aligned} \Sigma &= |\overline{r}_2 - \overline{r}_1| - \sqrt{\delta\overline{r}_1^2 + \delta\overline{r}_1^2} \leq 0 \\ \text{resp.} \quad \Sigma &= |\sigma_{r,1} - \sigma_{r,2}| - \sqrt{\delta\sigma_{r,1}^2 + \delta\sigma_{r,2}^2} \leq 0 \end{aligned} \tag{5.41}$$

Figures 5.27 and 5.3 show Σ versus the radius of a particle to the center of rotation. The numbers of particles with $\Sigma > 0$ and $\Sigma \leq 0$ respectively deviation from the bisecting line larger and smaller than the error are plotted in the images. Except from the running standard deviation of data set Ia more or at least half the particles deviate more than required in $\overline{r}$ and in σ_r respectively. With the velocities the ideal case applies: both running quantities differ far less than the error.

Thus one can conclude, that the particle velocities should be stationary within the errors while the displacements still have nonstationary components. This are very likely the fluctuations which could be seen in the plots of the averaged running quantities (figure 5.20). It should be expected that the nonstationarity will affect the results of the tests for ergodicity. The reasons could either be trends not identified yet due to the lack of a theoretical model, or artefacts of trends in the case of an insufficient remove. But the nonstationarity could also be a real property of the intrinsic dynamics of the system.

In the next chapter the time series of displacements and velocities of single particles will be examined with respect to dynamical properties such as temperature and oscillations under the influence of the interparticle potential.

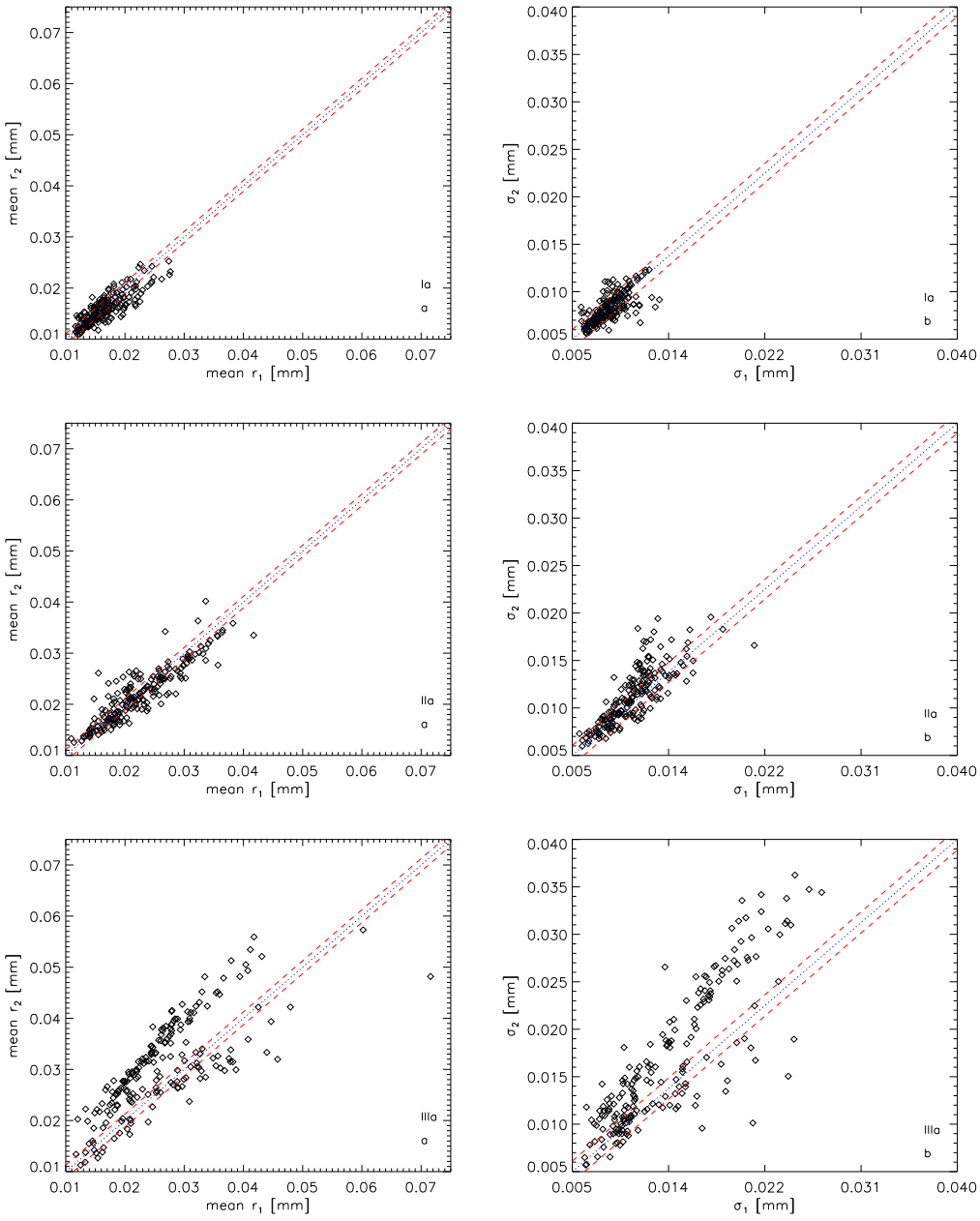

Figure 5.26: Displacement: running mean $\overline{r}_{i,2}$ vs. $\overline{r}_{i,1}$ for each particle in a data set (left) and running standard deviation $\sigma_{r,i,2}$ vs. $\sigma_{r,i,1}$ (right).

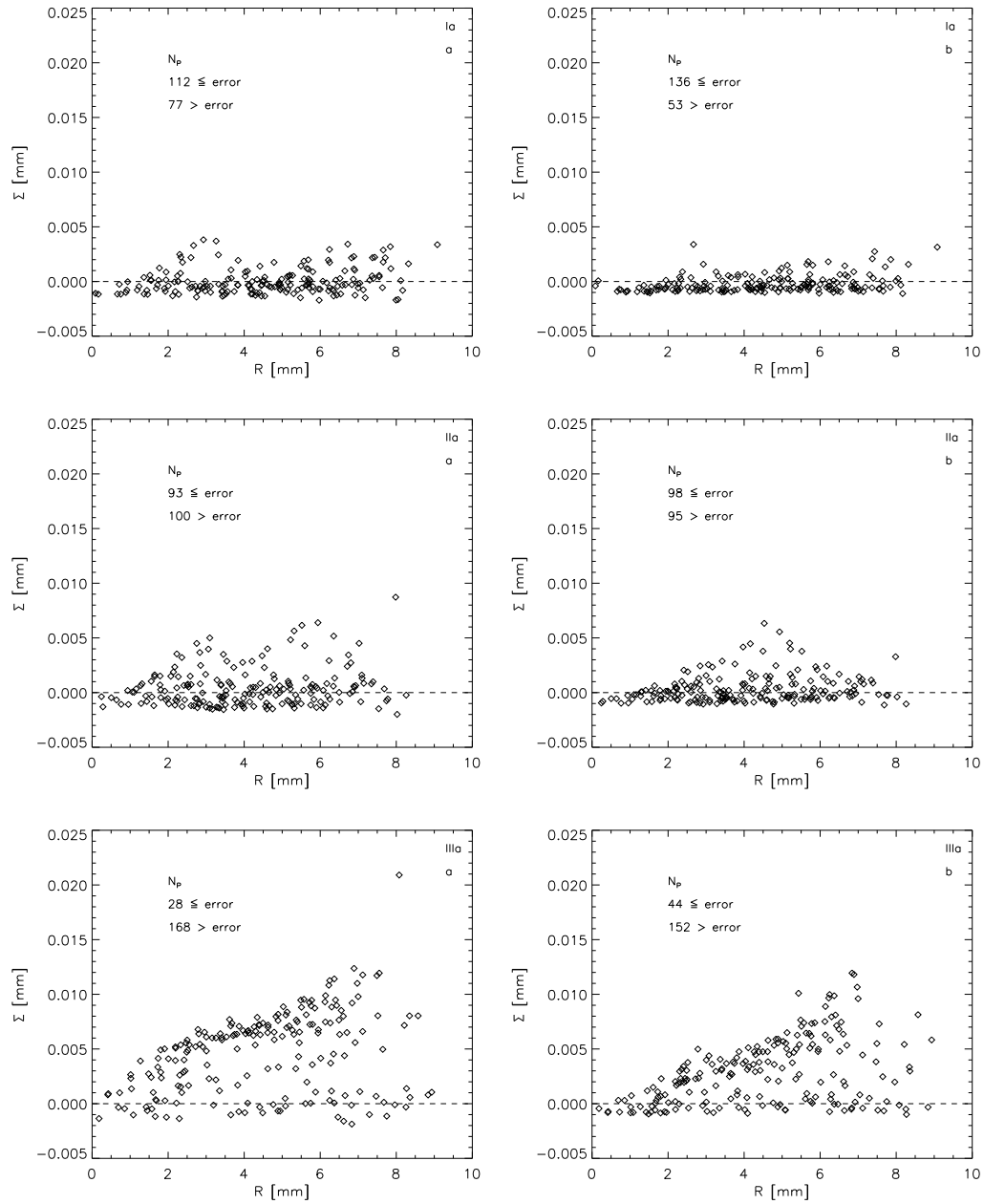

Figure 5.27: Σ vs. R as a measure for the deviation of a) running mean $\overline{r}_{i,2}$ vs. $\overline{r}_{i,1}$ (left) and b) running standard deviation $\sigma_{r,i,2}$ vs. $\sigma_{r,i,1}$ (right). $\Sigma < 0$ indicates deviations smaller than the error.

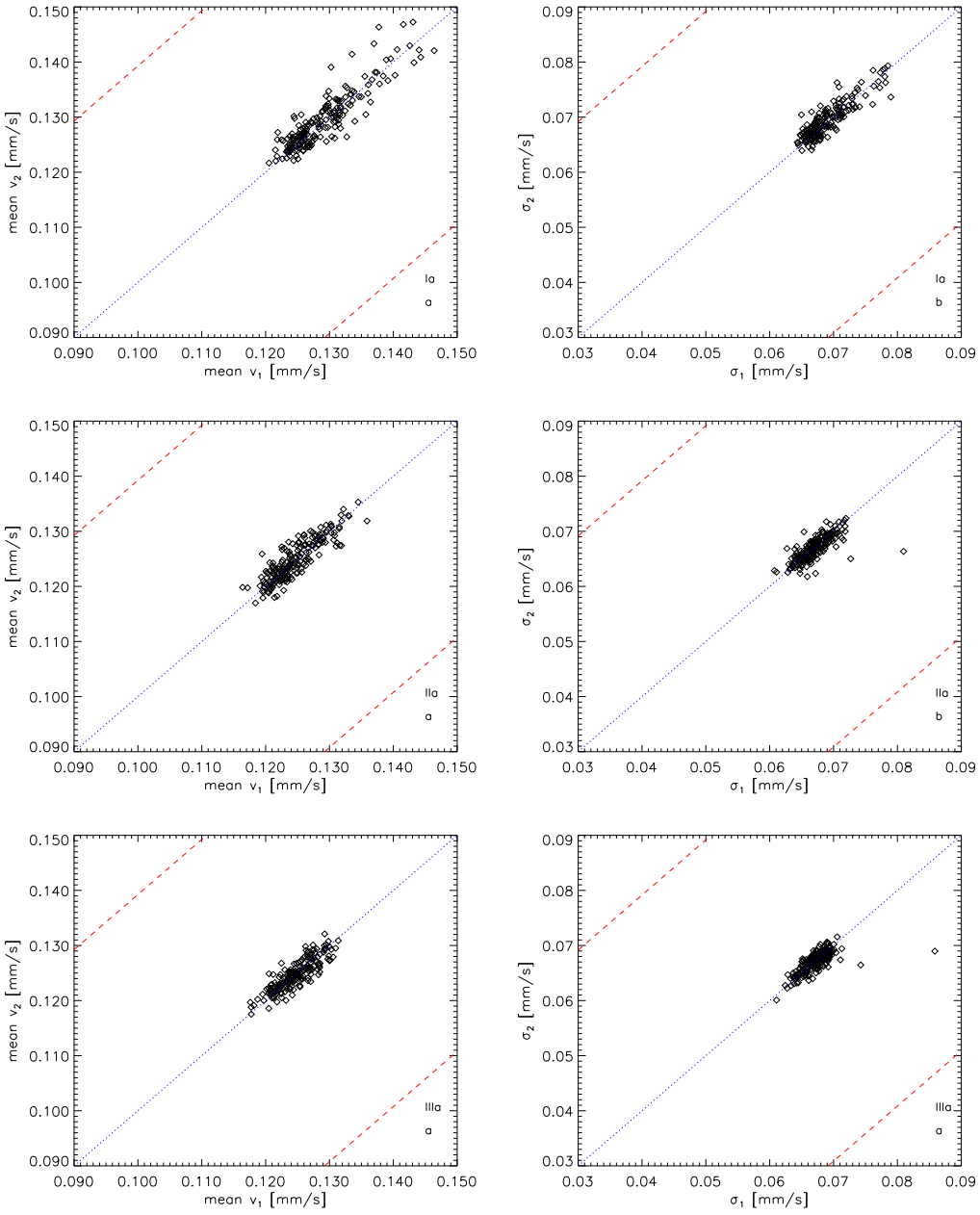

Figure 5.28: Velocity: running mean $\overline{v}_{i,2}$ vs. $\overline{v}_{i,1}$ for each particle in a data set (left) and running standard deviation $\sigma_{v,i,2}$ vs. $\sigma_{v,i,1}$ (right).

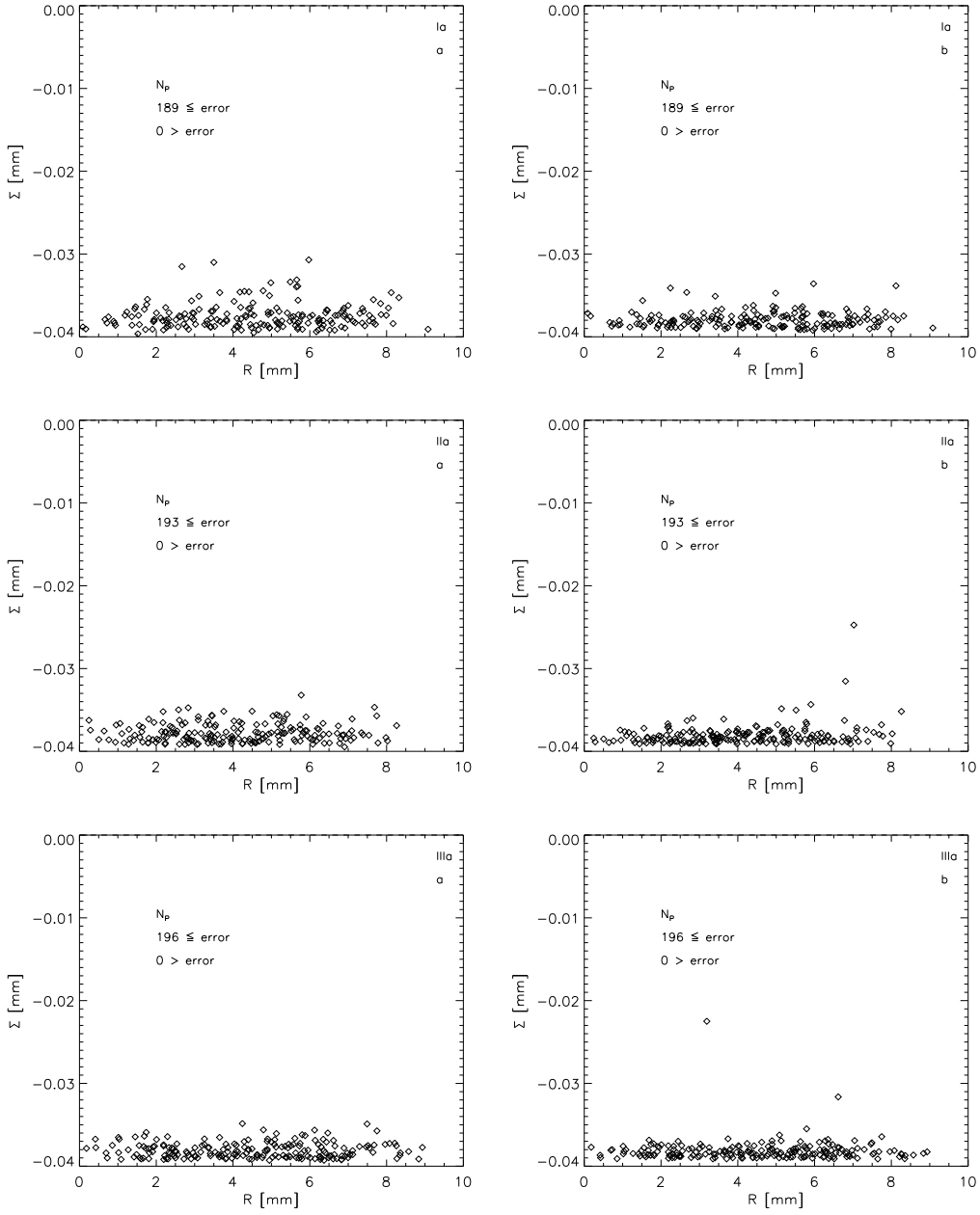

Σ vs. R as a measure for the deviation of a) running mean $\overline{v}_{i,2}$ vs. $\overline{v}_{i,1}$ (left) and b) running standard deviation $\sigma_{v,i,2}$ vs. $\sigma_{v,i,1}$ (right). $\Sigma < 0$ indicates deviations smaller than the error.

5.4 Dynamical Behaviour of Single Particles

5.4.1 Maxwell Distribution of Velocities

The velocity was assumed to follow a Maxwellian distribution. Here a short derivation of this distribution is given. A particle in one dimension with coordinate x, velocity v_x and energy $E_{tot}(x, v_v) = E_{kin}(v_v) + E_{pot}(x)$ can be described by a probability function $F(x, v_x)$ in phase space.

$$\begin{aligned} F(x, v_x) &= \frac{e^{-E_{tot}(x,v_x)/(k_B T)}}{\int_{-\infty}^{+\infty}\int_{-\infty}^{+\infty} e^{-E_{tot}(x,v_x)/(k_B T)} dx dv_x} \\ &= \frac{e^{-E_{kin}(v_x)/k_B T}}{\int_{-\infty}^{+\infty} e^{-E_{kin}(v_x)/(k_B T)} dv_x} \cdot \frac{e^{-E_{pot}(x)/k_B T}}{\int_{-\infty}^{+\infty} e^{-E_{pot}(x)/(k_B T)} dx} \end{aligned} \tag{5.42}$$

with the thermal energy $k_B T$. Equation (5.42) is the probability function of the canonical ensemble for a system in contact with a heat reservoir, normalised by the total phase space volume [22]. To get the probability function for the velocity, $F_{M1}(v_x)$, equation (5.42) is integrated over all coordinates:

$$F_{M1}(v_x) = \int_{-\infty}^{+\infty} F(x, v_x) dx = \frac{e^{-E_{kin}(v_x)/k_B T}}{\int_{-\infty}^{+\infty} e^{-E_{kin}(v_x)/(k_B T)} dv_x} \tag{5.43}$$

E_{kin} depends on v_x only, and the second term in equation (5.42) cancels out. Therefore the probability distribution for the velocities is not dependent on the position x. The integral in the denominator is a normalisation constant. For $E_{kin}(v) = 1/2 \cdot M_P v_x^2$ (M_P: mass) it has the value $\sqrt{2\pi k_B T / M_P}$. The Maxwellian velocity distribution for one dimension is thus:

$$F_{M1}(v_x) = \frac{1}{\sqrt{2\pi k_B T / M_P}} \cdot e^{-\frac{v_x^2}{2k_B T/M_P}} \qquad \text{1D Maxwell distribution} \tag{5.44}$$

This is a Gaussian probability distribution with

$$\begin{aligned} \text{mean} \qquad & \overline{v}_x = 0 \\ \text{and standard deviation} \qquad & \sigma_{v_x} = \sqrt{k_B T / M_P} \end{aligned} \tag{5.45}$$

If the system is 2-dimensional with coordinates x, y and independent velocity components v_x, v_y which are both described as above, the probability of the velocity $\mathbf{v} = \binom{v_x}{v_y}$, that means the probability to have a certain v_x and a certain v_y, is the product of the single probabilities $F(v_x)$ and $F(v_y)$:

$$\mathrm{F}(\mathbf{v}) = F_{M1}(v_x) \cdot F_{M1}(v_y) = \frac{1}{2\pi\sigma_v^2} \cdot e^{-\frac{v_x^2 + v_y^2}{2\sigma_v^2}} \tag{5.46}$$

The standard deviation depends on temperature and mass only and is the same for v_x and v_y. It is written as $\sigma_v = \sigma_{v_x} = \sigma_{v_y}$ now.
The probability of the absolute velocity $v = \sqrt{v_x^2 + v_y^2}$ is larger than for $\mathbf{v}$, because the same value of v can be obtained by a lot of combinations of v_x, v_y. Therefore $\mathrm{F}(\mathbf{v})$ multiplied by the surface $2\pi v$ in the 2-dimensional velocity phase space yields the probability distribution of the absolute velocity:

$$F_{M2}(v) = 2\pi v \cdot \mathrm{F}(\mathbf{v}) = \frac{v}{\sigma_v^2} \cdot e^{-\frac{v^2}{2\sigma_v^2}} \qquad \text{2D Maxwell distribution} \tag{5.47}$$

The Maxwell distribution depends on the mass M_P and the temperature T only. Some useful relations for a 2-dimensional Maxwellian velocity distribution are:

$$\overline{v}_x = \overline{v}_y = 0 \tag{5.48}$$

$$\overline{v_x^2} = \overline{v_y^2} = \frac{1}{2}\frac{k_B T}{M_P} \tag{5.49}$$

$$\sigma_v = \sqrt{\frac{k_B T}{M_P}} \tag{5.50}$$

$$\overline{v} = \int_0^\infty v \cdot F_{M2}(v) dv = \sqrt{\frac{\pi}{2}}\left(\frac{k_B T}{M_P}\right) \tag{5.51}$$

$$\overline{v^2} = \int_0^\infty v^2 \cdot F_{M2}(v) dv = 2 \cdot \frac{k_B T}{M_P} \tag{5.52}$$

The last relation is also following from the equipartition theorem [21].

5.4.2 Velocity Distributions in the Plasma Crystal

The velocity probability distributions F_{M1} and F_{M2} have been obtained for the velocities in x and y direction and for the absolute velocity $v_i(t)$ for each particle i by making histograms. 1- and 2-dimensional Maxwell distributions have been fitted to each histogram with σ_v as fit parameter. The goodness of fit is given by the reduced χ_ν^2 calculated between fit and histogram. As an example for one particle the histograms (normalized to unit area) and the Maxwellian fits are shown in figure 5.29. The χ_ν^2 are not plotted explicitely, but graphic 5.30 shows the maximum values obtained for velocity components v_x, v_y and for v of each data set and the respective mean value of χ_ν^2 averaged over all particles. The average values of the χ_ν^2 look reasonable good to accept the Maxwellian fits as a valid model for the distributions of velocities, since they are of the magnitude of 1 and do not reach 2 in the maximum.

By recapitulating the definition of the Maxwell distribution, it is described solely by particle mass and temperature. Also, the temperatures should not differ for v_x, v_y and v. The temperatures, or kinetic energies $k_B T$, are now calculated for each particles velocity time series directly from the data by using the relations for the mean squared velocities

$\overline{v_x^2}$, $\overline{v_y^2}$ and $\overline{v^2}$ (equations (5.49) and (5.52)) for the mean squared values, and again with the relation for the standard deviations which were obtained as the fit parameters. The result is shown in figures 5.31 to 5.33 for the three data sets. The temperature is plotted versus the radial particle position R with respect to the rotation center to detect possible dependencies from the position within the crystal. A linear fit to $k_B T(R)$ has been made for the velocity components and the absolute velocity and is plotted over the temperature distribution.

Two things can be seen: The kinetic energies of the velocity components are located around 0.04 eV ($\hat{=}$ 464 K), which is much higher than room temperature ($\hat{=}$ 0.026 eV) and there is indeed a radial dependence of the temperature. The gradients of the fit are shown in figure 5.34. The temperature decreases with increasing radius while it is nearly constant for the different peak-to-peak voltages.

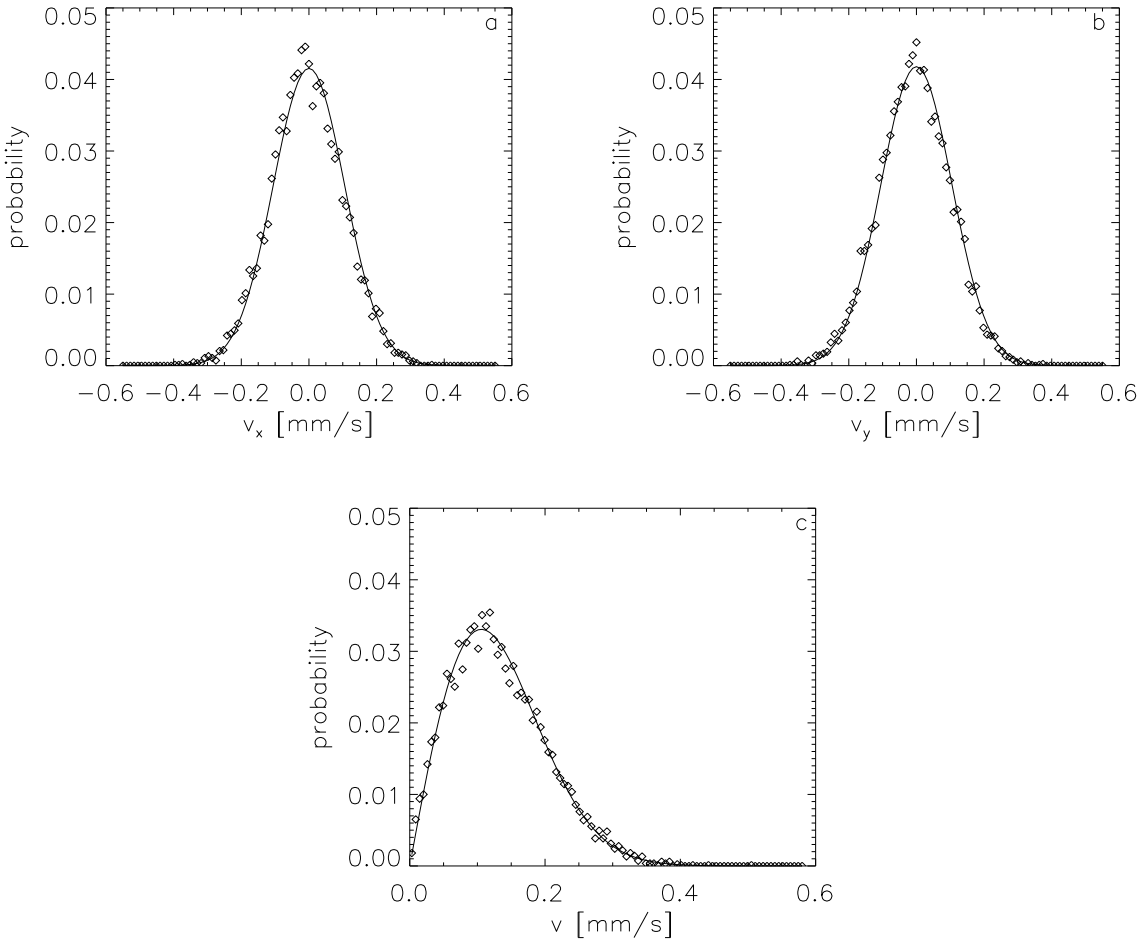

Figure 5.29: Histogram of velocities v_x (upper left), v_y (upper right) and v (below) of one particle (diamonds) and Maxwellian fit (solid line). The dashed line is the distribution of measurement errors.

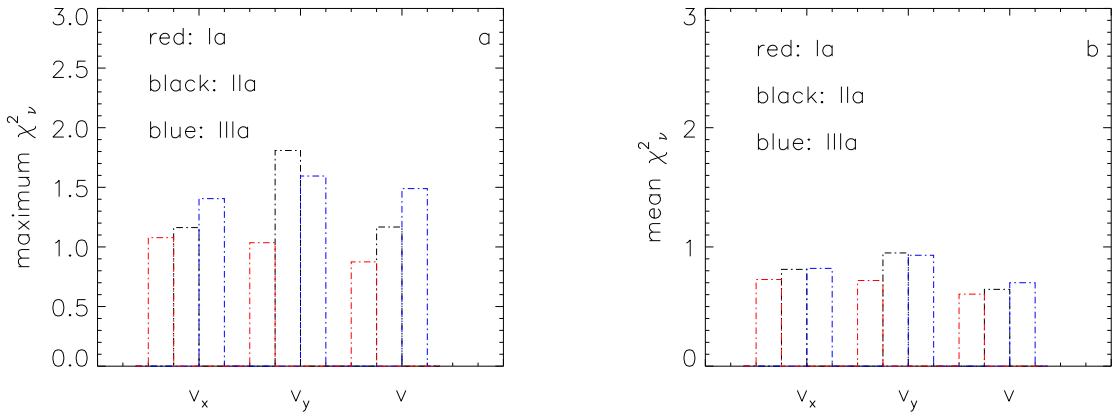

Figure 5.30: a) Maximum χ^2_ν and b) mean χ^2_ν of v_x, v_y and v v for data sets Ia, IIa and IIIa.

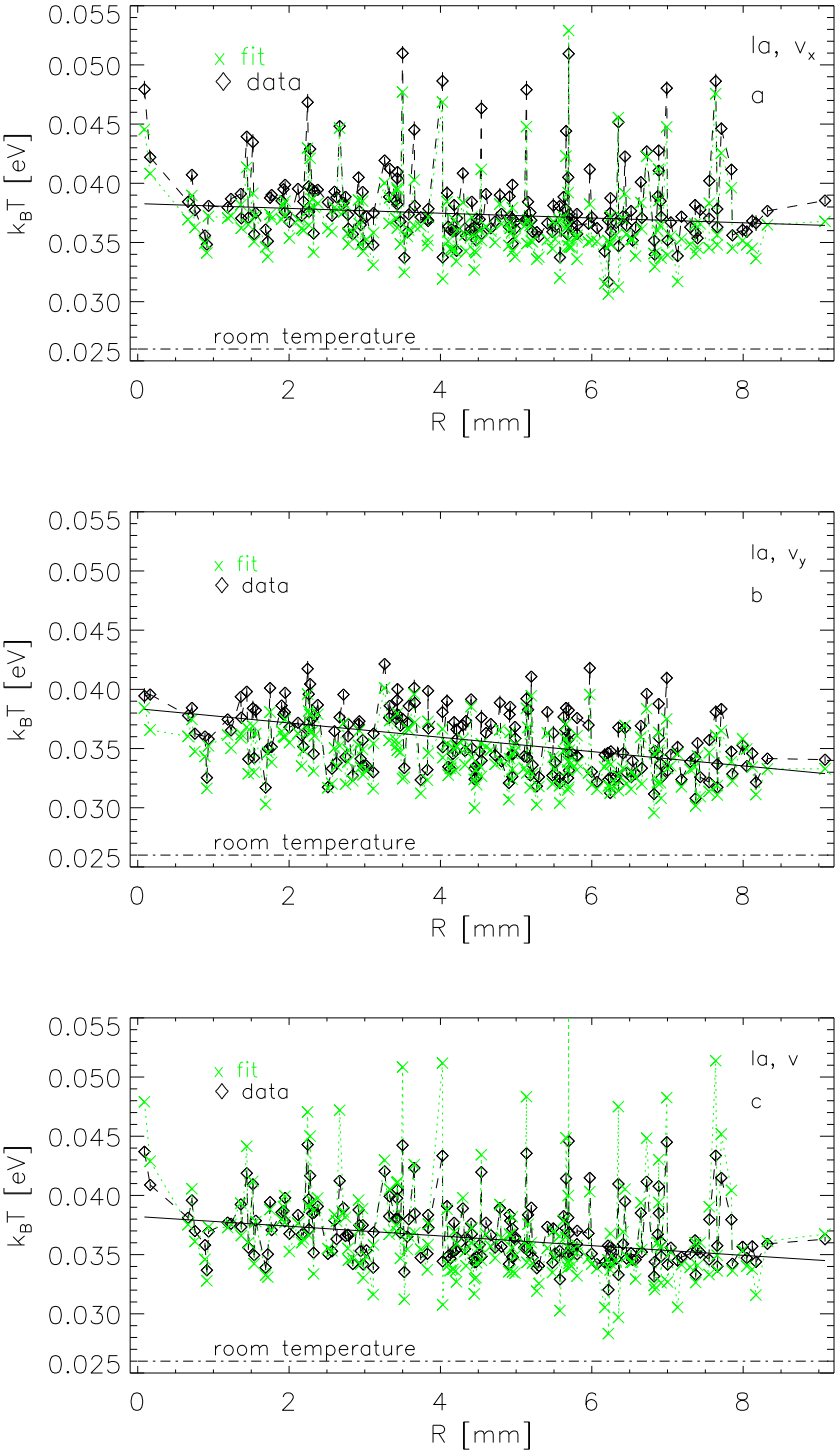

Figure 5.31: Data set Ia: Kinetic energy k_BT versus radial position R for v_x, v_y and v. The red, dotted lines correspond to the values obtained from the Maxwellian fit.

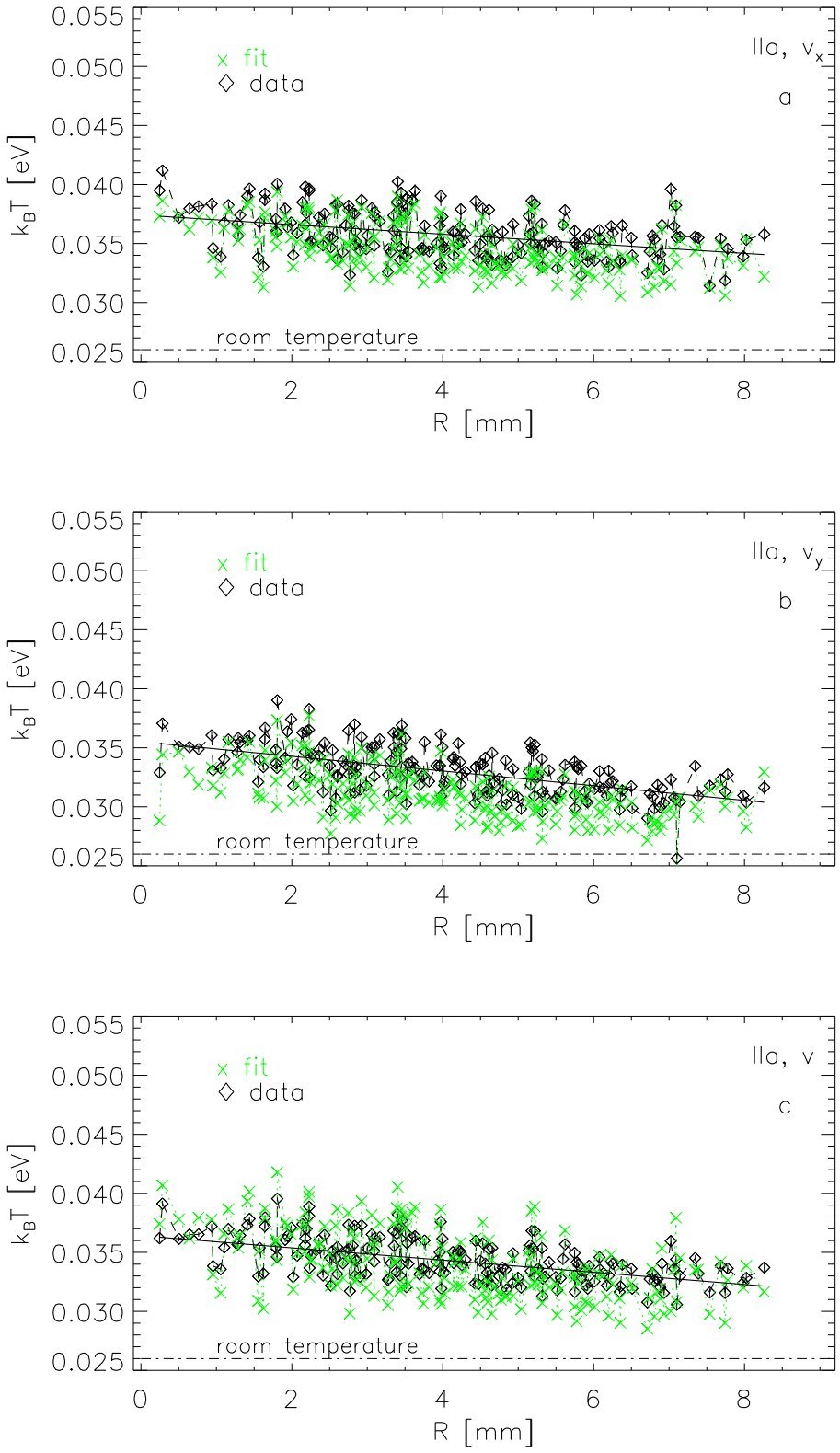

Figure 5.32: Data set IIa: Kinetic energy k_BT versus radial position R for v_x, v_y and v. The red, dotted lines correspond to the values obtained from the Maxwellian fit.

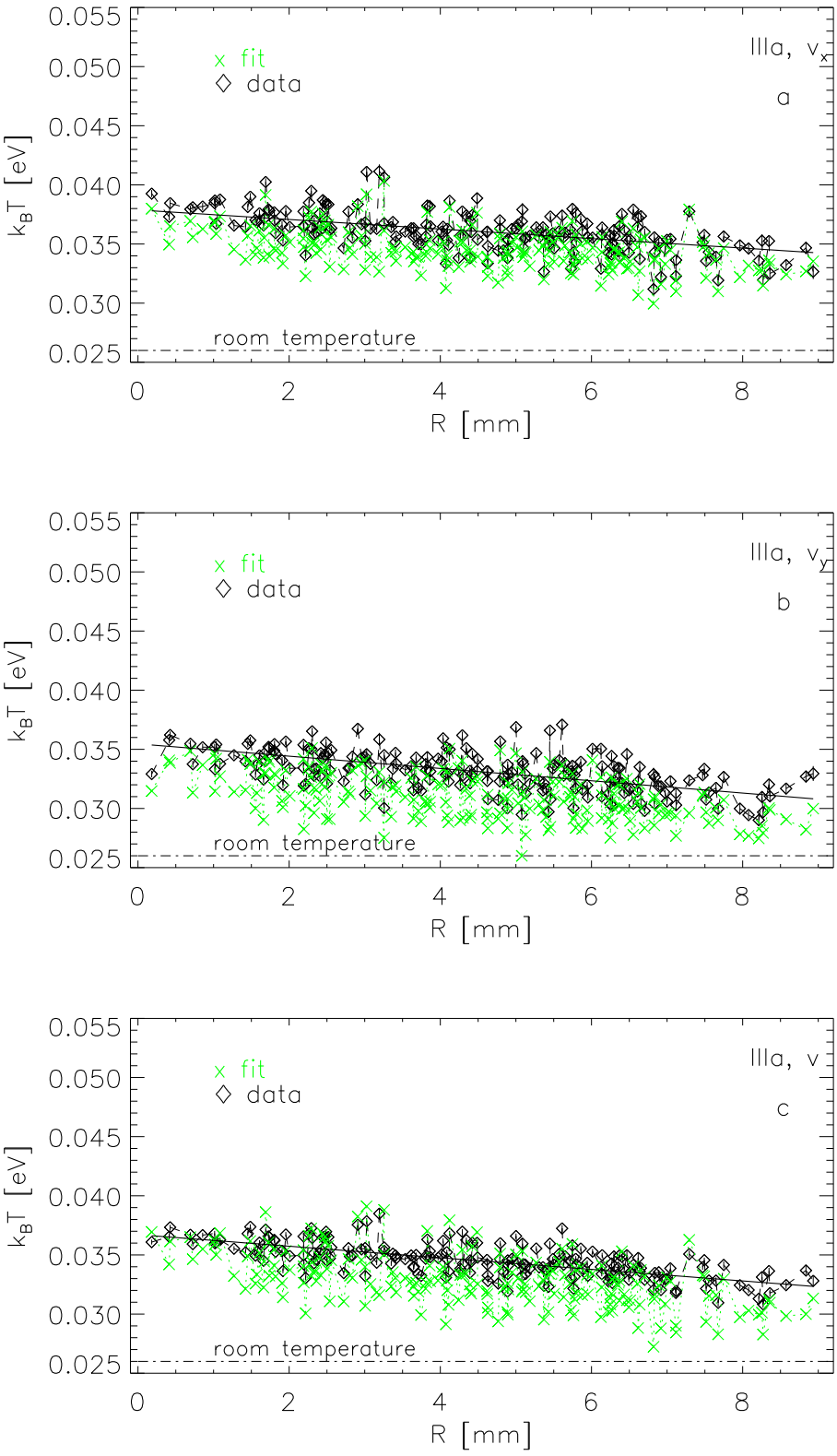

Figure 5.33: Data set IIIa: Kinetic energy k_BT versus radial position R for v_x, v_y and v. The red, dotted lines correspond to the values obtained from the Maxwellian fit.

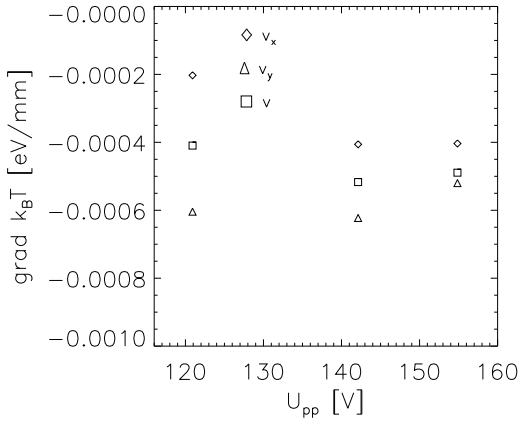

Figure 5.34: Gradient of linear fit to $k_BT(R)$ vs. U_{pp}

5.4.3 Distribution of the Displacement

The distribution of displacements r is determined mainly by the interparticle potential Φ_{IP}. An approximative theoretical derivation of the expected probability distribution is given here, starting with the 1-dimensional distribution of the coordinates $\tilde{x}$ and $\tilde{y}$, considering $\tilde{x}$ as example. $\tilde{x}$ and $\tilde{y}$ are the coordinates relative to the mean lattice site here, not the coordinates of a particle in the crystal. From this a model for the distribution of r is estimated. The normalisation constants will be associated with physical variables of the system.
As the Maxwell distribution of velocities is derived by the integration of the probability function $F(\tilde{x}, v_{\tilde{x}})$ in equation (5.42) over $d\tilde{x}$, the distribution $F_{D1}(\tilde{x})$ of $\tilde{x}$ is obtained by integrating (5.42) over $dv_{\tilde{x}}$. If the potential energy is independent of the velocities, as in our case, the terms with E_{kin} cancel out. Thus

$$F_{D1}(\tilde{x}) = \int_{-\infty}^{+\infty} F(\tilde{x}, v_{\tilde{x}}) dv_{\tilde{x}} = \frac{e^{-E_{pot}(\tilde{x})/(k_B T)}}{\int_{-\infty}^{+\infty} e^{-E_{pot}(\tilde{x})/(k_B T)} d\tilde{x}} \tag{5.53}$$

The integral in the denominator gives a normalisation constant. To solve it again the consideration of a linear chain of particles is used and the interparticle potential is expanded into a Taylor series to the second order. Then the change of the potential energy can be written as in equation (4.28)

$$\begin{aligned} \Delta E_{pot}(\tilde{x}) &= Q_P \Phi_{IP}(\Delta) \left(\left(\frac{\Delta + \lambda_D}{\Delta \lambda_D} \right)^2 + \frac{1}{\Delta^2} \right) \cdot \tilde{x}^2 \\ &= Q_P \Phi_{IP}(\Delta) \frac{1}{\Delta^3} (2 + 2\kappa + 2\kappa^2) \cdot \tilde{x}^2 \\ &= \frac{1}{2} k \tilde{x}^2 \end{aligned} \tag{5.54}$$

Here $\kappa = \Delta / \lambda_D$ and the definition of the spring constant k from equation (5.7) have been used. ΔE_{pot} is the quantity which destines the distributions of positions $\tilde{x}$, since the particle prefers directions of motion where the gradient of energy decreases. Solving the integral in the equation (5.53) with ΔE_{pot} yields for the normalisation constant

$$\frac{1}{\int_{-\infty}^{+\infty} \exp(-\Delta E_{pot}(\tilde{x})/(k_B T)) d\tilde{x}} = \frac{1}{2 \int_0^{+\infty} \exp(-\frac{1}{2} k \tilde{x}^2/(k_B T)) d\tilde{x}} = \frac{1}{\sqrt{2\pi}} \frac{1}{\sqrt{k_B T/k}} \tag{5.55}$$

and thus for $F_{D1}(\tilde{x})$:

$$F_{D1}(\tilde{x}) = \frac{1}{\sqrt{2\pi}} \frac{1}{\sqrt{k_B T/k}} e^{-\frac{1}{2} \frac{\tilde{x}^2}{k_B T/k}} \tag{5.56}$$

The same holds for the distribution of $\tilde{y}$. F_{D1} is a Gaussian distribution with mean zero and standard deviation $\sigma_{\tilde{x}} = \sigma_{\tilde{y}} = \frac{k_B T}{k}$.
The displacement r is derived from $\tilde{x}$ and $\tilde{y}$ as the square root $\sqrt{\tilde{x}^2 + \tilde{y}^2}$. Therefore for

independent $\tilde{x}$ and $\tilde{y}$ the probability function $F_{D2}(r)$ of the absolute displacement r is obtained by multiplying $F_{D1(\tilde{x})}$ with $F_{D1}(\tilde{y})$ and the volume $2\pi r$ of the phase space of r as it was done for the distribution of the absolute velocity.

$$F_{D2}(r) = F_{D1}(\tilde{x}) \cdot F_{D1}(\tilde{y}) \cdot 2\pi r = \frac{r}{k_B T/k} e^{-\frac{1}{2}\frac{r^2}{k_B T/k}} \tag{5.57}$$

The measured distributions for $\tilde{x}_i$, $\tilde{y}_i$ and r_i for the particular particles i are obtained as histograms from the data. $F_{D1}(\tilde{x}_i(t))$, $F_{D1}(\tilde{y}_i(t))$ and $F_{D2}(r_i(t))$ are then fitted to the histograms with $\sqrt{k_B T/k}$ as fit parameter. As an example, the histograms normalized to unit area found for one particle are displayed in figure 5.35. The goodness of the fits is tested again by the χ^2_ν and illustrated in terms of the maximum and the average χ^2_{nu} in graphic 5.36.

While the maxima of χ^2_ν are located around 30 for r and all data sets, the average exceeds 1 by a factor of 2 respectively even 10 for data set IIIa, so the validity of the fits are to be doubted.
The reason is on the one hand the model choosen for the distribution, which considered only small and linear deviations r from the mean lattice site in a chain of particles. The fact was ignored a particle is under the influence of approximately six neighboring particles in a hexagonal structure.
Further the detrending was not perfect for r, thus the shape of the distributions could still be influenced by remains of global motions in the crystal. Especially data set IIIa seems to diverge.

To demonstrate this, the histograms of r for all particles are plotted on top of each other as point distributions in panel 5.37. For a correct model and equal conditions for the particles in the crystal one would assume that all points are located around one distribution F_{D2} with a spreading due to statistical reasons or small irregularities. In the image a broad variation of distributions is found. The spreading increases with peak-to-peak voltage (from top to bottom in figure 5.37). To get an idea of the origin of the differences, the particles are divided in two or three groups as indicated by the colors red, blue and green on the left side of panel 5.37. Particles with a maximum ≥ 0.04 are assigned to the 'red' particles, if the maximum is ≤ 0.04 they are given the color blue. A theoretical average distribution for the colors red and blue is overplotted as a black line to illustrate the difference. For data set IIIa a third color (green) was needed for particles whose distributions have two maxima. These are very likely the reason for the bad χ^2 statistic for the fits to this data set. The corresponding particle distributions seem to consist of two nested distributions.

For comparison the corresponding fits found for each particle are displayed on the right hand side as an overlay of all fits of one data set. The change of colors from light blue to red illustrates the increasing maximum of the distribution for different particles. Here one finds a continuous change of the shape of the distributions fitted to the histograms. Though the goodness of fit is in question, it reflects the differences between the particular particles.

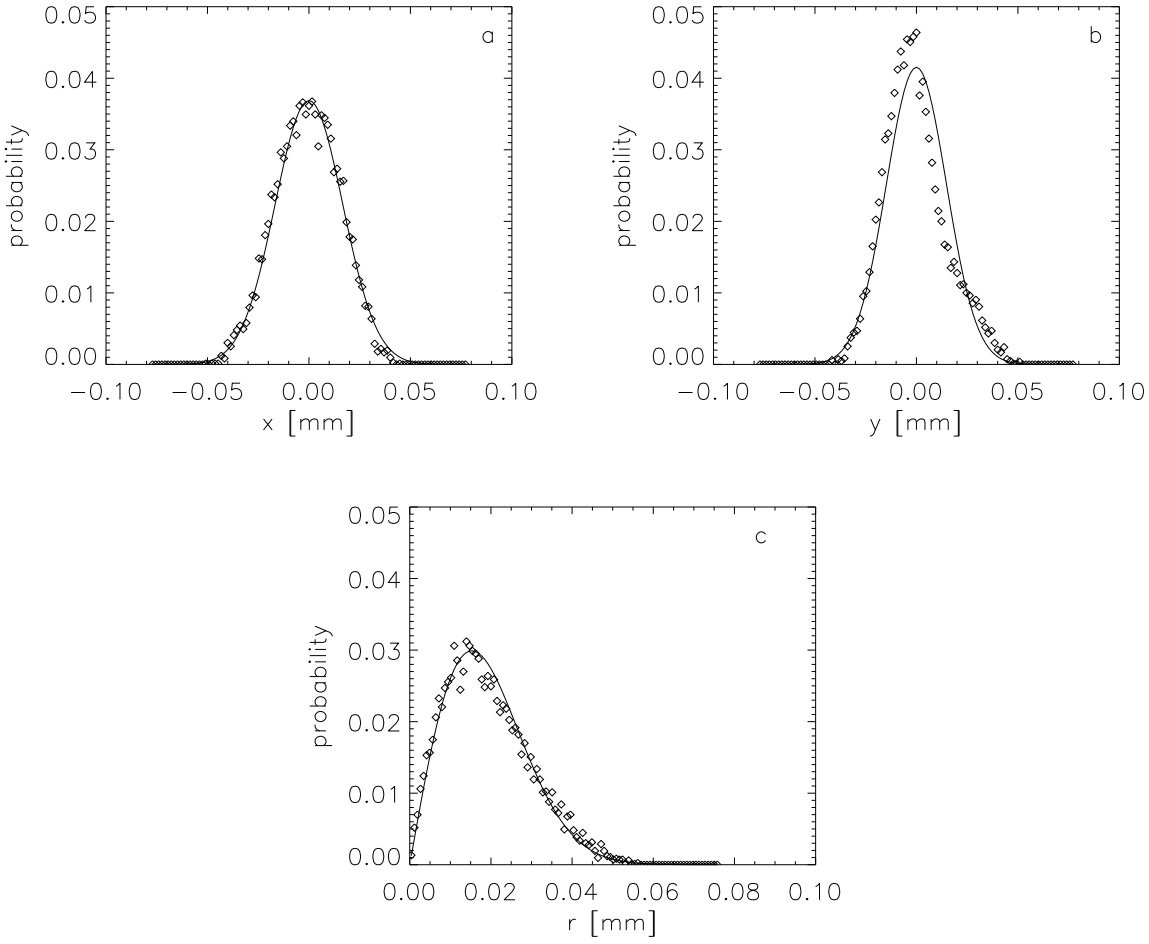

Figure 5.35: Example of the histograms of a) $\tilde{x}$, b) $\tilde{y}$ and c) r for one particle (diamonds), and a fit with F_{D1}, F_{D2} respectively (solid line). The curves are normalized to unit area.

As a final step particles belonging to different groups are identified by the unique numbers they are given during the tracking with respect to their positions in the crystal. In figure 5.38 the positions of all particles in the first frame of a record are marked with the colors as they were introduced for the histograms above. The rotation center is marked by a cross. In each data set the 'red' particles are approximately located around the rotation center, while the 'blue' particles group towards the edges. In data set IIIa the 'green' particles are arranged in a continuous stripe, so a spatial correlation of their irregular behaviour exists. Since the images contain only parts of a larger crystal, it is difficult to say, if the localisation of the groups is symmetrical around the rotation center or if it is connected to the localisation of the crystal in the confinement potential. Surely it will influence the statistical tests where ensembles of particles are compared with trajectories of single particles in time and turns up the question if such a test is reasonable as long as

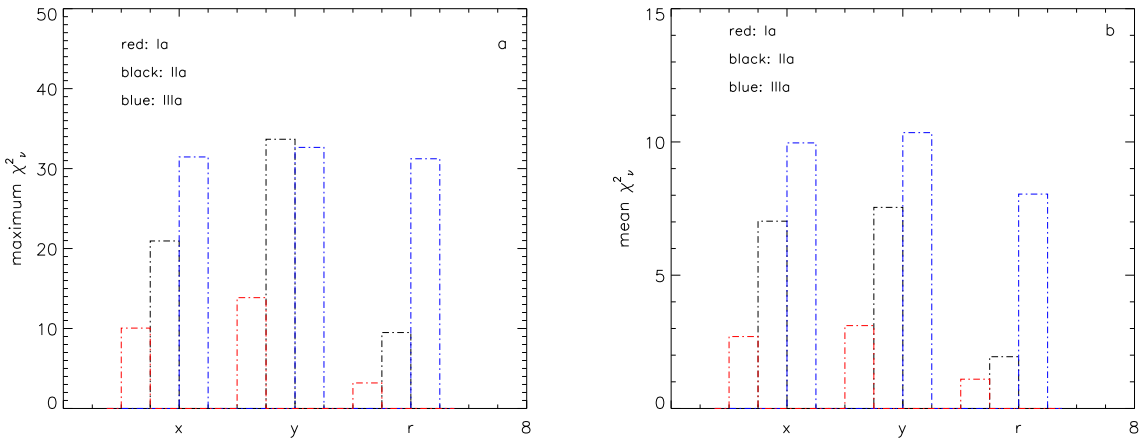

Figure 5.36: a) Maximum χ^2_ν and b) mean χ^2_ν of $\tilde{x}$, $\tilde{y}$ and r for data sets Ia, IIa and IIIa.

the cause for the difference in the particle behaviour is not known.

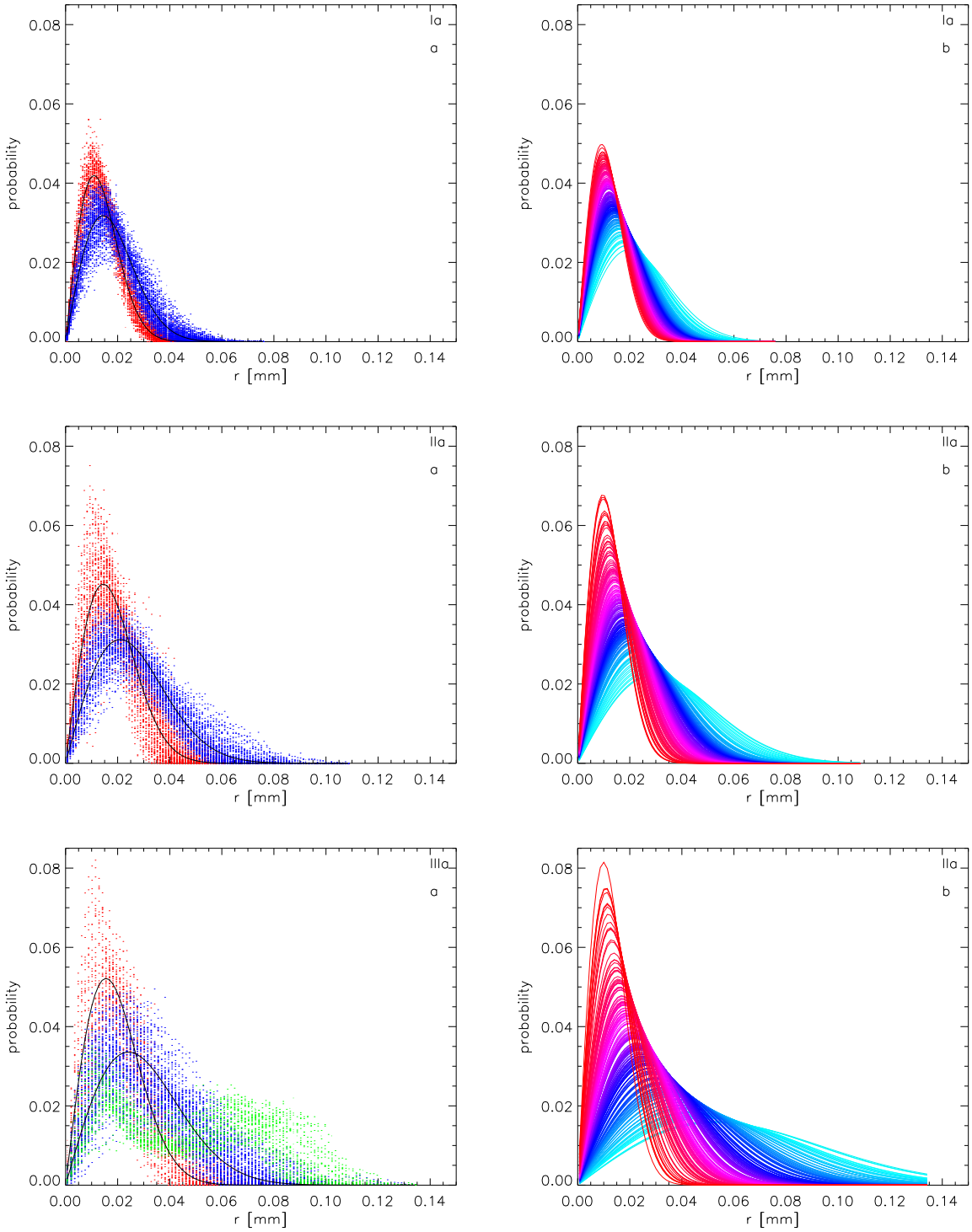

Figure 5.37: a) Normalized histograms of $r_i(t)$ for each particle as an overlay (left side). The black curves indicate a mean distribution for red resp. blue 'particles', b) Corresponding Gaussian fits. The colors from light blue to red indicate the increase of the maximum of $F_{D2}(r_i)$.

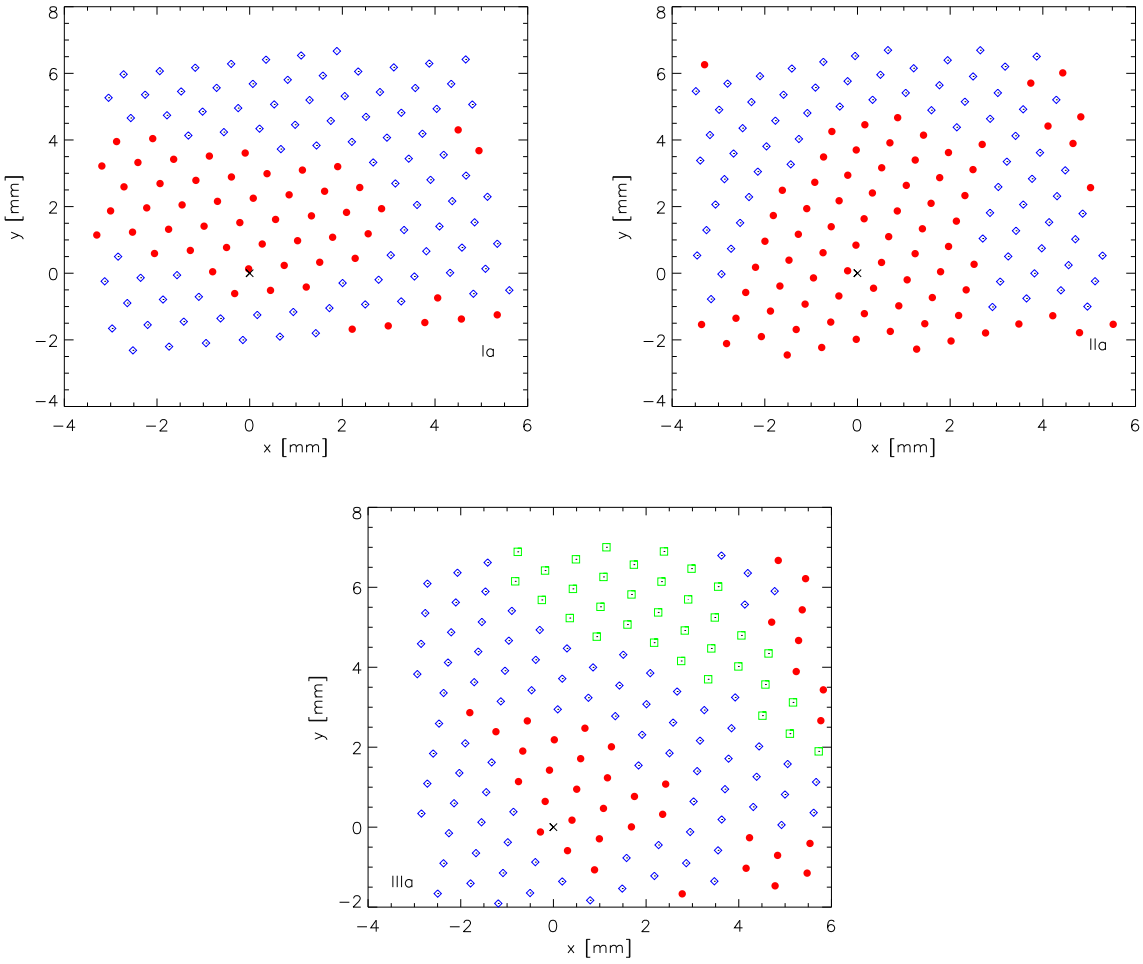

Figure 5.38: Position of all particles in one frame. The cross marks the center of rotation.The colors assign particles to the groups of distributions as it was introduced in figure 5.37.

Though the investigation of the displacement distributions revealed different behaviour of groups of particles connected spatially within the crystal thus contradicting the assumption of the result of equality from the comparison of time and ensemble distributions from the outset, it can be used to estimate a property of the system, namely the Einstein frequency. Remember the spring constant k appearing in the theoretical distribution for r. In chapter 5.1.2.2 it had been connected to k by

$$\omega_E = \sqrt{\frac{k}{M_P}} \tag{5.58}$$

with the particle mass $M_P = 5.5 \cdot 10^{-13}$ kg. Since the kinetic energy $k_B T$ was estimated from the velocity distributions in the last chapter, k and thus ω_E can be derived from the fit parameter $\sqrt{k_B T/k}$ for each particle. The resulting frequency $\nu_E = \omega_E/2\pi$ is displayed in figure 5.40. For comparison with the ν_E estimated in chapter 5.1.2.2 where the charge was an unknown factor, this is plotted again versus ascending particle charges in figure 5.39. The range of charges corresponding to the frequencies estimated from the fit to the displacement distributions is marked by a rectangle.

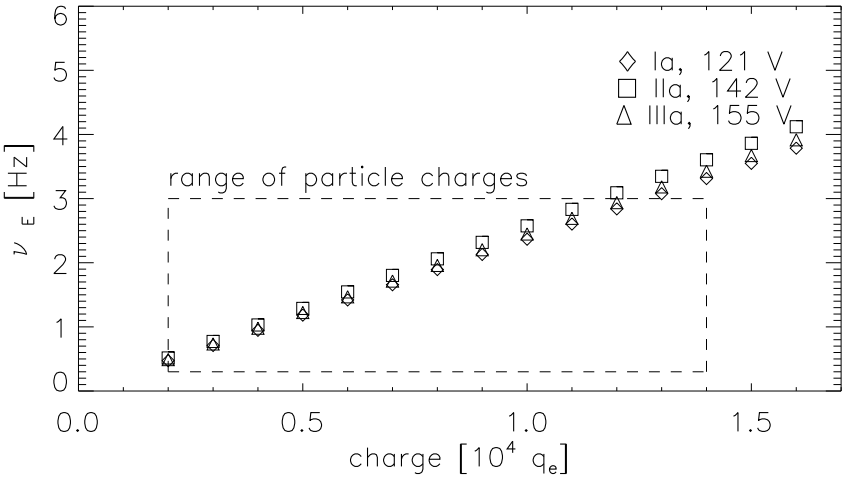

Figure 5.39: ν_E as derived in chapter 5.1.2.2 vs. particle charge. Within the rectangle possible charges are located for the frequencies found from the distributions.

The ν_E show a radial dependence very likely arising from the use of the particle temperatures in the calculation, which also were dependent on R. The estimated frequencies should not be weighed too much, since the goodness of fit was not the ideal case for all particles. Especially for data set IIIa the result might be wrong. By excluding the lowest frequencies originating from that data set, possible particle charges would be in the range of 5000 to 10000 q_e. $Q_P = 5000$ q_e together with $k_B T = 0.04$ eV and $\Delta \approx 0.7$ mm would yield a coupling parameter $\Gamma \approx 19000$ which coincides with the estimation of Γ in chapter 5.1.2.1.

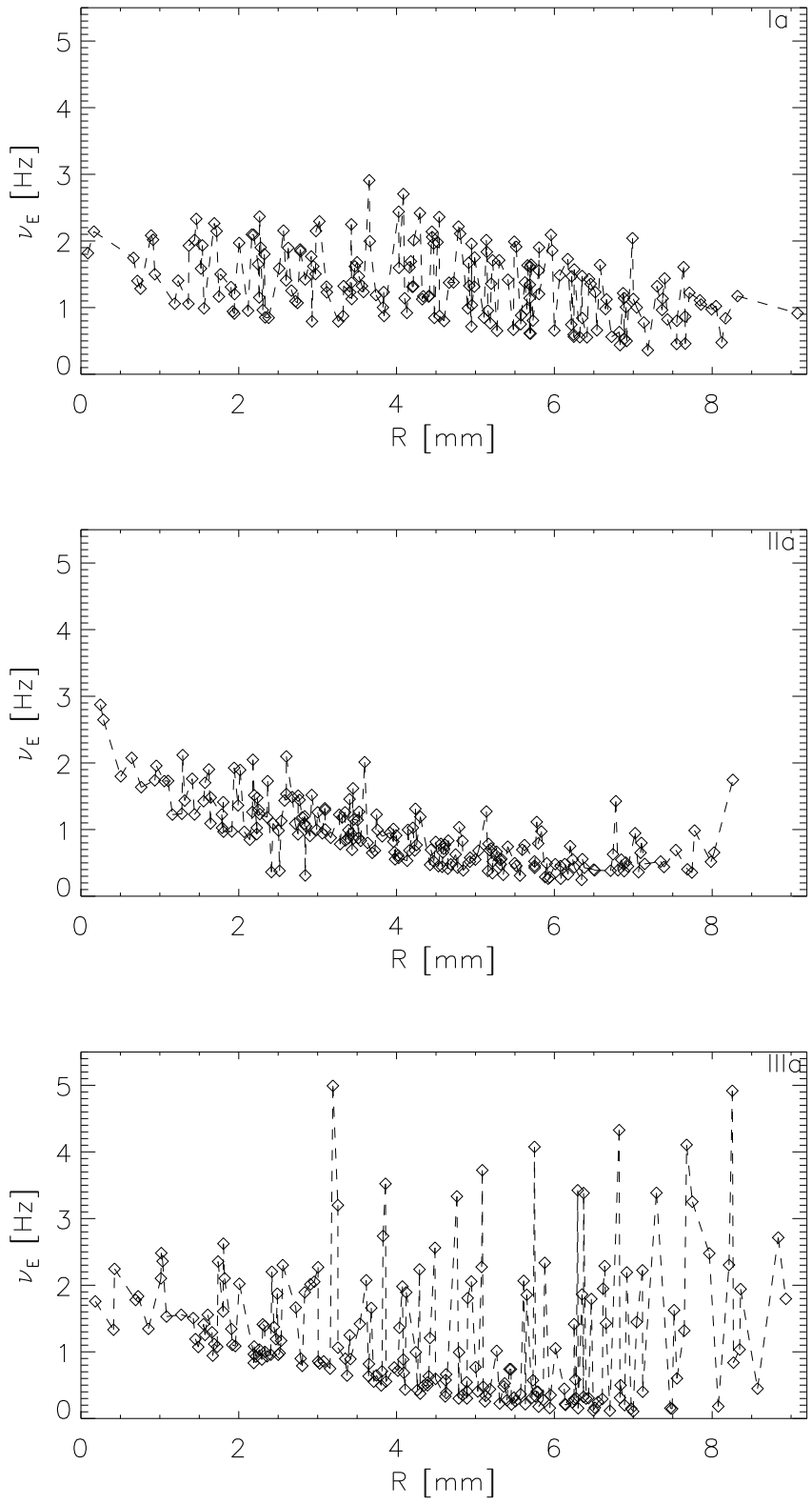

Figure 5.40: ν_E estimated from the fit parameter in $F_{D2}(r_i)$ with the particle velocities from chapter 5.4.2 plotted against radial position R for data sets Ia,IIa and IIIa (from top to bottom).

5.5 Test for Ergodic Behaviour

Ergodic behaviour in a plasma crystal is understood as the equivalence of the dynamic behaviour of a single particle in time and the ensemble of particles as components of the crystal at one particular time. It is often presupposed in the interpretation of particle dynamics. A lot of quantities such as particle temperature, the motion under the influence of the interparticle potential or the charge are derived from series of images taken from a whole crystal by averaging over the ensemble of particles in each image and over time.

It was already pointed out that a plasma crystal is a strongly coupled system. The condition for ergodicity of independent systems in an ensemble thus contradicts with the nature of plasma crystals.

Also the stationarity of the time series of displacements and velocities is a crucial point for ergodic behaviour. In the experiments performed in this thesis, long-time optical observation of a plasma crystal have been recorded. Thus nonstationarities hidden during the usually much shorter measurement times reveal apart from the already known trends innate to the crystal as a whole. This nonstationarities seem to be a property of each particular particle and not a global effect.

Further it had been found in the last chapter that the displacements of particles from their mean lattice site, defined as the average position in time, exhibits distributions completely determined in their shape by the position of the specific particles within the crystal. This dependence could be influenced by the external confining potential, since it was approximately radial symmetric to the rotation center of the crystal, which usually lies at the minimum of the confinement.

The distribution of velocities was found to be Maxwellian, thus determined by particle temperature and mass. The temperature was higher than the neutral gas temperature, and showed a radial dependence as the displacements, though the dependence was smaller by magnitudes here.

The question emerges for the validity of assuming ergodic behaviour in a system which disagrees with conditions implied for ergodicity. This could also be expressed as the question, how an ensemble of particles, of which each can be uniquely identified in phase space by its particular distribution function such as to the displacement, could exhibit anything else than a unique dynamic behaviour linked to that and strictly that particular particle.

However, it will be tested, if the distributions of the displacement $r_j(t_k) = r_{j,k}$ from the mean lattice site $x_{ML,j}, y_{ML,j}$ of all particles $j \in [1, N_k]$ in one frame at the time t_k is the same as the distribution of $r_i(t_n), n \in [1, N_T]$ of one particle i during all frames N_T. This will be done by statistical test methods These will directly compare the differences in the distribution of values of both sets. So no averaging will be done.The same will be investigated for the absolute velocities $v(t)$.

After a refresh of the conditions for ergodic behaviour in section 5.5.1, a short introduction to the principle of statistical tests is given in section 5.5.2. The test statistic used is then

explained in section 5.5.3, while section 5.5.4 summarises the result.

5.5.1 Conditions for Ergodicity

The information obtained for the performed experiments are compared with the conditions of ergodic behaviour listed in chapter 3. The points to take care of are the time scales of dynamics, the question for a closed system and stationarity, and last the condition of independent realisations.

That a plasma crystal is not a closed system is known, but it was mentioned that a constant particle energy would be enough to treat the particles as closed systems. In chapter 5.4.2 the particle velocities were described by Maxwellian distribution functions with a constant temperature, so the kinetic energy is assumed to be constant. The potential energy is connected to the particle charge and the confinement strength, which is given by the external power source. All parameters were kept constant during experiments, and the segments of trajectories affected by power fluctuations were cut out. The particle charge depends mainly on the particle radius, which does not change. In summary, the energy is assumed to be constant.

It was already pointed out, that the particles are not independent due to the strong electrostatic interaction between particles. The high values of the coupling parameter (table 5.2) confirm this. The degree and kind of correlation of the particles will not be investigated here. The test on ergodicity should show, if the particles behave ergodic though there are correlations. If the differences between time and ensemble distributions are not negligible, this has to be considered if statistical or thermodynamical properties of a plasma crystal are examined. Then for example the temperature of a plasma crystal obtained by the ensemble average of the velocities in one frame can not be assigned to a single particle.

The stationarity of the single particle time series was investigated in chapter 5.3. While the velocity time series of each single particle could be called stationary within the statistical uncertainties, the displacements still exhibited nonstationarity. The reasons could be trends not identified due to the lack of a theoretical model, or real properties of the dynamics of the system.

5.5.2 Hypothesis Testing

Before passing over to the test on ergodic behaviour, some principles of statistical tests with regards to the comparison of two sets of values are explained. As reference for this and the following chapters mainly [30],[31] and [28] are used. In this chapter the expression 'data set' is used not in the sense of the whole outcome of a measurement but in the sense of a set of values as input for a statistical test.

A statistical test gives a probability that an assumption about a set of values is valid

within certain errors. Before applying the test, the assumption is expressed as a so called null hypothesis H_0. If two data sets are compared with respect to equality, H_0 is the assumption, that both data sets originate from the same underlying distribution of values, ie. they describe identical processes. The opposite case is then called alternate hypothesis H_A (both data sets differ). The aim of the test is to reject either H_0 or H_A, not to proof one of them.

As a next step, a confidence limit α is choosen. α is a value between 0 and 1. It expresses the probability of error if the test result leads to a rejection of H_0. Some tests allow the choice of a second parameter, β. This is the probability of error if the alternate hypothesis is rejected. Such kinds of test are called two-sided tests in opposite to the one-sided test, which have α as the only parameter. The accuracy of a conclusion from the test depends on the values choosen for α and β, respectively, since both determine finite intervals of the probability to draw a wrong conclusion from the test result or in other words, to make a mistake. Table 5.4 gives an overview of the occurrences of this errors, called α and β errors corresponding to the parameters choosen (taken from [30]). One can see there, that in case of undefined β such as for one-sided tests, it is not possible to accept the null hypothesis, since the error for accepting it is not defined. Then an acceptance of H_0 can not be evaluated and thus is not a valid statement.

After the confidence limit has been choosen, the test is applied to the data sets. It usually calculates a defined quantity, called statistic, from the data which expresses a difference between both data sets. Now it has to be quantified, how significant the found difference is in fact. Here either a limiting value dependent on the choosen confidence limit and the number of data points of the compared data sets can be looked up in tables. If the found difference is larger than this limiting value, it is called significant. Another approach is to directly calculate a probability for the found difference which is usually defined such that is decreases if the difference becomes larger. Thus it is the probability to obtain a larger difference than the found one. If the latter is already significantly large, is is not very likely to find a larger one.

conclusion from statistical test	reality	reality
	H_0 true	H_0 wrong
H_0 rejected	alpha error	correct
H_0 accepted	correct	beta error

Table 5.4: Appearances of alpha and beta errors. In the left column the conclusions drawn from the test result are listed. Both column to the right give the connection to the real situation (which is not known, else one would not apply the test) and the error which is done in the case of a wrong decision.

In the following, the test methods used here, namely the Kolmogorov-Smirnov test and

the Kuiper test, are described in more detail.

5.5.3 Kolmogorov-Smirnov and Kuiper Tests

The Kolmogorov-Smirnov test is a one-sided test which is applied to unbinned data sets, in other words no moments of distributions are compared such as mean or standard deviation as it is done elsewhere. Therefore it has the advantage that it is more or less independent of the kind of distribution of the values of the data sets, ie. it is not nessecary that the values are for example normally distributed, as it is required by the Student-test for equal means.

The null hypothesis of this test states the equality of two data sets. Since the test is one-sided, only α can be choosen. As it was discussed above, in this case the null hypothesis can only be rejected, but not accepted. We will choose an $\alpha = 0.05$ as it is commonly done. This means that a rejection of H_0 due to the test result will have an error of 5 % in this statement.

The data sets handed over to the test algorithm are two series of values taken from the data of displacements and velocities respectively. One is the time series of one single particle corresponding to the distribution of values in time. The other data set contains the corresponding quantity r or v of all particles in one frame, which was defined as the ensemble. Between these two the test statistic is computed. Then, consecutively, each particle trajectory in time is compared with each frame. As a restriction on the trajectories, only those particles have been choosen which have a trajectory length of the full measurement time. As an estimate of magnitudes: In average 100 single particles were compared with 9000 frames for one experiment. This yields $\approx 9 \cdot 10^5$ comparisons per experiment.

A second test is done with the Kuiper test, which is mainly based on the Kolmogorov-Smirnov test, but puts more weight on points farer away from the mean of the compared sets of values.

It follows a description of the algorithm and the output one obtains.

Kolmogorov-Smirnov-Statistic The test method has been implemented as is is described in [28]. It gets as input two data arrays as described above with lengths N_1 and N_2. For the examples here the displacements r are used. The arrays are sorted by their values in ascending order. Then the cumulative distribution functions $S_{N_1}(r)$ and $S_{N_2}(r)$ of the values are derived. A cumulative distribution function $S_{N_j}(r), j \in 1, 2$ gives for a certain r the number of points with lower values than r, divided by the total number of points N_j. The cumulative distribution functions for the displacement of one particle and one frame are displayed in figure 5.41 a).

The statistic derived with this test is called Kolmogorov-D. It is computed from the

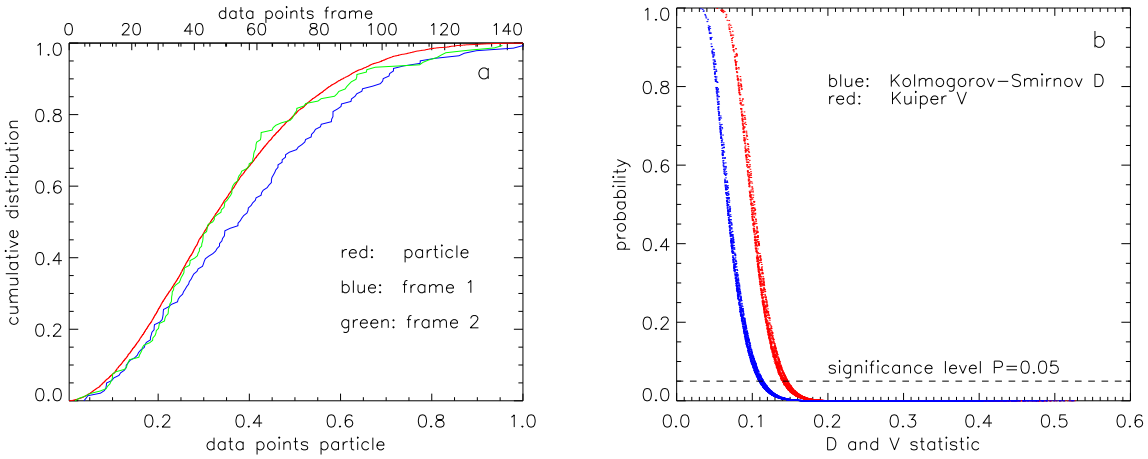

Figure 5.41: a) Cumulative distribution function for the displacements $r(t)$ of one particle (red line) and two frames (blue and green lines). b) Probability $P_{KS}(D)$ vs. D (Kolmogorov-Smirnov-Statistic, blue), and $P_{KP}(V)$ vs. V (Kuiper-Statistic, red).

cumulative distribution functions S_{N_1} and S_{N_2} as

$$D = \max_{-\infty<r<+\infty} |S_{N_1}(r) - S_{N_2}(r)| \quad \text{Kolmogorov-Smirnov D} \tag{5.59}$$

D is a measure for the maximum absolute difference between S_{N_1} and S_{N_2}. The significance of D, respectively the probability to get a certain value of D or a larger value by chance under the assumption that the S_{N_j} are drawn from the same distribution, is derived by

$$P_{KS}(D) := Q_{KS}\left(\left[\sqrt{N_e} + 0.12 + \frac{0.11}{\sqrt{N_e}}\right] \cdot D\right) \tag{5.60}$$

with the function $Q_{KS}(\lambda)$ defined as

$$Q_{KS}(\lambda) = 2\sum_{k=1}^{\infty}(-1)^{k-1}e^{-2k^2\lambda^2}$$
$$Q_{KS}(0) = 1 \quad , \quad Q_{KS}(\infty) = 0 \tag{5.61}$$

and the effective number of data points

$$N_e = \frac{N_1 N_2}{N_1 + N_2} \tag{5.62}$$

The calculation of the probability P_{KS} is valid for $N_e \geq 4$. In average, for the data used here, $N_e \approx 100$. The Kolmogorov-Smirnov-Test is more accurate around the median of the data. Due to the kind of statistic it calculates, it is useful to find shifts between the

compared data sets. A variation of the test, the Kuiper test, is more sensitive to differences in the tails of the cumulative distribution functions and thus can identify spreads between the data sets or different shapes of the distribution of values (see [28], chapter 14 for details).

Kuiper-Statistic The Kuiper statistic V is defined as

$$V = D_+ + D_- = \max_{-\infty<r<+\infty}[S_{N_1} - S_{N_2}] + \max_{-\infty<r<+\infty}[S_{N_2} - S_{N_1}] \tag{5.63}$$

The probability equivalent to P_{KS} is given by

$$P_{KP}(V) := Q_{KP}([\sqrt{N_e} + 0.155 + \frac{0.24}{\sqrt{N_e}}] \cdot V) \tag{5.64}$$

with the function $Q_{KP}(\lambda)$ given by

$$\begin{aligned} Q_{KP}(\lambda) &= 2\sum_{k=1}^{\infty}(4k^2\lambda^2 - 1)e^{-2k^2\lambda^2} \\ Q_{KP}(0) = 1 \quad &, \qquad Q_{KP}(\infty) = 0 \end{aligned} \tag{5.65}$$

N_e is the same as defined in equation (5.60). V measures the differences above and below both cumulative distribution functions, and thus is more sensible to deviations in the tails.

Interpretation of P_{KS} and P_{KP} P_{KS} and P_{KP} both return, for a found D or V, a probability value $\in [0, 1]$. The closer this is to zero, the more significant is the difference between the compared data sets. It is not the probability to get this particular D or V, but the probability to find a $\tilde{D}$ or $\tilde{V}$ which is larger than D resp. V. If D or V are already sufficiently small, it is very unlikely to find an even smaller value. Therefore P_{KS} and P_{KP} can directly be compared with the significance level determined by α, which was choosen as 0.05. Any $P_{KS/KP}$ smaller than $\alpha = 0.05$ leads to a rejection of the null hypothesis with an error of 5 %. That means, if 100 independent tests are performed on data sets which are in fact taken from the same underlying distribution of values (e.g. choose 10 values randomly from a set of 1000 normally distributed data and compare them with 100 also randomly choosen points from the same distribution), then 5 of the test results will yield a $P_{KS/KP}$ leading to a rejection of the null hypothesis, though this is the wrong decision.

Interpretation of Multiple Test Results Both test were applied to the measurements Ia, IIa and IIIa. The displacements r and the absolute velocities v were compared, as it was explained above, between the single particle time series and the values of r and v respectively of all particles in one frame. The results for the displacement are presented in section 5.5.3.1, the velocities follow in section 5.5.3.2.

Experiment	Ia	IIa	IIIa
N_P	109	121	134
N_f	8298	8798	8048
N_{tot}	904591	1064679	1078566
$N_{\%f}$	151	158	169
$N_{0.05,KS}$ [%]	75.9	87.0	94.1
$N_{0.05,KP}$ [%]	74.0	87.0	94.8

Table 5.5: Displacements: Numbers of compared data sets N_P (single particles) and N_f (ensembles), total number of comparisons N_{tot}, average number of particles in the ensemble $N_{\%f}$ and the percentage of test results $P_{KS/KP}$ smaller than 0.05, $N_{0.05,KS}$ and $N_{0.05,KP}$.

It was explained in the beginning of this chapter, that a proof is not possible by the application of statistical tests, and in particular the statistics computed here allow only a rejection, not an acceptance, of the null hypothesis. Further for each measured data set Ia, IIa, and IIIa we computed $\sum 1 \cdot 10^6$ comparisons between particle trajectories in time and ensembles of particles. Each result of a comparison has to be seen as independent of each other. That means, for each single test result one can reject the null hypothesis of equality due to a probability $P_{KS/KP} \leq 0.05$ with an error of 5 %, as explained above, for the two particular data sets which were compared. The interpretation of all comparisons together is a more difficult task. A measure for the significance of the rejection of the null hypothesis of e.g. 70 % of all comparisons is required in this case. Since no statistic is known which could answer that question, a qualitative interpretation will be done.

5.5.3.1 Results of Statistical Tests for Particle Displacements

To get an estimate of the number of single test runs and the number of data points in each of the two data sets handed over to the algorithm in each run, these values are listed in table 5.5, where N_P is the number of particle trajectories (distributions in time), N_f is the number of ensembles (or frames), N_{tot} is the total number of test runs, i.e. the total number of comparisons of single particles with ensembles. $N_{\%f}$ is the average number of particles contributing to an ensemble. The number of data points contained in a single particle trajectory is equal to N_f. The last two lines contain the percentage $N_{0.05,KS}$ and $N_{0.05,KP}$ of N_{tot} of outcomes of the test for which a P_{KS} or $P_{KP} \leq \alpha = 0.05$ has been found.

A graphical evaluation is done in figure 5.42. The x-axis is divided in equally spaced bins of the width 0.1 and is labelled P_d which indicates discrete points of a probability. Then the fraction of occurrences of $P_{KS} \leq P_d$ are plotted versus P_d (left side) and the fraction of $P_{KP} \leq P_d$ (right side) respectively. Since in chapter 5.4.3 some groups of particles were identified according to the shape of the displacement distribution function, these were picked out of the N_P trajectories and the corresponding test results of comparisons of just

these particles with all ensembles are plotted additionally in the colors they were assigned to before. Red corresponds mainly to particles around the rotation center of the crystal, while blue and green are located in the outer ranges. Note that particles of another color stayed in the ensembles here. If a 'red' particle was choosen as the trajectory in time, the ensemble was constituted of 'red' or 'green' particles, too.

In summary the fraction of N_{tot} of test results of the Kolmogorov-Smirnov test which are smaller than 0.05 increase from 75.9 % for measurement Ia to 94.1 % for IIIa with the peak-to-peak voltage at the lower electrode. This numbers could be reduced by 5 % due to the error done in rejection a possibly correct null hypothesis, but still they are too large to conclude an equality of the behaviour of a particle in time and the ensemble. The Kuiper statistic yield nearly the same result, so the difference between particle and ensemble is an overall feature and not just a shift of the mean. Also the selection of groups of particles, marked in red, blue and green in figure 5.42, does not produce a relevant difference in the statement, though it should be noted that the red line is always located below the others. The red particles were the ones in the center of the crystal.

The conclusion of a significant difference in the dynamical behaviour of particles and ensemble with regard to the displacement is confirmed by the large deviations of the shape of the probability distributions of the single particles found in chapter 5.4.3. These exhibited a shift of the mean as a change of the standard deviation (see figure 5.37) which are likely the reason of the result of the statistics.

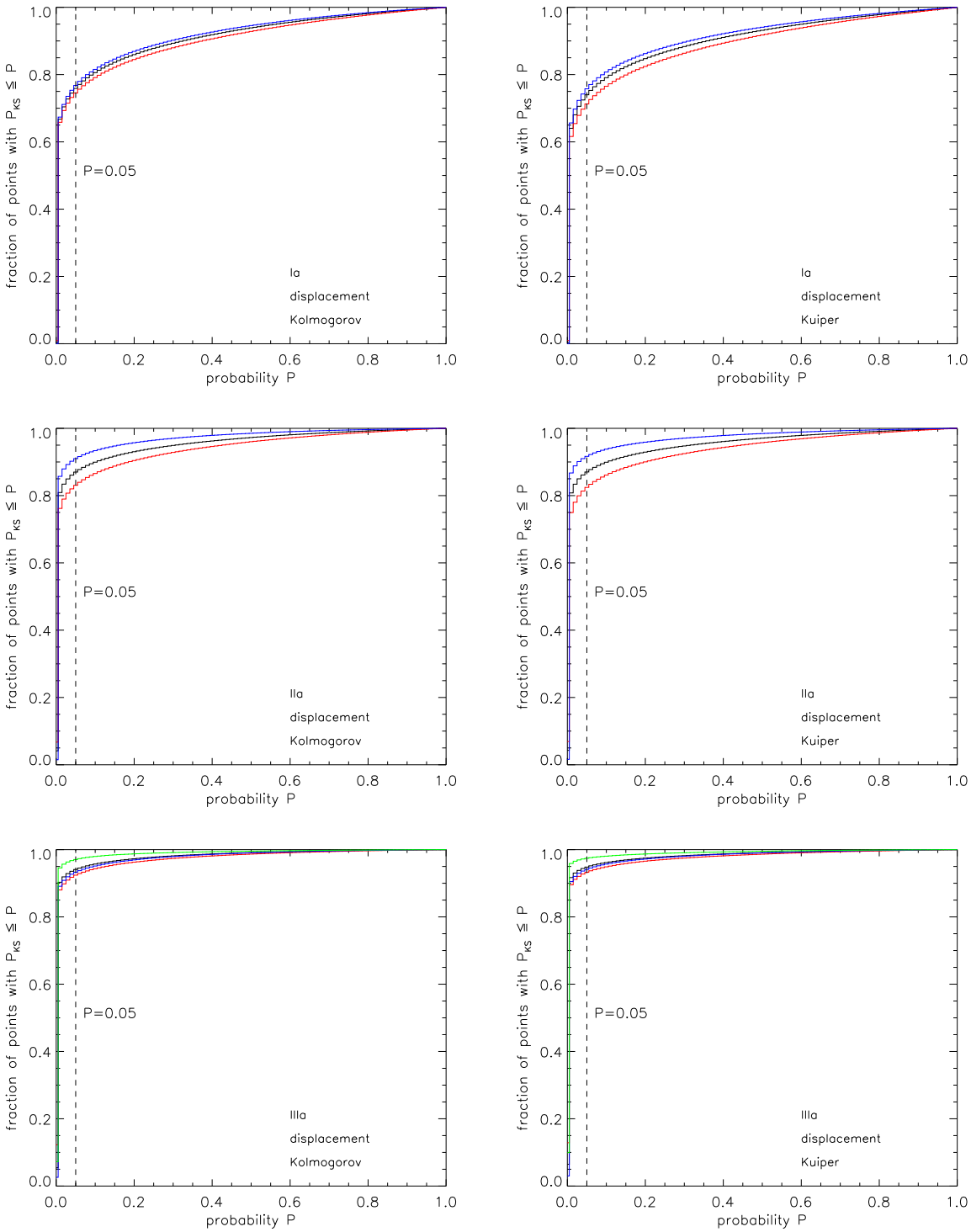

Figure 5.42: Displacements: Kolmogorov-Smirnov test results (left) and Kuiper test results (right). Plotted is the percentage of particles with $P_{KS}(D)$ smaller than the value on the x-axis. The colored lines include only trajectories which belong to the corresponding group found in chapter 5.4.3, compared with all frames. The black line includes all trajectories. The dashed line indicates the limit $\alpha = 0.05$.

Experiment	Ia	IIa	IIIa
N_P	109	121	134
N_f	8297	8797	8047
N_{tot}	904482	1064558	1078432
$N_{\%f}$	151	158	169
$N_{0.05,KS}$ [%]	18.3	18.3	19.9
$N_{0.05,KP}$ [%]	13.3	12.1	12.8

Table 5.6: Velocities: Numbers of compared data sets N_P (single particles) and N_f (ensembles), total number of comparisons N_{tot}, average number of particles in the ensemble $N_{\%f}$ and the percentage of test results $P_{KS/KP}$ smaller than 0.05, $N_{0.05,KS}$ and $N_{0.05,KP}$.

5.5.3.2 Results of Statistical Tests for Velocities

Exactly the same procedure as for the displacements before is done for the absolute velocities. Table 5.6 lists the corresponding magnitudes for the statistical test. The illustration in figure 5.43 follows the same principle as before.

In opposite to the displacements, no common increase of the fraction of probabilities smaller 0.05 can be found for the velocities in both test statistics. The fraction stays at $\sim$ 18 % for the Kolmogorov-Smirnov test and at $\sim$ 12 % for the Kuiper statistic. Here a not neglectable difference between both statistics exists. It seems that if there are significant differences in the particle trajectories and the ensembles, they appear more in a shift of the mean as in a change of the shape of the corresponding distribution of values.

The curves in figure 5.43 show a continuous increase toward 1. This makes it difficult to find a valid interpretation, since the $P_{KS/KP}$ seem to be uniformly spread in the interval $[0, 1]$. In other words, any probability $P_{KS/KP}$ is equally likely to obtain if a test is made for two arbitrary choosen sets of velocities.

If the result would be more unique, one would tend to accept the null hypothesis of equality of time and ensemble distributions of the velocity, even if it would mean to accept an unknown error. But in the case of uniformly distributed probabilities this would be risky. We remain with an open question here, but will not reject the null hypothesis for the velocities. This does not mean that it is the correct assumption, but more specific statistical methods would be needed to investigate the equality.

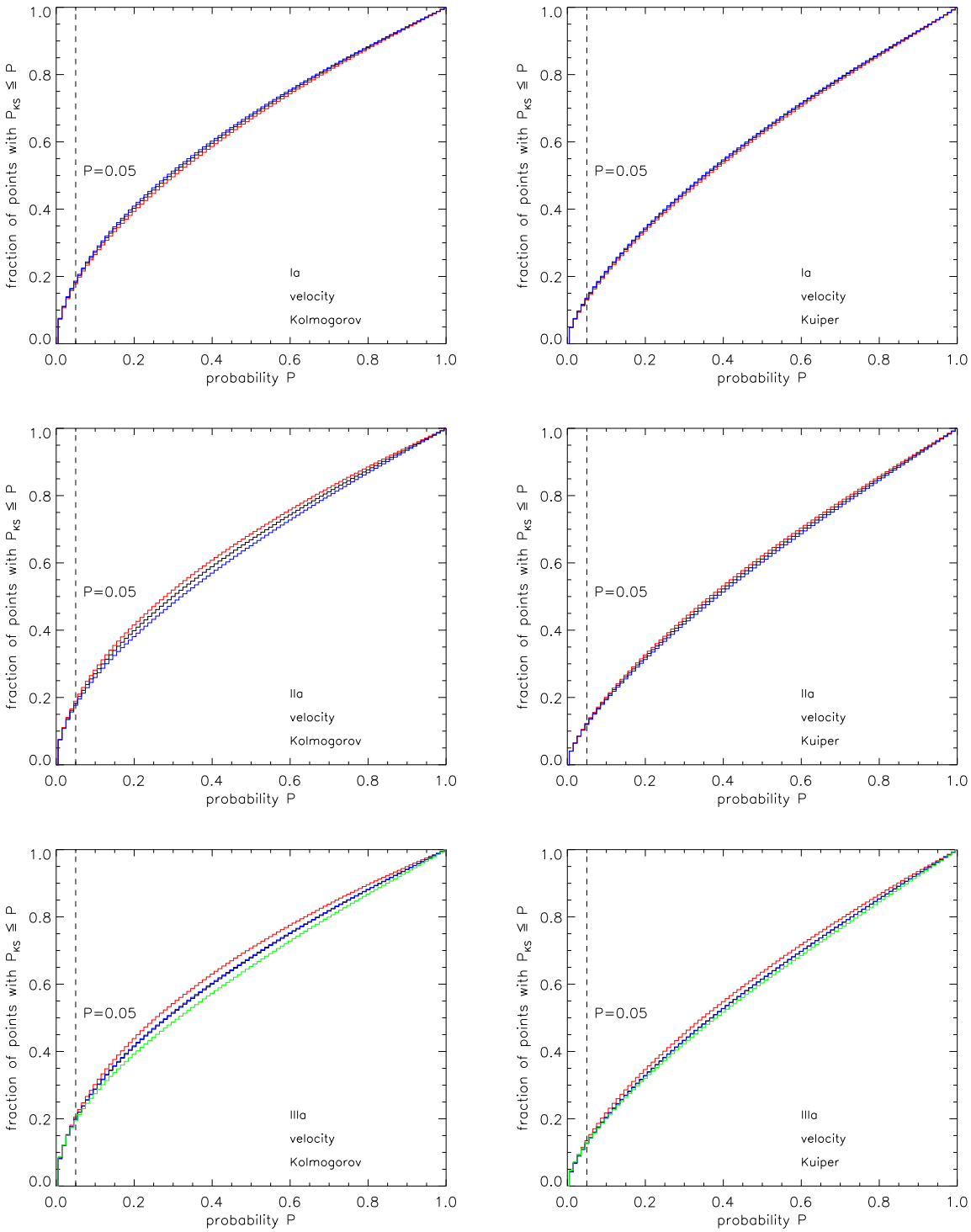

Figure 5.43: Velocities: Kolmogorov-Smirnov test results (left) and Kuiper test results (right). Plotted is the percentage of particles with $P_{KS}(D)$ smaller than the value on the x-axis. The colored lines include only trajectories which belong to the corresponding group found in chapter 5.4.3, compared with all frames. The black line includes all trajectories. The dashed line indicates the limit $\alpha = 0.05$.

Experiment	Ia	IIa	IIIa
N_P			
red	43	61	23
blue	66	60	77
green	-	-	34
N_f	8298	8798	8798
N_{tot}			
red	356857	536739	202377
blue	547734	527940	677523
green	-	-	299166
$N_{\%f}$			
red	63	79	36
blue	89	78	96
green	-	-	36
$N_{0.05,KS}$			
red	49.2	71.2	68.7
blue	72.2	89.3	91.5
green	-	-	99.3
$N_{0.05,KP}$			
red	49.8	69.1	66.5
blue	70.4	91.0	92.9
green	-	-	99.1

Table 5.7: Numbers of compared data sets N_P (single particles) and N_f (ensembles), total number of comparisons N_{tot}, average number of particles in the ensemble $N_{\%f}$ and the percentage of test results $P_{KS/KP}$ smaller than 0.05, $N_{0.05,KS}$ and $N_{0.05,KP}$. *Particles and ensemble are divided into groups regarding to the shape of their displacement distribution function. They are labeled red, blue and green*

5.5.3.3 Spatial Dependence of the Test Results

The question arose if the test results might be dependent spatial positions of particles in the crystal.

As it was indicated in the former chapters, the particles could be separated into groups with approximately different dynamical behaviour with respect to the particle's displacement distributions. Since the test results in section 5.5.3.1 leaded to a rejection of the null hypothesis in most cases, the tests were applied again, but now the also the ensemble of particles were separated. That means, 'blue' particle trajectories were compared with ensembles of 'blue' particles, and so on. This has only been done for the displacments. The results are presented in table 5.7 and figure 5.44 in the same manner as before.

It can bee seen, that the dependence of the fractions smaller 0.05 on the peak-to-peak voltage stay, as does the equalitiy of Kolmogorov-Smirnov and Kuiper statistic. But the curves of different groups splitted much farer than before, and this is not dependent on the smaller number of particles in the ensembles. But still $\sim$ 50 % is the lower limit to the fraction of comparisons with an $P_{KS/KP} \leq 0.05$

Interesting is the fact, that particles located near the center of rotation (red) yield the best results with regard to not reject the null hypothesis.

5.5.4 Conclusion of the Test

The particles displacements from their mean lattice site, compared as trajectories in time of single particles with ensembles of all particles at a particular time, seem not to exhibit ergodic behaviour in more than 75 % of all cases. This number still increases with peak-to-peak voltage. The assumption of ergodic behaviour should be rejected, or at least thought about carefully.

The velocities could behave ergodic, but this is a statement which can not be given based on the tests performed here. The small number of rejections of the null hypothesis compared with the displacements confirm the probability to find ergodicity, if more specific tests would be applied.

Figure 5.45 summarizes the results obtained from the statistical tests. The percentages of probabilities P_{KS} (left panel) and P_{KP} (right panel) smaller than 0.05 for both displacements and velocities are plotted versus the peak-to-peak voltage U_{pp}.

One possible reason for the increase of rejections with increasing U_{pp} and with inrceasing radial distance of the particles to the center of rotation could be a spatial dependence of the coupling parameter Γ inside the crystal. Thus the particle dynamics, which are determined by the degree of coupling, could change within the crystal as it was observed in section 5.4.3, where the displacement distributions were investigated. In such a case it would not be applicable to assume ergodic behaviour and perform ensemble averages for the particle displacements.

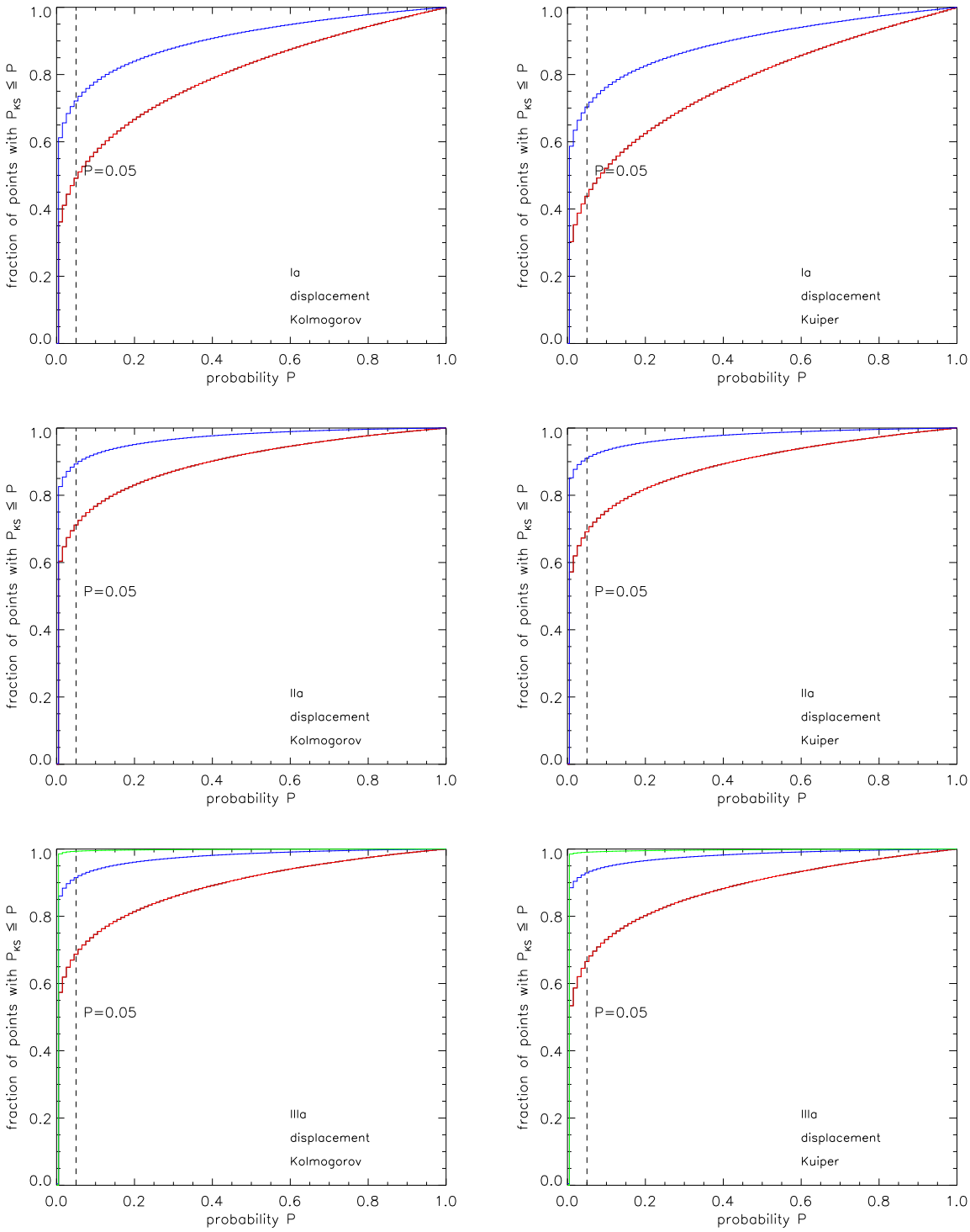

Figure 5.44: Result of Kolmogorov-Smirnov and Kuiper test for the displacements while particle trajectories and particles contributing to the ensemble were choosen for the data sets handed to the test accordingly to the colored groups.

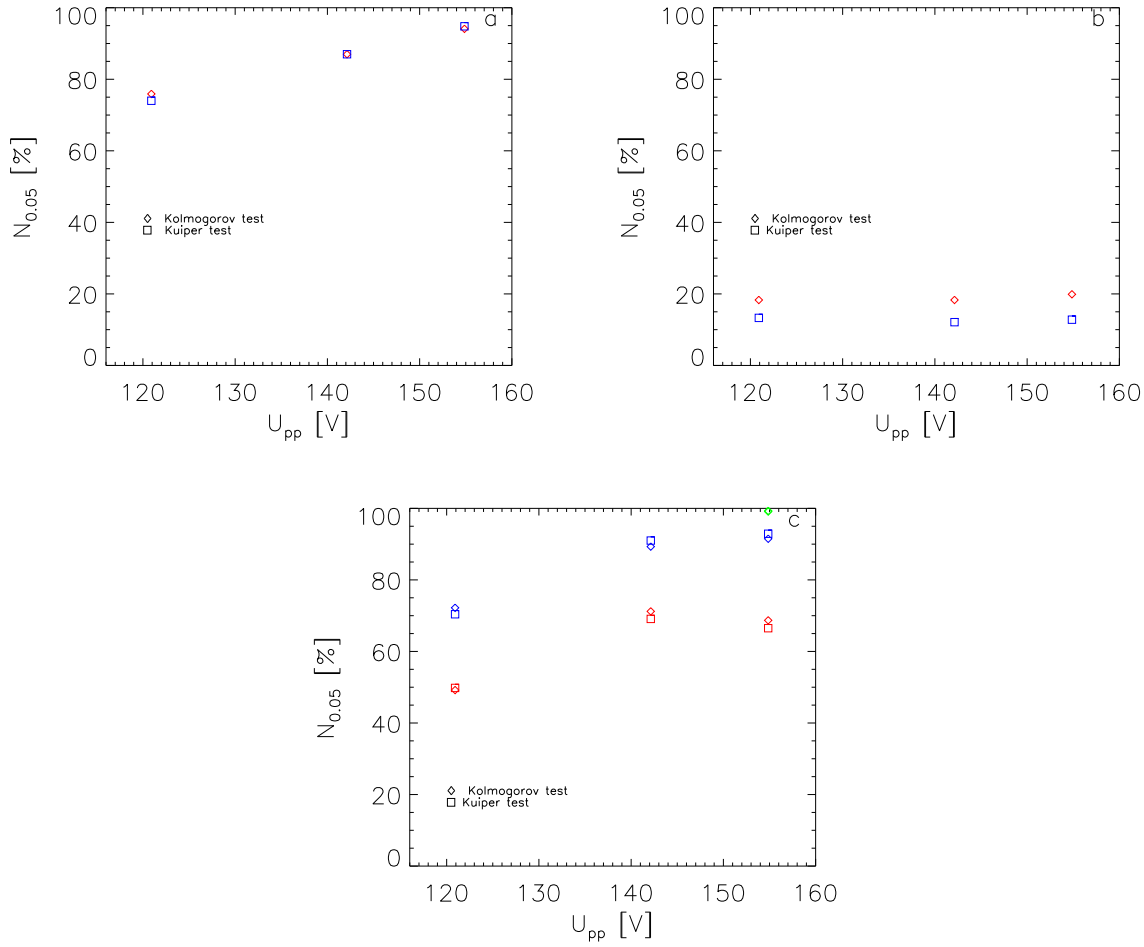

Figure 5.45: $N_{0.05,KS}$ (diamonds) and $N_{0.05,KP}$ (squares) vs. peak-to-peak voltage U_{pp} for a) displacements and b) velocities and c) displacments splitted into the introduced particle groups.

Chapter 6

Summary and Conclusion

Summary The aim of this thesis was to examine the dynamical behaviour of particles in a plasma crystal with respect to the validity of the assumption of ergodic behaviour related to fundamental properties of the particles described by their coordinates and velocities.

A single-layer plasma crystal was generated as a 2-dimensional ensemble of particles and long-time measurements of the particle coordinates have been recorded. The experimental task was to control external experimental parameters such that a stable system was established. Parameters were choosen such that a crystalline, strongly coupled state was achieved.

Global trends were identified by a sliding windows technique and Fourier transform methods. The trends were removed from the data by decomposition of the time series of particle coordinates into the different aspects of motions and by selecting the relevant segments for further investigation.

Time series of the displacements from the mean lattice site and the velocities were obtained for each single particle. These were tested for stationarity in terms of running averages and running standard deviations.

The distribution functions of velocities and displacements of each single particle describing its intrinsic dynamics have been investigated in dependence on the particular particle position within the crystal and with respect to the physical quantities determining the shape of the distributions such as temperature and interparticle potential.

Statistical tests were applied to the detrended data, which compared the set of values of the displacement and the velocity, respectively, of single particle trajectories with the set of corresponding values at a fixed time, i.e. in one particular image of the data set. The test method returned a quantity which could be interpreted in terms of the significance of the difference found between the compared sets.
To improve the statistics, the comparison was carried out between each particle and each frame independently. Thus a large number of approximately 1 million test results per data

set could be evaluated.

Conclusion The question for ergodic behaviour of the particles in a plasma crystal could not be answered definitely. On reason is that tests were carried out only on absolute values of quantities. The surfaces covered by the system in its real phase space were not investigated. In consequence, any statement concerning ergodic behaviour is applicable just to the absolute values of a quantity in a 1-dimensional space, and no conclusions can be drawn on the dynamics for higher dimensional distributions. With regard to the result of the statistical tests applied, the assumption of ergodicity in the displacements has to be rejected. Though this did not account for the velocities, ergodicity can not be proved uniquely by the test methods used. The reasons for this restricted result cover a large scale.

Starting with the data acquisition, the constance of experimental parameters such as pressure and peak-to-peak voltage might be adequate for short-time measurements or investigations of macroscopic quantities, but the influences on the particle dynamics are not negligible, as it became evident in the radial contractions of the whole crystal due to small power fluctuations.

Global trends such as rotation affect all particles in a plasma crystal and contaminate the time series of the single particles. Thus the process of removing trends is a crucial point in the data analysis. It has not been elaborated before, since it is not essential in the usual case of short-time measurements. Further in the latter case trends might be hidden at all. In the case presented here the removing of trends was possible only if a theoretical model applicable to all particles could be found. Since this was not always possible, nonstationarities were detected in the single particle time series.

The investigation of the distribution functions of displacements and velocities of the single particles in time revealed a Maxwellian velocity distribution weakly dependent on the distance of a particle to the rotation center of the crystal. The displacement distributions were found to diverge completely when compared with each other. The reason could be either artefacts of trends not properly removed from the time series, or a real physical effect maybe related to the confinement potential.

In any case, particles can not be considered as equal realisations of a system since they exhibit different dynamical behaviour with regard to the phase space of displacements. In consequence, the rejection of the assumption of ergodicity follows, at least for similar experiments such as performed here, which is affirmed by the result of the statistical test.

On exception can be made for the particle velocities. A lot of evidences were found for possible ergodic behaviour with respect to the averaged velocities and the particle temperature, respectively. Although the statistical test did not reveal a unique result, this in no final conclusion. Since temperatures were found to be approximately constant for the particles contributing to an ensemble, an averaging could be valid here and a common particle temperature could be defined.

The results presented are not a final proof, since a lot of experimental conditions could be improved to fulfil the requirements of a system in equilibrium in a better way. Diagnostic data should be captured during a measurement to give the possibility of identifying and finally suppressing externally caused disturbances. The trends in the system could be investigated in more detail and a detrending procedure could be developed which takes into account all the prominent influences. Quantities like the particle charge could be considered in the description of particle dynamics. The influence of charge fluctuations was ignored here, but it might be an important factor, too. Finally, not just the absolute values of quantities like the displacement and the velocity could be examined, but the structures in a higher dimensional phase space using for instance delayed coordinates. This could reveal a lot of information not yet evident.

References

[1] H. Ikezi: *Coulomb solid of small particles in plasmas*, Phys. of Fluids, 1764-1766 (1966)

[2] H. Thomas, G. E. Morfill, V. Demmel, J. Goree, B. Feuerbacher, D. Möhlmann: *Plasma Crystal: Coulomb Crystallization in a Dusty Plasma*, Phys. Rev. Lett. 73 (5), 652-655 (1994)

[3] R. A. Quinn, C. Cui, J. Goree, J. B. Pieper, H. Thomas, G. E. Morfill: *Structural analysis of a Coulomb lattice in a dusty plasma*, Phys. Rev. E 53 (3), 2049-2052 (1995)

[4] R. Wilhelm: *Vorlesungsskript Experimentelle Plasmaphysik I* (2001/2002)

[5] A. Piehl, A. Melzer: *Dynamical processes in complex plasmas*, Plasma Phys. Control. Fusion 44 (2002)

[6] U. Konopka, G. E. Morfill, L. Ratke: *Measurement of the Interaction Potential of Microspheres in the Sheath of a rf Discharge*, Phys. Rev. Lett. 84 (5), 891-894 (1999)

[7] M. Liebermann, A. Lichtenberg: *Principles of plasma discharges and material processing*, John Wiley & Sons, Inc. (1994)

[8] M. Zuzic, A. V. Ivlev, J. Goree, G. E. Morfill, H. M. Thomas, H. Rothermel, U. Konopka, R. Sütterlin, D. D. Goldbeck: *Three-Dimensional Strongly Coupled Plasma Crystal under Gravity Conditions*, Phys. Rev. Lett. 85 (19), 4064-4067 (2000)

[9] A. Melzer, V. A. Schweigert, I. V. Schweigert, A. Homann, S. Peters, A. Piehl: *Structure and stability of the plasma crystal*, Phys. Rev. E 54 (1), 46-49 (1995)

[10] U. Konopka: *Wechselwirkungen geladener Staubteilchen in Hochfrequenzplasmen*, Dissertation (2000)

[11] A. G. Zagorodny, P. P. J. M. Schram, S. A. Trigger: Stationary Velocity and Charge Distributions of Grains in Dusty Plasmas, Phys. Rev. Lett. 84 (16), 3594-3599 (2000)

[12] A. V. Ivlev, G. E. Morfill: *Anisotropic dust lattice modes*, Phys. Rev E 63, 016409 (2000)

[13] V. A. Schweigert, I. V. Schweigert, A. Melzer, A. Homann, A. Piehl: *Plasma crystal melting: A nonequilibrium phase transition*, Phys. Rev. Lett. 80 (24), 5345-5348 (1997)

[14] A. V. Ivlev, U. Konopka, G. E. Morfill: *Melting of monolayer plasma crystals*, Phys. Rev. E 68, 0260405 (2003)

[15] S. Nunomura, J. Goree, S. Hu, X. Wang, A. Bhattacharjee: *Dispersion relations of longitudinal and transverse waves in two-dimensional screened Coulomb crystals*, Phys. Rev. E 65 (2002)

[16] D. Samsonov, J. Goree, H. M. Thomas, G. E. Morfill: *Mach cone shocks in a two-dimensional Yukawa solid using a complex plasma*, Phys. Rev. E 61 (5), 5557-5572 (1999)

[17] R. A. Quinn, J. Goree: *Single-Particle Langevin model of particle temperature in dusty plasmas*, Phys. Rev. E 61 (3), 3033-3041 (1999)

[18] P. S. Epstein: *On the resistance experienced by spheres in their motion through gases*, Phys. Rev. 23, 710-733 (1924)

[19] R. A. Quinn, J. Goree: *Particle Interaction Measurements in a Coulomb Crystal Using Caged-Particle Motion*, Phys. Rev. Lett. 88 (19), (2002)

[20] S. Ratynskaia, C. Knapek, K. Rypdal, S. Khrapak, R. A. Quinn, G. E. Morfill: *Statistics of particle transport in a 2D dusty plasma cluster*, submitted

[21] W. Greiner, L. Neise, H. Stöcker: *Thermodynamik und statistische Physik*, Verlag Harri Deutsch, 1. Aufl., pages 203-207 (1987)

[22] Frederick Reif: *Statistische Physik und Theorie der Wärme*, de Gruyter (1987), Chapter 6

[23] I. E. Farquhar: *Ergodic Theory in Statistical Mechanics*, John Wiley & Sons, Ltd. (1964)

[24] R. A. Quinn: *Experimental Studies of Strongly-Coupled Dusty Plasmas*, PhD Thesis (2000)

[25] P. J. Hargis, Jr. et al., Rev. Sci. Instrum. 65, 140 (1994)

[26] C. F. Bohren, D. R. Huffman: *Absorption and Scattering of Light by Small Particles*, John Wiley & Sons, Inc. (1983)

[27] John R. Taylor: *An Introduction to Error Analysis*, University Science Books (1997)

[28] William H. Press, Saul A. Teukolsky, William T. Vetterling, Brian P. Flannery: *Numerical Recipes in C*, Cambridge University Press, Second Edition (2002), Online Edition: http://www.library.cornell.edu/nr/bookcpdf.html

[29] U. Konopka, D. Samsonov, A. V. Ivlev, J. Goree, V. Steinberg, G. E. Morfill: *Rigid and differential plasma crystal rotation induced by magnetic fields*, Phys. Rev. E 61 (2), 1890-1898 (1999)

[30] Lothar Sachs: *Statistische Auswertungsmethoden*, Springer Verlag, 3. Auflage (1972)

[31] Rainer Sachs: *Detektion von nichtlinearem Determinismus in syntetischen und realen Zeitserien*, Dissertation

List of Figures

2.1 Overview of plasmas and the corresponding coupling parameter Γ. Dusty plamas are located in the upper left corner (also called colloidal plasmas) with $\Gamma > 1$. 6

2.2 External forces acting on a dust particle in a RF discharge. The ion drag force mentioned in the text is not included. 8

2.3 3-dimensional crystal structure: a) hexagonal close-packed and b) face-centered cubic. 9

2.4 Real image of a 2D plasma crystal (right) and corresponding triangulation of the particle positions (left). Marked in red is the hexagonal structure. . . 9

4.1 Image of the GEC cell used for experiments. 22

4.2 Top: Schematic top view of the experimental setup. Bottom: Schematic side view of the experimental setup 23

4.3 Electrode cap for manipulating the horizontal potential 24

4.4 Single layer plasma crystal illuminated by the laser. 25

4.5 Image of a 2D plasma crystal (right) and numbering of particles after the tracking (left). 27

4.6 Left: Random measurement error distribution (normalized to unit area) and gaussian fit, Right: Close-up of the inner part of the error distribution 32

4.7 Error distribution (normalized to unit area) and Gaussian fit estimated separately for the x- and y-direction 33

4.8 Right: Image of the crystal in the test experiment, Left: Particle positions in that frame. Marked on the left side are particles with local maxima in the distribution of the frame to frame displacement 34

4.9 Linear chain of three particles. 35

4.10 a) Magnification m vs. kinetic energy k_BT, b) $\langle \Delta r \rangle$ vs. kinetic energy k_BT and pixel-noise for $m = 1$ 36

4.11 Maximum distance from mean lattice site vs. $U_{pp,1}$. The colors indicate different pressures from 1.0 Pa to 5.9 Pa. 40

4.12 N_P vs. $U_{pp,1}$ for two magnifications $m = 1.0$ (top) and $m = 1.5$ (bottom). The colors indicate different pressures from 1.0 Pa to 5.9 Pa. 42

5.1 Plotted versus U_{pp} are a) Mean interparticle spacing Δ, b) r_{max}, c) $\lambda_{D,exp}$ (black) and $\lambda_{D,est}$ (red), d) Comparison of the magnitudes of Δ, λ_D and r_{max}, e) $\kappa = \Delta/\lambda_{D,est}$, f) Γ. 48

5.2 ν_E in dependence of the particle charge for $\kappa = 2$ and Δ from table 5.2. a) low resolution, b) high resolution 50

5.3 Mean absolute velocity $\overline{v}$ vs. U_{pp} as comparison for both magnifications. The error bars include the measurement error. 51

5.4 Example of the development of running mean and standard deviation for one particle. a) $\overline{r}_{i,w}$, b) $\sigma_{r,i,w}$, c) $\overline{v}_{i,w}$, d) $\sigma_{v,i,w}$. The error bars include the position error δr and δv respectively, and the statistical uncertainty. For $\overline{r}_{i,w}$ the error was too small to be visible. 55

5.5 Running mean $\hat{r}_w$ (left images) and running standard deviation $\hat{\sigma}_{r,w}$ (right images) for two window sizes. Data sets Ia, IIa, IIIa (low resolution). The error bars where only plotted for $L = 300$, if both data sets where too close. 56

5.6 Running mean $\hat{v}_w$ (left images) and running standard deviation $\hat{\sigma}_{v,w}$ (right images) for two window sizes. Data sets Ia, IIa, IIIa (low resolution). . . . 57

5.7 Percentage of differences Σ smaller zero for a) running mean and standard deviation of the displacement, b) running mean and standard deviation of the velocities. For stationary systems ≈ 100 % should be smaller zero. . . . 58

5.8 Power spectrum of a) $r(t)$ and b) $v(t)$ of one single particle. The power is normalized to the mean squared amplitude. 60

5.9 Power spectra of displacement (left) and velocity (right), averaged over all particles. Data sets Ia, IIa, IIIa (low resolution). The y-axis has a logarithmic scale. 62

5.10 Log-log plot of the fraction of total power in frequency ranges [0,0.01], [0.01,0.1], [0.1,1], [1,5], [5,10], [10,15] Hz for a) displacement and b) velocities. 63

5.11 Maximum values of power in frequency intervals of 1 Hz from 0 to 15 Hz for a) displacement and b) velocities. Marked by arrows are the peaks detected in the power spectra. 63

5.12 Overlay of particle trajectories of 2000 consecutive frames. The colors from red to yellow indicate the propagating time. 65

5.13 Ω_i vs. $\overline{R}_i$. The dashed lines are linear fits to $\Omega_i(\overline{R}_i)$. The median of Ω_i and the fit parameters are displayed in the diagrams. The lower right panel shows the median Ω vs. U_{pp} for all data sets. 67

5.14 Y_i vs. X_i. The red cross marks the median (X, Y) for all particles. 68

5.15 $X(t)$ (left) and $Y(t)$ (right). The dashed line is the median value of X or Y from the first fit (equation (5.31)) which was used as starting value here. 70

5.16 Flow of particles represented as arrows for data sets Ia (upper left), IIa (upper right) and IIIa (below). 72

5.17 $\overline{R}_k$ vs. time for an illustration of radial breathing. The grey graph is the total radius of the original, raw data. The vertical colored lines mark the segments that are cut out between. 75

5.18 Effect of removing common trends from the data. The images show an overlay of the particle coordinates of 2000 frames after the consecutive subtraction of following trends: a) Rotation, b) Translation, c) Linear flow, d) Segments with large radial fluctuations. 76

5.19 Top panels: Time series of $r(t)$ of a single particle before (left) and after (right) the detrending. Bottom: Velocity $v(t)$ before (left) and after (right) detrending for the same particle. 77

5.20 Running mean $\hat{r}_w$ (left images) and running standard deviation $\hat{\sigma}_{r,w}$ (right images) for two window sizes. The error bars where only plotted for the window size 300. The solid line shows the mean over all frames. 78

5.21 Running mean $\hat{v}_w$ (left images) and running standard deviation $\hat{\sigma}_{v,w}$ (right images) for two window sizes. The solid line shows the mean over all frames. 79

5.22 Percentage of differences Σ smaller zero compared with the quantities before trends were removed for a) running mean of the displacement, b) running standard deviation of the displacement, c) running mean of the velocity, d) running standard deviation of the velocity. For stationary systems 100 % should be smaller zero. 80

5.23 Power spectra of displacement (left) and velocity (right), averaged over all particles. Data sets Ia, IIa, IIIa after detrending. 81

5.24 Log-log plot of the fraction of total power in frequency ranges [0,0.01], [0.01,0.1], [0.1,1], [1,5], [5,10], [10,15] Hz for a) displacement and b) velocities. 82

5.25 Maximum values of power in frequency intervals of 1 Hz from 0 to 15 Hz for a) displacement and b) velocities. Marked are the peaks detected before the detrending. 82

5.26 Displacement: running mean $\overline{r}_{i,2}$ vs. $\overline{r}_{i,1}$ for each particle in a data set (left) and running standard deviation $\sigma_{r,i,2}$ vs. $\sigma_{r,i,1}$ (right). 85

5.27 Σ vs. R as a measure for the deviation of a) running mean $\overline{r}_{i,2}$ vs. $\overline{r}_{i,1}$ (left) and b) running standard deviation $\sigma_{r,i,2}$ vs. $\sigma_{r,i,1}$ (right). $\Sigma < 0$ indicates deviations smaller than the error. 86

5.28 Velocity: running mean $\overline{v}_{i,2}$ vs. $\overline{v}_{i,1}$ for each particle in a data set (left) and running standard deviation $\sigma_{v,i,2}$ vs. $\sigma_{v,i,1}$ (right). 87

5.29 Histogram of velocities v_x (upper left), v_y (upper right) and v (below) of one particle (diamonds) and Maxwellian fit (solid line). The dashed line is the distribution of measurement errors. 92

5.30 a) Maximum χ^2_ν and b) mean χ^2_ν of v_x, v_y and v v for data sets Ia, IIa and IIIa. 93

5.31 Data set Ia: Kinetic energy k_BT versus radial position R for v_x, v_y and v. The red, dotted lines correspond to the values obtained from the Maxwellian fit. 94

5.32 Data set IIa: Kinetic energy k_BT versus radial position R for v_x, v_y and v. The red, dotted lines correspond to the values obtained from the Maxwellian fit. 95

5.33 Data set IIIa: Kinetic energy k_BT versus radial position R for v_x, v_y and v. The red, dotted lines correspond to the values obtained from the Maxwellian fit. 96

5.34 Gradient of linear fit to $k_BT(R)$ vs. U_{pp} 97

5.35 Example of the histograms of a) $\tilde{x}$, b) $\tilde{y}$ and c) r for one particle (diamonds), and a fit with F_{D1}, F_{D2} respectively (solid line). The curves are normalized to unit area. 100

5.36 a) Maximum χ^2_ν and b) mean χ^2_ν of $\tilde{x}$, $\tilde{y}$ and r for data sets Ia, IIa and IIIa. 101

5.37 a) Normalized histograms of $r_i(t)$ for each particle as an overlay (left side). The black curves indicate a mean distribution for red resp. blue 'particles', b) Corresponding Gaussian fits. The colors from light blue to red indicate the increase of the maximum of $F_{D2}(r_i)$. 102

5.38 Position of all particles in one frame. The cross marks the center of rotation.The colors assign particles to the groups of distributions as it was introduced in figure 5.37. 103

5.39 ν_E as derived in chapter 5.1.2.2 vs. particle charge. Within the rectangle possible charges are located for the frequencies found from the distributions.104

5.40 ν_E estimated from the fit parameter in $F_{D2}(r_i)$ with the particle velocities from chapter 5.4.2 plotted against radial position R for data sets Ia,IIa and IIIa (from top to bottom). 105

5.41 a) Cumulative distribution function for the displacements $r(t)$ of one particle (red line) and two frames (blue and green lines). b) Probability $P_{KS}(D)$ vs. D (Kolmogorov-Smirnov-Statistic, blue), and $P_{KP}(V)$ vs. V (Kuiper-Statistic, red). 110

5.42 Displacements: Kolmogorov-Smirnov test results (left) and Kuiper test results (right). Plotted is the percentage of particles with $P_{KS}(D)$ smaller than the value on the x-axis. The colored lines include only trajectories which belong to the corresponding group found in chapter 5.4.3, compared with all frames. The black line includes all trajectories. The dashed line indicates the limit $\alpha = 0.05$. 114

5.43 Velocities: Kolmogorov-Smirnov test results (left) and Kuiper test results (right). Plotted is the percentage of particles with $P_{KS}(D)$ smaller than the value on the x-axis. The colored lines include only trajectories which belong to the corresponding group found in chapter 5.4.3, compared with all frames. The black line includes all trajectories. The dashed line indicates the limit $\alpha = 0.05$. 116

5.44 Result of Kolmogorov-Smirnov and Kuiper test for the displacements while particle trajectories and particles contributing to the ensemble were choosen for the data sets handed to the test accordingly to the colored groups. . . . 119

5.45 $N_{0.05,KS}$ (diamonds) and $N_{0.05,KP}$ (squares) vs. peak-to-peak voltage U_{pp} for a) displacements and b) velocities and c) displacments splitted into the introduced particle groups. 120

List of Tables

4.1 Standard deviations obtained by the fit and calculated from the data directly 32

5.1 Experimental settings. 45

5.2 Quantities estimated from the data. N_P: number of particles in the field of view; r_{max}: expected maximum deviation from mean lattice site; Δ: mean interparticle spacing; $\lambda_{D,exp} = 2\Delta$: screening length; $\lambda_{D,est}$: screening length estimated with equation (4.31); Γ: coupling parameter (equation (4.33)) . . 47

5.3 Ω obtained as median from the Ω_i and fit parameters of the linear fit to $\Omega(\overline{R}_i)$ 67

5.4 Appearances of alpha and beta errors. In the left column the conclusions drawn from the test result are listed. Both column to the right give the connection to the real situation (which is not known, else one would not apply the test) and the error which is done in the case of a wrong decision. 108

5.5 Displacements: Numbers of compared data sets N_P (single particles) and N_f (ensembles), total number of comparisons N_{tot}, average number of particles in the ensemble $N_{\%f}$ and the percentage of test results $P_{KS/KP}$ smaller than 0.05, $N_{0.05,KS}$ and $N_{0.05,KP}$. 112

5.6 Velocities: Numbers of compared data sets N_P (single particles) and N_f (ensembles), total number of comparisons N_{tot}, average number of particles in the ensemble $N_{\%f}$ and the percentage of test results $P_{KS/KP}$ smaller than 0.05, $N_{0.05,KS}$ and $N_{0.05,KP}$. 115

5.7 Numbers of compared data sets N_P (single particles) and N_f (ensembles), total number of comparisons N_{tot}, average number of particles in the ensemble $N_{\%f}$ and the percentage of test results $P_{KS/KP}$ smaller than 0.05, $N_{0.05,KS}$ and $N_{0.05,KP}$. *Particles and ensemble are divided into groups regarding to the shape of their displacement distribution function. They are labeled red, blue and green* 117